Czech Technical University in Prague
Faculty of Electrical Engineering, Dept. of Electromagnetic Field

Ph.D. Thesis

# Precise Measurement and Modeling on Planar Transmission Lines

*Ondřej Morávek*

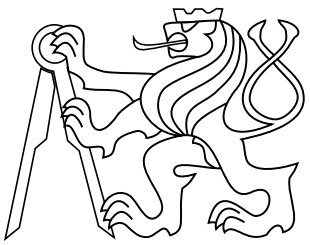

September 2014

Advisor: prof. Ing. Karel Hoffmann, CSc.

## Acknowledgement

I would like to sincerely thank to my supervisor Karel Hoffmann and to all colleagues at the Department of Electromagnetic Field for important advices and stimulations that were essential during my work.

## Declaration

I declare that I worked out the presented thesis independently and I quoted all used sources of information in accord with Methodical instructions about ethical principles for writing academic thesis.

## Abstrakt

Cílem této dizertační práce je publikovat výsledky dosažené v oblasti mikrovlnné techniky, na kterých jsem pracoval v průběhu mého doktorského studia. Název této dizertační práce – *Precizní měření a modelování na planárních vedeních* – odráží hlavní motivaci této práce, která si klade za cíl ukázat inovace a pokrok, kterého bylo dosaženo v oblasti přesného měření na planárních vedeních a odstraňování překážek s tím souvisejících. V této dizertační práci je prezentováno skloubení několika stěžejních článků, které byly publikovány v odborných recenzovaných časopisech na témata úzce související s názvem této dizertační práce. Přijetí těchto publikací je znamením, že téma je v dnešní době velmi aktuální a problematika je zajímavá pro vědeckou komunitu v oboru mikrovlnného měření, kalibrací a modelování planárních komponent.

Technologie spojené s měřením na mikrovlnných planárních vedeních lze rozdělit na dvě hlavní oblasti. Historicky již od počátků mikropáskových vedení byly navrhovány mechanické přechody mezi dvěma typy vedení, kterými byl přiváděn mikrovlnný signál na planární strukturu. Modernějším řešením je použití takzvaných wafer-probe stanic, kterými lze měřit mikropáskové planární obvody bez použití mechanických přechodů. Oba přístupy přinášejí své výhody a omezení. Jedním z efektů u konvenčních přechodů z koaxiálního na mikropáskové vedení, který je analyzován v této dizertační práci, je problém vyzařování elektromagnetického signálu z místa přechodu a jeho následná interakce s měřenou planární strukturou nebo měřeným objektem. Tyto efekty se mohou v určité podobě vyskytovat i na wafer-probe stanicích, což nebylo zkoumáno v rámci této dizertace.

Vliv takového vyzařování se projeví do jedno i víceportových měření na vektorovém analyzátoru a do přesnosti, s jakou je možné takový analyzátor zkalibrovat ve vybrané referenční rovině na mikropáskovém vedení pro měření aktivních nebo pasivních obvodů. Díky moderním 3D simulátorům pole je možné zreprodukovat problém pomocí numerických výpočtů. Následnou analýzou je v této práci prezentováno jedno z možných vysvětlení původu vyzářeného pole a je navržen možný způsob potlačení tohoto jevu. Modifikovaný přechod je podroben zkouškám jak syntetickými kalibracemi, tak i měřením na reálných testovacích mikropáskových přípravcích a výsledky jsou porovnány.

Vzhledem k relativně krátkému časovému horizontu, ve kterém došlo k prvním publikacím na téma vliv vyzařování na vektorové kalibrace, je řešení tohoto jevu stále otevřené a na definitivní fyzikální popis problému stále čeká. Tato práce klade větší důraz na mechanické úpravy, které vedou k pochopení a potlačení těchto nežádoucích efektů spolu s popisem a návrhem metodiky pro provádění experimentů, kterými je možné tyto efekty kvantifikovat.



### Klíčová slova

Kalibrace; měřicí techniky; mikrovlnná měření; efekty vyzařování; vektorová obvodová analýza

## Abstract

Goal of this thesis is to present results achieved in the field of microwave theory and techniques that I have been working on during the several years of my doctoral studies. The name of this thesis – *Precise Measurement and Modeling on Planar Transmission Lines* – reflects the main motivation of this thesis, which aims to show an innovation and novelty, that have been achieved in the area of precise measurement on planar transmission lines and in elimination of related obstacles. This dissertation combines several crucial papers that have been published in peer-reviewed journals on topics that are very strongly bound with the title of this thesis. The acceptance of these papers is a good sign that this research is still actual and the issues that have been worked on are interesting for the community in the field of measurement, calibration and modeling of planar components.

Technical equipment associated with a measurement on planar transmission lines can be divided into two parts. There have been mechanical transitions between two types of transmission lines since the origin of microstrip lines. These transitions feed the microwave signal to the planar structure. More modern approach include the wafer-probe stations which can be used to directly measure the planar devices without specific launchers. Both these ways have their advantages and limitations. One of the unwanted effect of the conventional transitions, that is being analyzed in this thesis, is a radiation of electromagnetic wave from the launcher edge and its interaction with the planar device under test. These effects can be certainly observed even on the wafer-probe stations, however this issue has not been investigated in this thesis.

The influence of radiation would be observable during one or multi-port measurements on a vector network analyzer and it would decrease the potential precision and accuracy of the calibration of such analyzer in a chosen reference plane on a microstrip transmission line (either for passive or active circuits measurement). Thanks to the modern 3D electro-magnetic field simulators it is now possible to reproduce the problem using the numerical calculations. With a subsequent analysis in this thesis, one of the possible physical explanations of the radiation effect is presented and one practical way of the radiation suppression is being proposed. The modified transition is subjected to a synthetic measurement validation as well as real-world measurement with microstrip test-boards with comparison of both results in the end.

Due to the relatively short timescale of which the first publications on the topic of such influence on a vector calibration emerged, the definitive solution of the effect with its deep physical understanding is still being looked for. This thesis emphasizes the mechanical modifications and the full-wave field simulations that lead to understanding a suppression of these unwanted effects along with a new methodology for experimental verification which can be used to quantify these effects.



### Keywords

Calibration; measurement techniques; microwave measurements; radiation effects; vector network analysis

# Contents

## Abbreviations

List of abbreviations used in this thesis and their meaning.

| | |
|---|---|
| AWR MWO | AWR Microwave Office design software |
| CPWG | Grounded Coplanar Waveguide transmission line |
| CST MWS | CST Microwave Studio simulation software |
| DUT | Device Under Test |
| EM | Electro Magnetic |
| FEM | Finite Element Method |
| OSM | Open-Short-Match calibration technique |
| OSO | Open-Short-Open (offset) calibration technique |
| PCB | Printed Circuit Board |
| QTEM | Quasi-TEM mode present on microstrip transmission line |
| SMA | SubMiniature interface version A |
| SMD | Surface Mount Device |
| SOLR | Short-Open-Load-Reciprocal calibration technique |
| SOLT | Short-Open-Load-Thru calibration technique |
| TEM | Transversal Electromagnetic mode - common for transmission lines |
| TRL | Thru-Reflect-Line calibration technique |
| TRP | Total Radiated Power |
| VNA | Vector Network Analyzer |
| VRC | Voltage Reflection Coefficient ($\Gamma$) |
| VSWR | Voltage Standing Wave Ratio |

# 1 Introduction

The aim of this thesis is to describe an original contribution to the field of precise microwave vector measurements in the region of RF and millimeter-wave frequencies especially on planar microwave transmission lines. This area has been subjected to an active research for a very long time since the original development of the first automated vector network analyzer (VNA) by Hackborn [1]. This effort started a development of calibration and correction methods for measurement using VNA.

These days, there is a vast amount of calibration techniques [2] which are suitable for different types of microwave transmission lines, but reliable and robust methods usable on planar transmission lines (namely microstrip and coplanar waveguide) are still not fully perfected. Among the most popular calibration methods, there are the 12-term error terms techniques – Short-Open-Load-Thru (SOLT) [3] with its over-determined variant [4] and various 8-term error terms techniques – Short-Open-Load-Reciprocal (SOLR) [5], Thru-Reflect-Line (TRL) [6] and multi-line TRL [7].

These calibration methods rely on evaluation of the error terms solving system of mostly linear equations. Finally, raw measured S-parameters with (partial) knowledge lead to evaluation of the error model parameters $e_{ij}$. The degree of uncertainty associated with the error parameters is correlated with distance among calibration standards calculated in the complex-plane [8]. The uncertainty propagation in the calibration procedure has been extensively studied in the past years by means of calculation of covariance matrices that handle elliptically-shaped uncertainty areas [9, 10].

There are existing software implementations of numeric derivation of the calibration uncertainty that were recently published [11, 12, 13]. Some of these tools provide Monte-Carlo calculations that account for nonlinear error propagation [14]. However, none of these techniques is able to account for errors caused by radiation from a coaxial-to-microstrip transition. This issue will be discussed and analyzed in this thesis.

An important aspect of this thesis is modeling on planar transmission lines. 3D full-wave simulations are becoming important alternative in the field of microwave techniques. It is a promising way of testing new designs, analyzing the existing structures and it helps to understand physical relations between the reality and simulated results. Therefore the modeling part is closely related to the measurement and optimal results are achieved by combining both approaches.

This thesis is divided into several chapters that should cover all important topics about precise planar microwave measurements and modeling and will present new findings presented by the author during the past four years.

Second chapter will introduce the reader into the theory of uncertainties in microwave measurements and show some of its applications on the practical measurement. The example utilizes the uncertainty calculation to show a degree of quality for a sliding mismatch second-tier calibration on coplanar transmission line which is then used to perform a secondary correction to the error model.

Third chapter is dedicated to the problem of radiation from coaxial-to-planar transitions that was recently discovered and was established to be an issue in the millimeter wave region. In this chapter the current state-of-the-art in the radiation phenomenon is introduced. Some existing suppression solutions are being discussed as well. Following

chapters are based only on the original contributions of this thesis' author.

Fourth chapter of this thesis deals with experimental quantification of the radiated wave and real-world measurement validation of the proposed ideas that are presented in the third chapter. Practical methodology is described that helps to prepare a scenario for each individual combination of transition and microwave transmission line. There is also a description of a theoretical model (an equivalent circuit) of the coaxial-to-microstrip transition with added radiation losses dependent on the character of the load impedance.

Fifth chapter shows a novel concept of coaxial-to-microstrip transition with suppressed radiation. This design was published and shows a crucial part of this thesis. The chapter illustrates the benefits of such proposals and validates the concept with full-wave simulations results, some of which were used to perform a synthetic calibration and correction. Real-world one-port and two-port measurements with applied calibration and correction are illustrated as well.

## 1.1 Dissertation goals

1. Collect the current state-of-the-art in the field of precise microwave measurements and calibrations and describe the issue of radiation from coaxial-to-planar transitions.
2. Develop a reproducible technique of quantification of radiated wave from any given transition thus enabling a qualitative practical evaluation of existing test-fixtures with specific transmission line.
3. Validate the concept of synthetic measurements and show its applications with the possible utilization of the 3D electro-magnetic full-wave simulation tools. Show that the data from synthetic measurement has its useful value during the research and development process.
4. Analyze the coaxial-to-planar transition's radiation effect from the antenna theory point of view and present an explanation of its origin with possible analogies.
5. Evaluate the existing concepts of coaxial-to-microstrip transitions from the radiation point of view and focus on a suppression of the radiated field, thus enabling a more precise measurement on microstrip.

# 2 Short introduction into uncertainties in microwave measurements

When talking about precise microwave measurement, first chapter of this thesis has to start with introduction into uncertainty and its propagation in microwave measurement. This chapter aims to provide very basic examples and illustrate the concept on real-world examples.

Uncertainty in microwave measurement is closely related to the uncertainties propagation of complex numbers. When dealing with uncertainties within a measurement, all procedures have to be consistent with ISO Guide to the expression of uncertainty in measurement [15]. One of the first comprehensive papers which gives introduction into uncertainty of complex-valued S-parameters was published by Ridler in 2001 [9] and this chapter is based on the theory presented in this paper.

While performing a measurement on VNA, the measured values are used to perform some calculations (calibration and correction) to obtain some output quantity. If the uncertainty in the individual S-parameters is estimated, one has to propagate them through to the uncertainty of the output quantity.

Let's have $m$ output quantities $\mathbf{Y} = (y_1, y_2, ..., y_m)$ which are related to the $n$ input quantities $\mathbf{X} = (x_1, x_2, ..., x_n)$ with a function $\mathbf{f}$:

$$\mathbf{Y} = \mathbf{f}(\mathbf{X}) \tag{1}$$

where $\mathbf{f}$ is a function which is mapping the $n$-dimensional space into $m$-dimensional space. The function $f$ can be rewritten into $m$ components functions $f_1, f_2, ..., f_m$. Generally, each output quantity is a function of all input quantities (the components of the input vector). If there is only one output quantity ($\mathbf{Y}$ is scalar) then there is only one component function $f$. The Jacobian matrix $J$ of the transformation $\mathbf{f}$ is a matrix of sensitivity coefficients (partial derivatives):

$$J = \begin{bmatrix} \frac{\partial f_1}{\partial x_1} & \frac{\partial f_1}{\partial x_2} & \cdots & \frac{\partial f_1}{\partial x_n} \\ \frac{\partial f_2}{\partial x_1} & \frac{\partial f_2}{\partial x_2} & \cdots & \frac{\partial f_2}{\partial x_n} \\ \vdots & \vdots & \ddots & \vdots \\ \frac{\partial f_m}{\partial x_1} & \frac{\partial f_m}{\partial x_2} & \cdots & \frac{\partial f_m}{\partial x_n} \end{bmatrix} \tag{2}$$

If there is single output quantity, the Jacobian matrix becomes:

$$J = \begin{bmatrix} \frac{\partial f}{\partial x_1} & \frac{\partial f}{\partial x_2} & \cdots & \frac{\partial f}{\partial x_n} \end{bmatrix} \tag{3}$$

To illustrate the notation above, let's consider conversion between polar coordinates and Cartesian coordinates of a point in a complex plane. Vector of input quantities $\mathbf{X}$ contains polar coordinates and the vector of output quantities $\mathbf{Y}$ contains Cartesian coordinates of a point.

$$\begin{aligned} \mathbf{X} &= (r, \phi) \\ \mathbf{Y} &= (r\cos\phi, r\sin\phi) \end{aligned} \tag{4}$$

The transformation function $\mathbf{f}$ is mapping from 2-dimensional space to itself. The component functions are defined by:

$$\begin{aligned} y_1 &= f_1(r,\phi) = r\cos\phi \\ y_2 &= f_2(r,\phi) = r\sin\phi \end{aligned} \tag{5}$$

The Jacobian matrix of this transformation is:

$$J = \begin{bmatrix} \frac{\partial f_1}{\partial r} & \frac{\partial f_1}{\partial \phi} \\ \frac{\partial f_2}{\partial r} & \frac{\partial f_2}{\partial \phi} \end{bmatrix} = \begin{bmatrix} \cos\phi & -r\sin\phi \\ \sin\phi & r\cos\phi \end{bmatrix} \tag{6}$$

In the matrix form, the law of propagation of uncertainty states [16]:

$$V(\mathbf{Y}) = J \cdot V(\mathbf{X}) \cdot J^T \tag{7}$$

where $V(\mathbf{X})$ and $V(\mathbf{Y})$ are covariance matrices of the input and output vectors and $J$ is Jacobian matrix of the transformation $f$. The covariance matrix of the input vector $V(\mathbf{X})$ is $n \times n$ matrix which expresses the uncertainty in the $n$ input quantities including the effect of correlation. It is defined:

$$\begin{aligned} V(\mathbf{X}) &= \begin{bmatrix} u^2(x_1) & u(x_1,x_2) & \cdots & u(x_1,x_n) \\ u(x_2,x_1) & u^2(x_2) & \cdots & u(x_2,x_n) \\ \vdots & \vdots & \ddots & \vdots \\ u(x_n,x_1) & u(x_n,x_2) & \cdots & u^2(x_n) \end{bmatrix} = \\ &= \begin{bmatrix} u^2(x_1) & u(x_1)\,u(x_2)\,r(x_1,x_2) & \cdots & u(x_1)\,u(x_n)\,r(x_1,x_n) \\ u(x_2)\,u(x_1)\,r(x_2,x_1) & u^2(x_2) & \cdots & u(x_2)\,u(x_n)\,r(x_2,x_n) \\ \vdots & \vdots & \ddots & \vdots \\ u(x_n)\,u(x_1)\,r(x_n,x_1) & u(x_n)\,u(x_2)\,r(x_n,x_2) & \cdots & u^2(x_n) \end{bmatrix} \end{aligned} \tag{8}$$

Diagonal elements of the covariance matrix represent squared standard uncertainties (variances). The off-diagonal elements represent covariance terms. Correlation coefficient $r(x_i,x_j)$ (dimensionless) takes values from $-1$ (maximum negative correlation) to $+1$ (maximum positive correlation). The covariance matrix is symmetric therefore elements below the main diagonal contain no extra information. Similarly, the covariance matrix of the output vector $V(\mathbf{Y})$ is $m \times m$ matrix which expresses the uncertainty in the $m$ output quantities including the effect of correlation. It has the same structure

as $V(\mathbf{X})$:

$$V(\mathbf{Y}) = \begin{bmatrix} u^2(y_1) & u(y_1,y_2) & \cdots & u(y_1,y_m) \\ u(y_2,y_1) & u^2(y_2) & \cdots & u(y_2,y_m) \\ \vdots & \vdots & \ddots & \vdots \\ u(y_m,y_1) & u(y_m,y_2) & \cdots & u^2(y_m) \end{bmatrix} = \tag{9}$$

$$= \begin{bmatrix} u^2(y_1) & u(y_1)\,u(y_2)\,r(y_1,y_2) & \cdots & u(y_1)\,u(y_m)\,r(y_1,y_m) \\ u(y_2)\,u(y_1)\,r(y_2,y_1) & u^2(y_2) & \cdots & u(y_2)\,u(y_m)\,r(y_2,y_m) \\ \vdots & \vdots & \ddots & \vdots \\ u(y_m)\,u(y_1)\,r(y_m,y_1) & u(y_m)\,u(y_2)\,r(y_m,y_2) & \cdots & u^2(y_m) \end{bmatrix}$$

## 2.1 Special case of the uncertainty propagation

Equation 7 expresses the propagation of uncertainty in matrix form, however it is more common to see this law as a sum over indexed terms. It will be shown that equation 7 reduces to familiar form in two important special cases.

### 2.1.1 (Un)correlated input quantities and a single output quantity

If the input quantities are uncorrelated, the covariance matrix of the input vector is diagonal:

$$V(\mathbf{X}) = \begin{bmatrix} u^2(x_1) & 0 & \cdots & 0 \\ 0 & u^2(x_2) & \cdots & 0 \\ \vdots & \vdots & \ddots & \vdots \\ 0 & 0 & \cdots & u^2(x_n) \end{bmatrix} \tag{10}$$

Additionally the output vector degenerates into scalar since it is assumed that there is only one output quantity. Covariance matrix of the one-term output vector is:

$$V(\mathbf{Y}) = \left[u^2(y)\right] \tag{11}$$

The Jacobian matrix for the transformation is a $1 \times n$ matrix:

$$J = \begin{bmatrix} \frac{\partial f}{\partial x_1} & \frac{\partial f}{\partial x_2} & \cdots & \frac{\partial f}{\partial x_n} \end{bmatrix} \tag{12}$$

The law of propagation of uncertainty (equation 7) becomes:

$$\left[u^2(y)\right] = \begin{bmatrix} \frac{\partial f}{\partial x_1} & \frac{\partial f}{\partial x_2} & \cdots & \frac{\partial f}{\partial x_n} \end{bmatrix} \begin{bmatrix} u^2(x_1) & 0 & \cdots & 0 \\ 0 & u^2(x_2) & \cdots & 0 \\ \vdots & \vdots & \ddots & \vdots \\ 0 & 0 & \cdots & u^2(x_n) \end{bmatrix} \begin{bmatrix} \frac{\partial f}{\partial x_1} \\ \frac{\partial f}{\partial x_2} \\ \vdots \\ \frac{\partial f}{\partial x_n} \end{bmatrix} \tag{13}$$

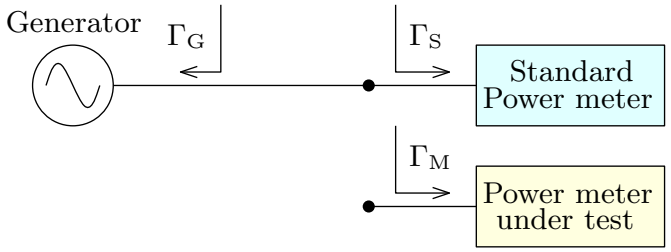


**Fig. 1** Comparison loss in power meter calibration measurement.

If the matrix multiplication is carried out, the following is obtained:

$$u^2(y) = \sum_{i=1}^{n} \left( \frac{\partial f}{\partial x_i} \right)^2 u^2(x_i) \tag{14}$$

This is the form of the law of uncertainty propagation given in 7, but for uncorrelated input quantities. By following a similar procedure, one can achieve the equation for correlated input quantities:

$$u^2(y) = \sum_{i=1}^{n} \sum_{j=1}^{n} \frac{\partial f}{\partial x_i} \frac{\partial f}{\partial x_j} u(x_i, x_j) \tag{15}$$

### 2.1.2 Uncertainty for complex-valued quantities

Let's have a complex valued quantity $z = z_R + jz_I$. The uncertainty is expressed as a $2 \times 2$ covariance matrix:

$$\begin{bmatrix} u^2(z_R) & u(z_R, z_I) \\ u(z_I, z_R) & u^2(z_I) \end{bmatrix} \tag{16}$$

For a $n$-dimensional vector of complex-valued quantities, the uncertainty is expressed by a $2n \times 2n$ covariance matrix. When applying the law of propagation uncertainty, each complex-valued quantity contributes two components to either the vector of input quantities $V(\mathbf{X})$ or the vector of output quantities $V(\mathbf{Y})$.

## 2.2 Comparison loss in power meter calibration

To illustrate the uncertainty propagation on an example, let's choose a power meter calibration using a stable signal generator and a standard power meter (illustration in Fig. 1). Power absorbed by two different power meters will vary generally due to the fact that their input voltage reflection coefficient (VRC) $\Gamma$ is different. The ratio of power absorbed by the power meter under test $P_M$ to the power absorbed by the standard power meter $P_S$ is defined as:

$$M_1 = \frac{P_M}{P_S} = \frac{1 - |\Gamma_M|^2}{1 - |\Gamma_M|^2} \frac{|1 - \Gamma_S \Gamma_G|^2}{|1 - \Gamma_M \Gamma_G|^2} \tag{17}$$

where $\Gamma_G$ is VRC of the signal generator, $\Gamma_M$ is VRC of the power meter under test and $\Gamma_S$ is VRC of the standard power meter. This ratio is referred in the literature as

*comparison loss* [17]. The formula can be further simplified if a standard reflectionless power meter (i.e. $\Gamma_S = 0$) is used:

$$M_2 = \frac{P_M}{P_S} = \frac{1 - |\Gamma_M|^2}{|1 - \Gamma_M \Gamma_G|^2} \tag{18}$$

If both the standard power meter and signal generator are reflectionless (i.e. $\Gamma_S = \Gamma_G = 0$), the comparison loss becomes:

$$M_3 = \frac{P_M}{P_S} = 1 - |\Gamma_M|^2 \tag{19}$$

It is difficult to measure VRC of a signal generator. But when a directional coupler is used at the output of a generator in automatic leveling loop, the effective VRC of the stabilized generator is determined solely by S-parameters of the coupler [18]:

$$\Gamma_G = S_{22} - \frac{S_{12} S_{23}}{S_{13}} \tag{20}$$

The law of propagation of uncertainty (equation 7) is applied to the transformations in equations 17 to 20 which have to be solved during power meter calibration. The input quantities of these transformations are complex-valued S-parameters. In equations 17 to 19, the single output quantity is a real-valued mismatch term. In equation 20, the single output quantity is a complex-valued VRC which then becomes an input quantity in equations 17 and 18.

## 2.3 Comparison loss with reflectionless power meter and signal generator

Let's consider the expression for *comparison loss* in equation 19 where both the standard power meter and the signal generator are assumed to be reflectionless.

$$M_3 = 1 - |\Gamma_M|^2 \tag{21}$$

### 2.3.1 If only the magnitude of $\Gamma_M$ is measured

The 1-dimensional vector of input quantities is:

$$\mathbf{X} = (|\Gamma_M|) \tag{22}$$

and 1-dimensional vector of output quantities is:

$$\mathbf{Y} = (M_3) \tag{23}$$

The covariance matrix of the input quantities is:

$$V(|\Gamma_M|) = \left[u^2(|\Gamma_M|)\right] \tag{24}$$

and the covariance matrix of the output quantities is:

$$V(M_3) = \left[u^2(M_3)\right] \tag{25}$$

The $1 \times 1$ Jacobian matrix of the transformation is given by:

$$J = \left[\frac{\partial M_3}{\partial |\Gamma_M|}\right] = \left[-2|\Gamma_M|\right] \tag{26}$$

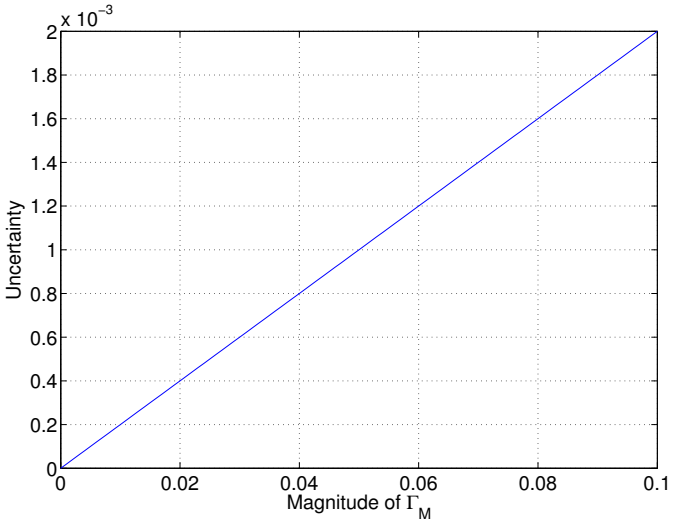


**Fig. 2** Uncertainty in $M_3$ plotted against $|\Gamma_M|$. Uncertainty $u\left(|\Gamma_M|\right) = 0.001$.

By the law of uncertainty propagation:

$$\begin{aligned} V\left(M_3\right) &= J\,V\left(|\Gamma_M|\right)\,J^T \\ \left[u^2\left(M_3\right)\right] &= \left[-2|\Gamma_M|\right]\left[u^2\left(|\Gamma_M|\right)\right]\left[-2|\Gamma_M|\right] \end{aligned} \tag{27}$$

This can be simplified to:

$$u^2\left(M_3\right) = 4|\Gamma_M|^2 u^2\left(|\Gamma_M|\right) \tag{28}$$

Therefore the uncertainty in $M_3$ is given by:

$$u\left(M_3\right) = 2|\Gamma_M| u\left(|\Gamma_M|\right) \tag{29}$$

The uncertainty in $M_3$ depends on the magnitude of $\Gamma_M$ and the corresponding uncertainty. A plot is shown in Fig. 2 where it is assumed that $u\left(|\Gamma_M|\right) = 0.001$ and is independent of $|\Gamma_M|$.

### 2.3.2 The *comparison loss* in terms of the real and imaginary parts

Let's assume the VRC of the power meter under test as $\Gamma_M = x + jy$. The *comparison loss* is then equal to:

$$M_3 = 1 - x^2 - y^2 \tag{30}$$

If the real and imaginary parts of $\Gamma_M$ the vector of input quantities is:

$$\mathbf{X} = (x, y) \tag{31}$$

and the 1-dimensional vector of output quantities is

$$\mathbf{Y} = (M_3) \tag{32}$$

The covariance matrix $2 \times 2$ of the input quantities is:

$$V\left(\Gamma_M\right) = \begin{bmatrix} u^2\left(x\right) & u\left(x,y\right) \\ u\left(y,x\right) & u^2\left(y\right) \end{bmatrix} \tag{33}$$

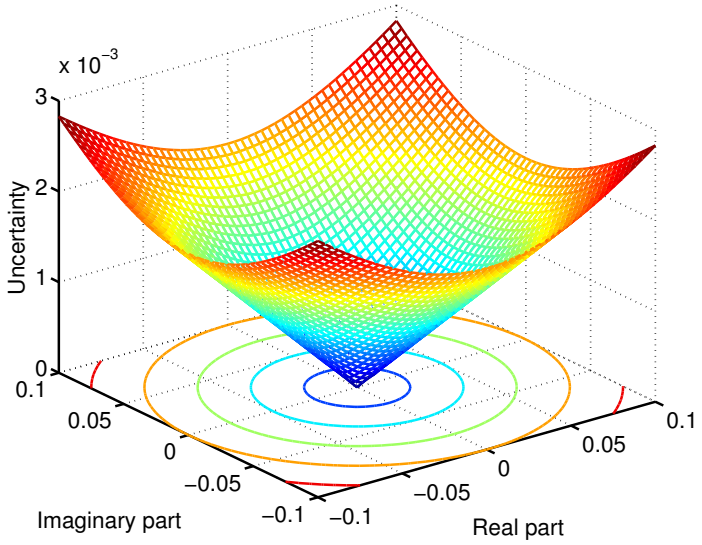


**Fig. 3** Uncertainty in $M_3$ plotted against $\Gamma_M$. Uncertainty $u(x) = u(y) = 0.01$. Correlation coefficient $r(x, y) = 0$.

and the covariance matrix of the output quantities is:

$$V(M_3) = \left[u^2(M_3)\right] \tag{34}$$

The Jacobian matrix $(1 \times 2)$ of the transformation is given by:

$$J = \left[\frac{\partial M_3}{\partial x} \quad \frac{\partial M_3}{\partial y}\right] = \left[-2x \quad -2y\right] \tag{35}$$

By the law of uncertainty propagation:

$$\begin{aligned} V(M_3) &= J\,V(\Gamma_M)\,J^T \\ \left[u^2(M_3)\right] &= \left[-2x \quad -2y\right] \begin{bmatrix} u^2(x) & u(x,y) \\ u(y,x) & u^2(y) \end{bmatrix} \begin{bmatrix} -2x \\ -2y \end{bmatrix} \end{aligned} \tag{36}$$

If the matrices are multiplied out and by using the fact that $u(x, y) = u(y, x)$.

$$u^2(M_3) = 4\left[u^2(x)\,x^2 + u^2(y)\,y^2 + 2u(x,y)\,xy\right] \tag{37}$$

Which yields the uncertainty in $M_3$ as:

$$u(M_3) = 2\sqrt{u^2(x)\,x^2 + u^2(y)\,y^2 + 2u(x,y)\,xy} \tag{38}$$

The correlation coefficient between real and imaginary parts $r(x, y)$ can be used to rewrite the term:

$$u(M_3) = 2\sqrt{u^2(x)\,x^2 + u^2(y)\,y^2 + 2r(x,y)\,u(x)\,u(y)\,xy} \tag{39}$$

Compared to the equation 29 now the uncertainty in $M_3$ is dependent on real and imaginary parts of $\Gamma_M$, their uncertainties and correlation coefficient between real and imaginary parts. Fig. 3 and Fig. 4 show uncertainty profiles plotted above the complex VRC plane. The correlation coefficient is $r(x, y) = 0$ or 0.8 respectively. Note that the Fig. 2 is just a cross-section of the Fig. 3.

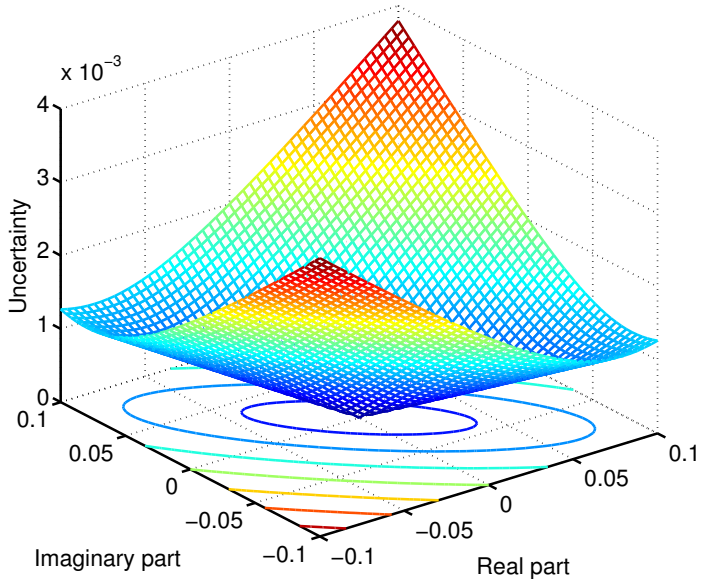


**Fig. 4** Uncertainty in $M_3$ plotted against $\Gamma_M$. Uncertainty $u(x) = u(y) = 0.01$. Correlation coefficient $r(x, y) = 0.8$.

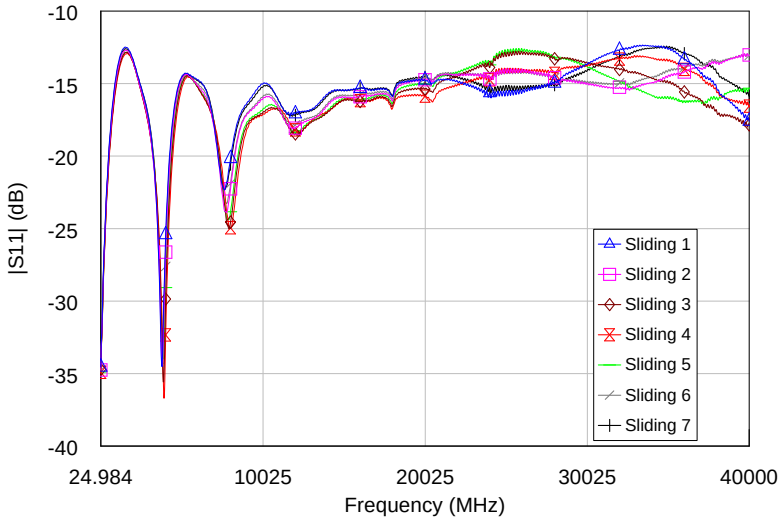


**Fig. 5** Corrected measurement of the sliding load placed in multiple positions along the transmission line. Notice the variation of the $|S_{11}|$ increasing with frequency.

## 2.4 Uncertainty values of circle-fitting for validation of planar calibration

Practical applications of the uncertainty propagation in microwave measurements and calibration can be illustrated on the verification process of a planar calibration.

The basic qualitative verification of the planar calibration can be done by doing a simple sliding mismatch measurement. By measuring the reflection $S_{11}$ of the sliding load element in several different positions along the transmission line, one obtains the values shown in Fig. 5. The measurement set-up can be seen in Fig. 6.

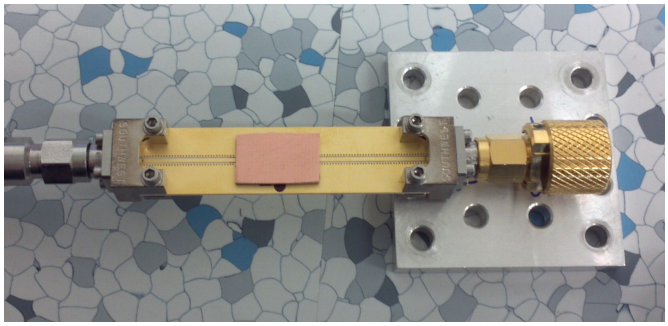

**Fig. 6** Evaluation board mounted between coaxial to coplanar launchers with a sliding load.

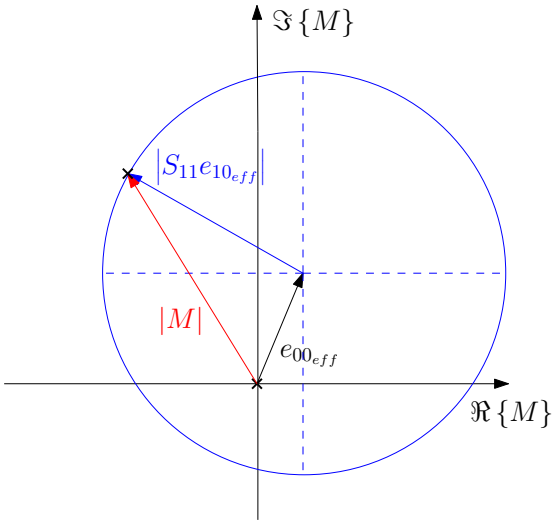


**Fig. 7** Vectorial representation of measuring different reflections $\Gamma_i$ while moving a sliding mismatch element to obtain the calibration error vector $e_{00}$.

It can be seen in the Fig. 5 that magnitude of corrected reflection coefficient $S_{11}$ created by the mismatch is varying with the position along the transmission line in a specific way that is not what one would expect. The reflection coefficient from the sliding mismatch should change its value predictably and the magnitude should linearly decrease with distance. This effect can be observed in the measured data up to approx. 20 GHz. This can be thought of as transformation of the reflection coefficient along a lossy transmission line.

However, in higher frequencies the effect of improper calibration starts to appear as the reflection from the sliding mismatch is not transformed along the center of the Smith chart, but along the point that is determined by the effective directivity. This invalidates the assumption that the current error model includes the system's error terms up to the measurement reference plane. In other words, there is some uncorrected residual directivity $e_{00_{\text{eff}}}$ [19, 20] present after the calibration.

The phase of measured values $arg\,(S_{11})$ varies because of the different position in each measurement. When one plots the value of $S_{11}$ into the polar graph the points can be easily fitted with a circle (schematically drawn in Fig. 7). The measured example of the imaginary circle on 25 GHz is depicted in Fig. 8. The calculated center of the circle is the complex value of residual directivity $e_{00_{\text{eff}}}$.

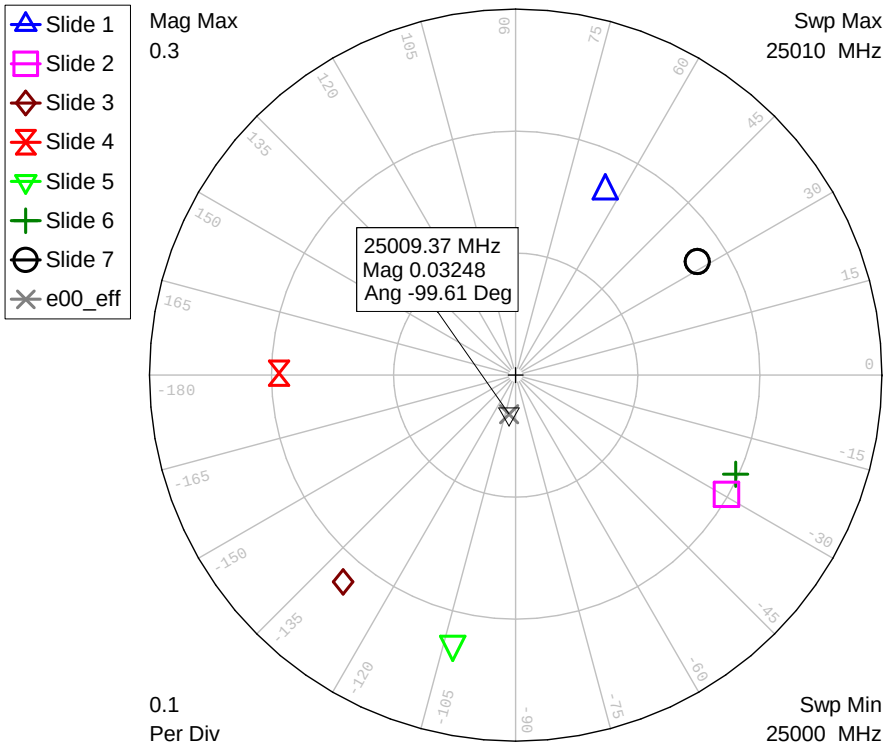


**Fig. 8** Calculated value of $e_{00_{\text{eff}}}$ on 25 GHz based on 7-position sliding load measurement.

A common 1-port calibration equation is usually written as follows

$$M = e_{00} + \frac{e_{10}\Gamma_{\text{DUT}}}{1 - e_{11}\Gamma_{\text{DUT}}} \tag{40}$$

The error terms determined using equation 40 are then used to correct the measured data $M$ to obtain the corrected value of $S_{11}$.

$$S_{11} = \frac{M_{\text{DUT}} - e_{00}}{e_{10} + e_{11}\left(M_{\text{DUT}} - e_{00}\right)} \tag{41}$$

The equation 40 can be used to describe the points obtained in the Fig. 8 as well [2]. It is assumed that $|S_{11}| \approx 0.1$ and $|e_{11_{\text{eff}}}| \ll 0.1$ thus one can simplify equation 40 to get:

$$M = e_{00_{\text{eff}}} + e_{10_{\text{eff}}} S_{11} \tag{42}$$

The resulting vectorial superposition yields a circle with radius $|S_{11}e_{10_{\text{eff}}}|$. The term $e_{00_{\text{eff}}}$ can be calculated in the frequency range of interest. However, one has to take into account the uncertainty associated with the fitting algorithm (especially on lower frequencies).

The measured complex values of $S_{11}e_{10_{\text{eff}}}$ on single frequency have to be sufficiently separated in phase so that the resulting circle fit is unambiguous. This problem can be illustrated by the Fig. 9.

On lower frequencies the determination uncertainty of the circle's center is higher because the phase difference is reduced. This uncertainty analysis can be used to estimate the lowest acceptable frequency limit for $e_{00_{\text{eff}}}$ calculation. In this measurement scenario one can estimate the acceptable frequency band from the uncertainty analysis of the evaluated $|e_{00_{\text{eff}}}|$ to be approximately 15 GHz. The frequency band width of

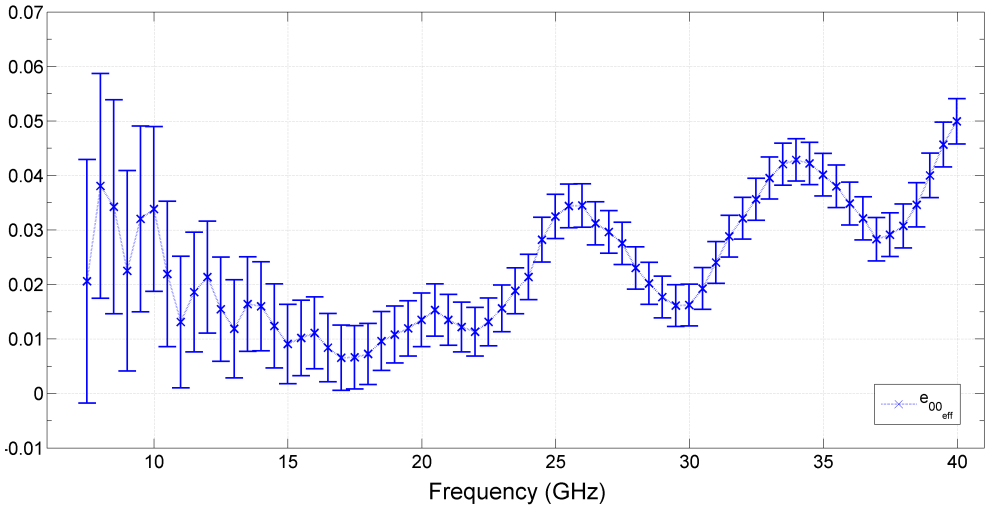


**Fig. 9** Calculated values of $|e_{00_{\text{eff}}}|$ based on 7-position sliding load measurement. Values are plotted with error bars based on a standard uncertainty of the circle fitting procedure.

this verification technique was not a requirement known in advance therefore it was determined from the chosen sliding load positions which were random.

# 3 Radiation of coaxial-to-planar transitions

Along with advances in microwaves, there comes a need for feeding the microwave signal from coaxial to planar transmission lines to perform a measurement and characterizations of various active and passive devices. Precise measurement is essential to enable an accurate extraction of various large-signal models or equivalent circuits of packaged transistors [21, 22].

A large number of interesting and innovative designs of these transitions were proposed and patented since the eighties [23, 24, 25, 26, 27, 28, 29] that are suitable either for microstrip or for coplanar waveguide transmission line. Some of these concepts intentionally shape electromagnetic (EM) field distribution at the transition to improve microwave performance and to reduce the unwanted effects of the discontinuity. The quality of such transition was assessed mostly by a magnitude of a reflection coefficient, insertion loss and by its mechanical usability. Now it turns out that the concept of these transitions is even more complicated.

Radiation of an electromagnetic wave originating at the coaxial-to-microstrip transition is a recently discovered field of interest [30] that influences precise microwave measurements in open transmission lines in $K$ band and above. Considerable attention has been recently given to the radiation of the leaky-wave modes from the planar transmission lines [31, 32, 33]. However the radiation mode at the transition is not to be confused with the well described leaky-wave mode. Planar leaky-wave antennas are subject of active research [34, 35] these days and to excite the leaky-wave modes in general, one has to design a microstrip line with width of the microstrip greater than quarter-wavelength on the desired frequency. All simulations and measurements in this thesis are done within the single-mode propagation region of the microstrip and well below the possible excitation of leaky-wave modes.

## 3.1 Current state-of-the-art

Some important studies on the radiation problem have been published. For example, it has been shown that the radiation clearly disturbs [30] commonly used calibration methods on microstrip and introduces other interesting phenomenons and problems [36, 37] associated with the radiation during measurement with VNA. The fact that the radiated wave interferes with the Quasi-TEM (QTEM) mode on microstrip and introduces some added losses as well helps to explain why the most frequently used calibration methods are affected by the radiation.

Radiation from the transitions demonstrated itself to be somehow dependent on the standing-wave distribution within the test-fixture. It was observed [30] (later verified [38, 39]) that the magnitude of radiated power is proportional to the phase of the reflected wave and thus it depends directly on the distance of the discontinuity from the transition and on the reflection coefficient of the device under test (DUT) itself. This means that the error model is dependent on the reflection coefficient of the DUT.

The condition of constant error model parameters for each measured DUT applies for all calibration methods suitable for microstrip (the frequently used examples can

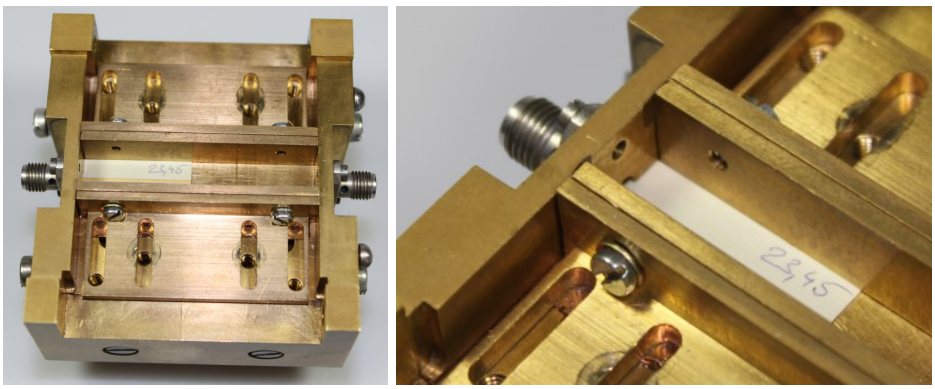

a) b)

**Fig. 10** Plan view (a) and perspective (b) of the *canyon* test-fixture [44] with microstrip calibration standard as a DUT.

be found in literature [3, 5, 6, 7, 40, 41, 42]. However, this condition is not fulfilled in the case where the radiation introduces additional losses and a multi-mode propagation where both modes (QTEM and radiated wave) can interfere with each other.

Different hardware approaches supported with 3D EM full-wave simulations were proposed recently to control and suppress the radiation problem. Cheng [43] suggests modifications in the SMA coaxial-to-microstrip transitions. It is based on enclosing the transition into a conducting metal ring. The other solution [44] suggests placing the microstrip line between two conducting sidewalls from both sides in such distance so it will not influence the microstrip QTEM mode. This unfortunately introduces possible waveguide-like behavior of such structure. Some higher-order (waveguide) modes would have to be dealt with and additionally the solution is not suitable for all possible DUT dimensions. This concept is similar to the buried microstrip line and will be described in more detail.

### 3.1.1 Buried microstrip alternatives

There are existing commercially available test-fixtures or transitions (e.g. a test-fixture from Inter-Continental Microwave [29]) that utilize the concept of buried microstrip transmission line. It has been published [45] that for highly-integrated circuits, the buried microstrip configuration has major advantages in terms of lower crosstalk between two parallel microstrips. Similar effect has been utilized and published in the recent paper [44] which described *canyon*-like enclosure of the launcher with the adjacent microstrip line in order to suppress the radiation. The buried microstrip (see Fig. 10) reliably suppresses the radiation and crosstalk, but introduces some disadvantages that have to be explained.

### 3.1.2 Modal analysis

The buried microstrip concept proposed in [44] (originally named as *canyon* for its looks) can potentially introduce due to its configuration waveguide-like behavior. The concept is described in more detail and a modal analysis is done to explain the reason for the effective suppression of radiation.

Full-wave 3D electromagnetic field simulators (CST MWS and ANSYS HFSS) were used to analyze excitable modes in the test-fixture with buried microstrip (photograph

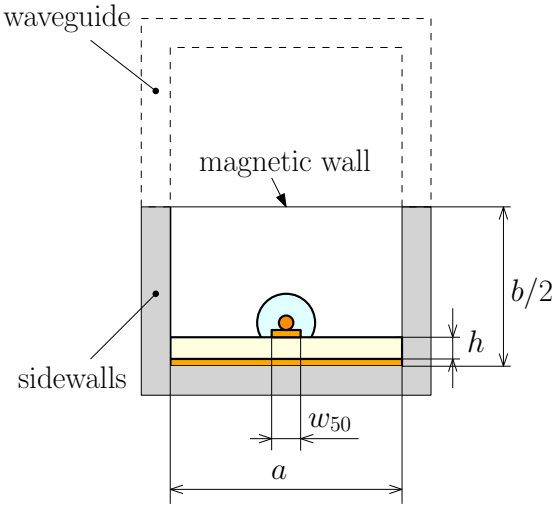


**Fig. 11** Cross section of the test-fixture illustrating the *canyon* configuration that is analogical to the buried microstrip. The possible waveguide configuration including the virtual magnetic wall is shown.

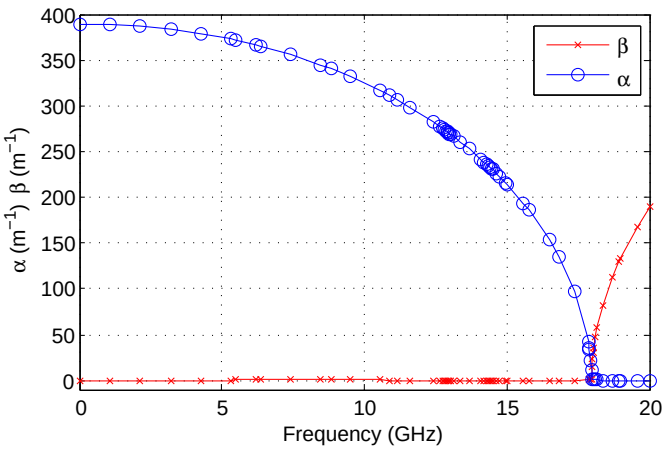


**Fig. 12** Simulated propagation constants $\beta$, $\alpha$ and their frequency dependence for the dominant waveguide mode which can be excited in the *canyon*. Frequency cutoff ($f_c$) can be estimated and it is dependent on the dimensions of the waveguide. In this case is $f_c \approx 17\,\mathrm{GHz}$.

of the device is in Fig. 10). The models are based on the schematic in Fig. 11. The dominant waveguide mode $\mathrm{TE}_{10}$ of theoretical rectangular waveguide with a *magnetic wall* has to be expected first, but it was observed that such ideal *magnetic wall* which is drawn in the schematic is not present thus another higher order modes have to be analyzed. First simulation results include important parameters such as propagation phase constant $\beta$ and attenuation constant $\alpha$ of single higher-order waveguide mode which can limit the usability of the proposed approach on higher frequencies (see Fig. 12).

One can determine the approximate cutoff frequency ($f_c$) of such mode according to the $\beta$ and $\alpha$ traces. Based on the Fig. 12 it is clear that the mode has its cutoff frequency around 17 GHz. This can be verified by performing more detailed analysis of this mode which can be excited in the test-fixture.

Hence more elaborate approach was undertaken and according to the electromagnetic field distribution it was observed that the second-order mode in the *canyon* is based on the $\mathrm{TE}_{11}$ mode [46] which can propagate in rectangular waveguides. The electric and

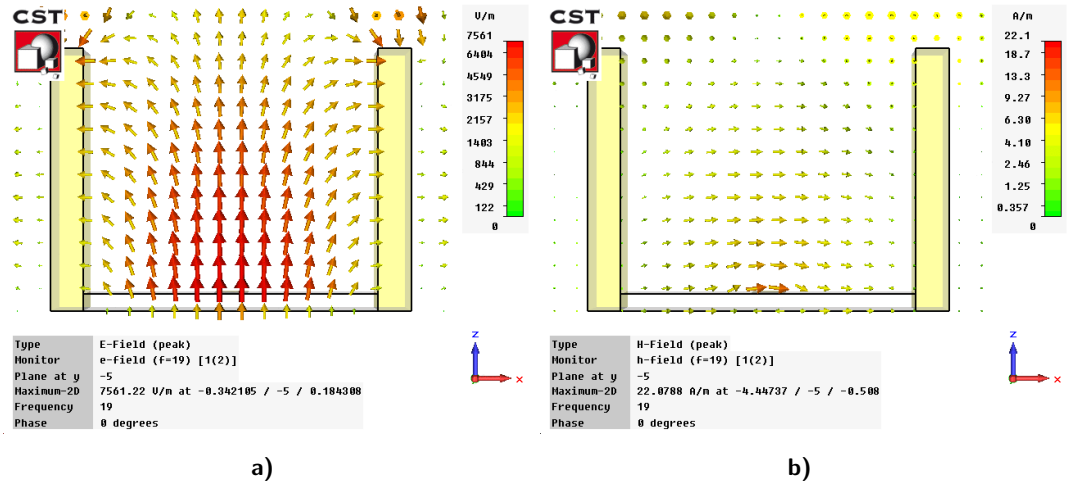


**Fig. 13** Electric (a) and magnetic (b) field distributions in the cross section of the *canyon*. Waveguide mode $\mathrm{TE}_{11}$ for this structure is above the cutoff frequency ($f = 19\,\mathrm{GHz}$).

magnetic field distributions of this mode are illustrated in Fig. 13. The simulation was done using CST Microwave Studio with its FEM frequency solver and waveguide port excitation.

It is worth noting that this approach is not perfect because it provides only approximate results compared to the real measurement. Main reason being that the excitation from an ideal waveguide port implemented in CST MWS is nonphysical and cannot be well recreated in the real measurement. Therefore these results can serve as a qualitative benchmark for the designed hardware components before the actual fabrication. The real influence of this mode is somehow distorted by the waveguide excitation.

To inspect the properties and performance of the buried microstrip test-fixture one can rely on 3D EM field simulations as well. The longitudinal section of the test-fixture with simulated electric field distributions on a single frequency is shown in Fig. 14. In the case with standard microstrip line (Fig. 14a), the radiated field which propagates from the launcher creates additional losses and interferes with the electric fields on microstrip line and with the microstrip open. This influences observable properties of the line and of the DUT (or the calibration standard). On the other hand, the influence of the buried microstrip in Fig. 14b can be seen as the radiated wave propagation is suppressed compared to the standard case. The electric field distribution resembles a classic microstrip QTEM mode, thus the interferences are minimized in this case.

It is possible to verify the simulation results from CST and increase the confidence in the proposed explanation by an analytical computation of the $f_c$ for the $\mathrm{TE}_{11}$ mode based on physical dimensions of the *canyon* test-fixture (see Fig. 11) using analytical formulas for waveguide cutoff. According to [46], to calculate the cutoff angular frequency for a rectangular waveguide, one can use the following equation:

$$\omega_{c_{m,n}} = \frac{1}{\sqrt{\mu\varepsilon}}\sqrt{\left(\frac{m\pi}{b}\right)^2 + \left(\frac{n\pi}{a}\right)^2} \tag{43}$$

The actual dimensions from the CST MWS 3D model can now be used and substituted into the formula. One can now compute the theoretical cutoff $f_{c_{1,1}}$ for the $\mathrm{TE}_{11}$ mode which would be excited in a perfect rectangular waveguide with the proposed

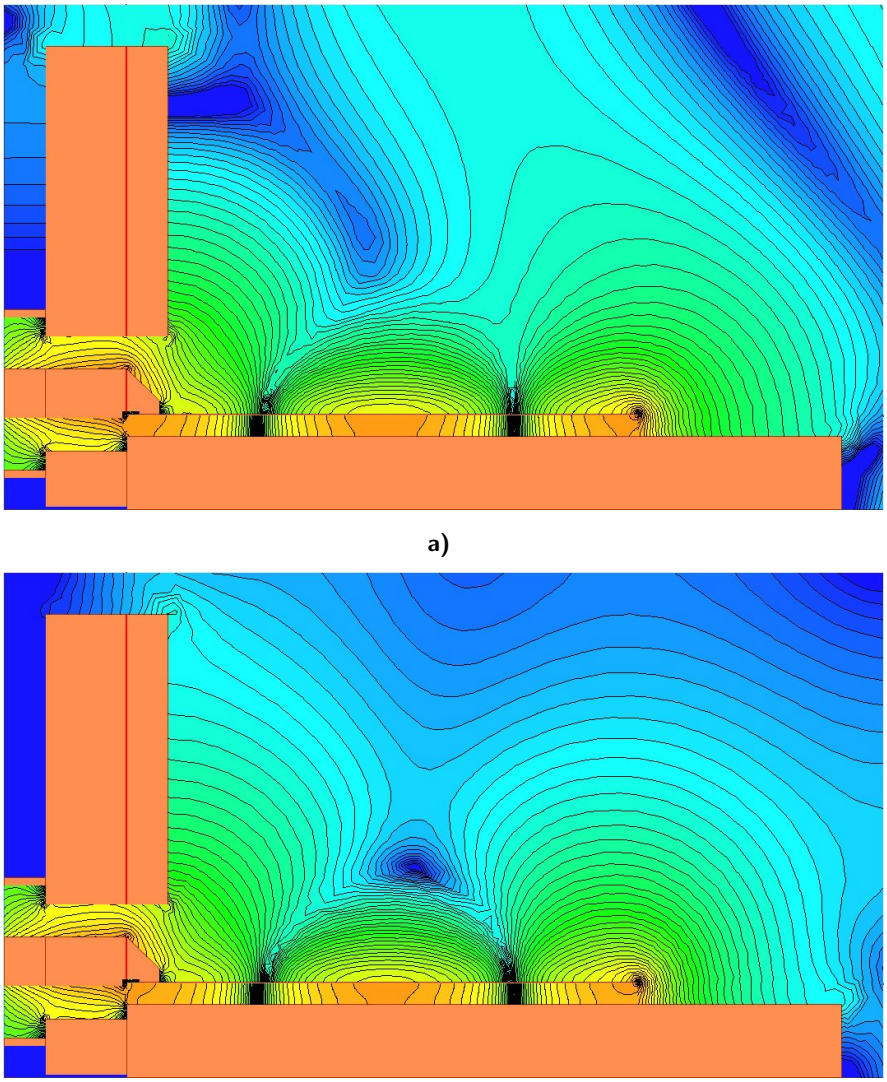


**Fig. 14** Electric field distribution in a longitudinal section of the test-fixture with a microstrip *open* calibration standard simulated in a unmodified assembly (a) and in the *canyon* structure (b) as well. The scaling of electric field and the phase of the excitation were preserved in both figures. Note the propagating radiated wave above the microstrip line in the first case.

dimensions. For the specific case of this simulated scenario, one will obtain:

$$f_{c_{1,1}} = \frac{1}{2\sqrt{\mu\varepsilon}}\sqrt{\left(\frac{1}{b}\right)^2 + \left(\frac{1}{a}\right)^2} = 18.34\,\text{GHz} \tag{44}$$

The value of 18.34 GHz is in correlation with the simulated results shown in Fig. 12 which plots the phase and attenuation constants versus the frequency. The difference between $f_{c_{1,1}}$ and simulated $f_c$ is caused mainly by two reasons. Relative permittivity of the microstrip substrate was not taken into account when evaluating effective permittivity inside the waveguide and secondly the fringing field effect at the top of the sidewalls effectively extends the height $b/2$ and this results in decreased cutoff frequency $f_c$ of the imaginary waveguide described with dotted line in Fig. 11.

There are other possible higher-order waveguide modes which could propagate in the test-fixture on frequencies higher than 20 GHz. This is beyond the scope of this

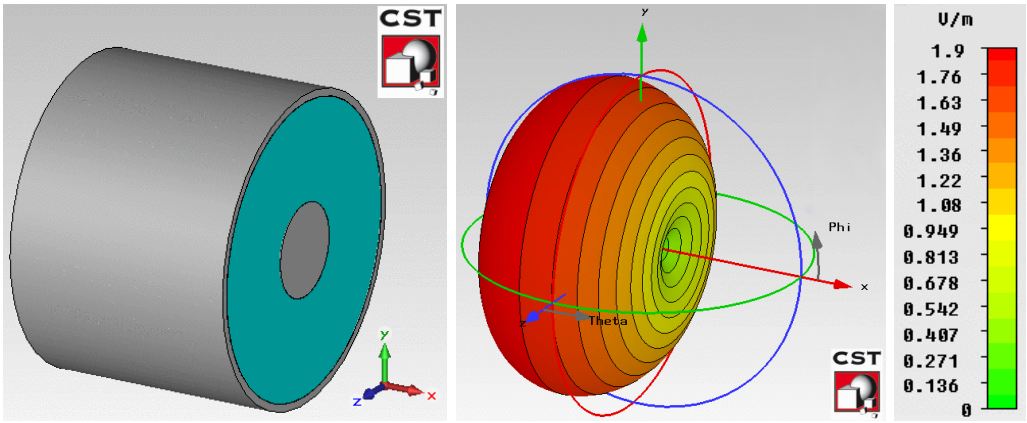


**Fig. 15** Simple open-ended coaxial-line and its far-field plot is shown in linear scale (V/m). Frequency was chosen to show the far-field in case of the largest radiated power (26 GHz). Incident power is 1 W.

section and some useful information and additional references can be found in the original paper [44] that proposed the idea. It is worth to note that despite the issues with higher order modes, the *canyon* configuration that effectively buries the transition between two ground planes proved itself to be effective in the radiation suppression. However, the usable bandwidth and higher order waveguide modes introduce limitations for practical use. The validation measurement results presented in the original paper were reproduced in similar conditions and are shown in the section A of the appendix.

Laminate substrate Rogers 4350b [47] $h = 0.508$ mm thick was used to fabricate the microstrip standards used for the validation measurement in the buried microstrip test-fixture. See Fig. 62, Fig. 63 and Fig. 64 in the appendix. The measurement results show that the suppression was indeed achieved, but for the understanding of the phenomenon, the problem is still in the beginning.

## 3.2 Analogy with open-ended coaxial line

This section presents an analysis that was done to understand the nature of the radiation from the transition and shows possible analogies with much simpler models. This analysis was already published by the author of this thesis in [48].

The idea behind this section can be summarized as follows. Let's say that we would like to find the simplest possible configuration that is related to the coaxial-to-microstrip transition, which could have also similar EM performance. From the most elementary point of view, one can say that the transition is just an open-ended coaxial line placed on top of some microstrip line. Due to the fact that the model of coaxial-to-microstrip transition is a rather complex structure, the problem will be explained on simplified models with progressively increasing complexity. This systematic process should help to understand the physics behind the radiation with use of advanced 3D EM full-wave simulation tools. The models were simulated and analyzed in the frequency range 0–26 GHz.

Firstly, the most basic approximation of a coaxial-to-microstrip transition from the radiation point of view can be based on an open-ended coaxial line with overlapping (i.e. extruded) inner conductor and a ground plane with some appropriate dimensions that would come from the transition model. But first, one has to start by looking at radiation properties of a simple open-ended coaxial-line without any modifications (i.e.

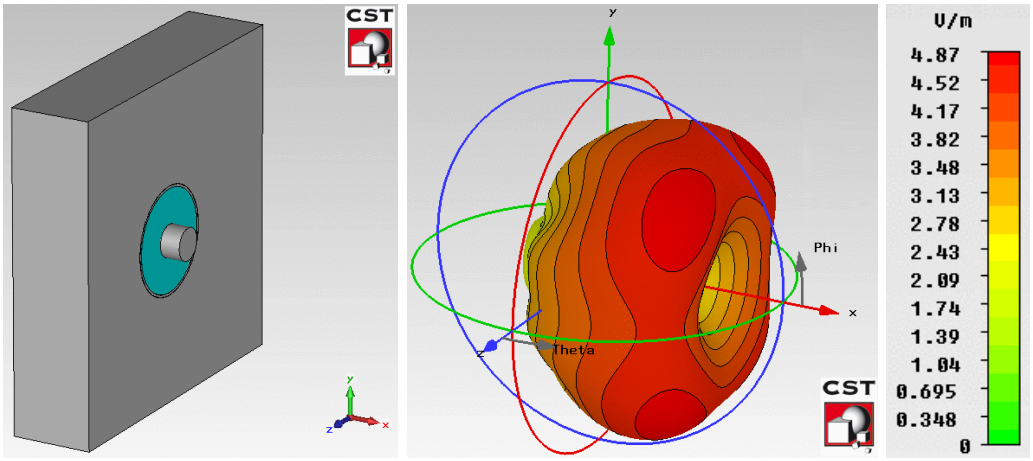


**Fig. 16** Simple open-ended coaxial-line with ground plane and extended inner conductor to a $\lambda/20 = 0.75\,\text{mm}$ (a). Respective far-field plot (b) is shown in linear scale (V/m). Frequency was chosen to show the far-field in case of the largest radiated power (26 GHz). Incident power is 1 W.

coaxial line with shielding and inner conductor cut in the same point), which is shown in Fig. 15. After performing the EM simulation of such model it becomes clear that this configuration has relatively small radiation efficiency, because the electric field is distributed mainly inside the coaxial line and the open-end capacitance is small.

This relatively simple antenna would start to increase its radiation efficiency with an overlap (extrusion) of the inner conductor, which would become significant at offsets similar to $\lambda/20$. This effect can be amplified by using an electrically significant ground plane that is perpendicular to the axial direction of the coaxial line (see Fig. 16). It is possible to illustrate the increased radiated power using 3D EM field simulations in CST Microwave Studio[1].

With this simple modification, it is possible to increase the coaxial open-end capacitance and also the radiation efficiency by factor of 4, that is also clearly visible in the comparison in Fig. 18. As this model is still far from being similar to the actual transition, the results are shown just to illustrate the significance of the inner conductor extrusion on the magnitude of EM field radiation. Notice that the radiation pattern has very similar shape and keeps its symmetry similarly as the basic open-ended coaxial line from Fig. 15.

To get reliable results and to see the qualitatively correct radiation properties which would be close to the actual geometry, it is necessary to improve the existing model shown in Fig. 16 by adding an electrical equivalent of the microstrip line to the transition. The microstrip line is modeled for the sake of simplicity with an air dielectric (other parameters are: $h = 0.254\,\text{mm}$, $w_{50} = 1.22\,\text{mm}$). Updated model with its simulated far-field radiation pattern is shown in Fig. 17.

The radiation pattern contains the first significant lobe in the elevation $\theta = 30°$ with 35° 3 dB beam-width. This is caused mainly by the presence of the microstrip ground plane, which steers the radiation characteristics to the upper area of the transition and forms a significant main beam. From the radiation efficiency point of view, this

[1]The CST Microwave Studio in version 2012.05 was used. Perfectly matched layer (PML) is used as a boundary condition for the CST frequency solver in all directions of the models. Adaptive meshing convergence limit was set to 0.001 and broadband frequency interpolated sweep convergence limit was set to 0.0005. These settings apply for all following CST simulations in this section.

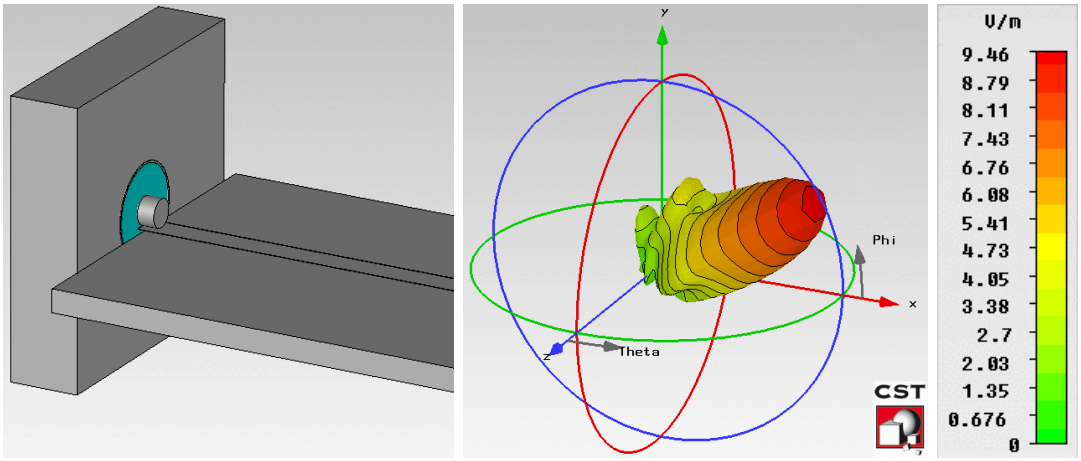


**Fig. 17** Coaxial-to-microstrip transition model with an air dielectric perfectly-matched microstrip line (a) which has overlapping inner conductor to a $\lambda/20 = 0.75\,\text{mm}$ from the end of the coaxial line. The far-field plot (b) is displayed in linear scale (V/m). Frequency was chosen to show the far-field in case of the largest radiated power (26 GHz).

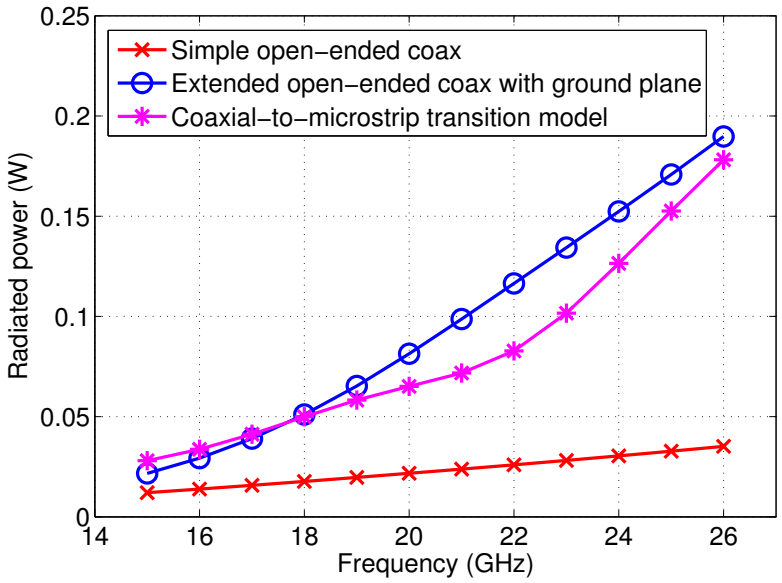


**Fig. 18** Radiated power as a function of frequency from simple open-ended coaxial line (Fig. 15), extended coaxial line with ground plane (Fig. 16) and coaxial-to-microstrip transition model (Fig. 17). Incident power is 1 W in all cases.

model has very similar properties as the simplified model (see Fig. 16). This can be demonstrated by simulated radiated power for all examined models which is shown in Fig. 18. It is possible to say that the transition model shows similar magnitude of radiated power while having more focused radiation pattern.

The presented results give the author good confidence in the validity of the proposed analogy of radiation from the coaxial-to-microstrip transitions that have similar properties as an open-ended coaxial line with extruded center conductor. In the following section possible issues that arise with this radiation phenomenon are introduced.

## 3.3 Synthetic data tests

Before introducing the description of a radiation influence on any selected calibration technique, several paragraphs will be presented that describe a testing methodology of the radiation influence evaluation on any results obtained with some specific calibration algorithm. Some of the frequently used calibration techniques that are generally regarded as state-of-the-art will be described and tested in this section.

### 3.3.1 Calibration method

Suitable planar calibration method has to be chosen that will provide the most satisfying results for planar calibrations in general. Suitability of each technique can be evaluated in various ways. One of the most convenient ways utilizes software package – for example the VNA Tools II published by the Swiss measurement institute METAS [13]. This software provides many convenient features for testing purposes, particularly:

- measurement setups with remote VNAs connected via ethernet/GPIB
- the Test VNA with arbitrary noise, linearity and uncertainty parameters
- calibration kit database with S-parameter based or Agilent polynomial definitions and arbitrary uncertainty in amplitude and phase
- uncertainty propagation through the measurement setup into the corrected results
- various calibration techniques with 12-term or 8-term error models including switch terms
- uncertainty calculation of connector repeatability and cable movement stability
- calibration/correction performed on any arbitrary data set with S-parameter plots including uncertainty bounds (standard and expanded) for magnitude and phase

This software package provides some vital tools for many engineering tasks and simplifies the task of testing and evaluating new calibration kits or performing a synthetic measurement itself. Thanks to the free availability of this package, it creates the possibility to easily reproduce the presented results by different researcher without the need for implementation of the specific calibration algorithm with uncertainty propagation included.

### 3.3.2 Suitability of match standard for planar calibrations

The virtual measurement equipment *Test VNA* that is implemented in VNA Tools II has been used in this section to make a quantitative comparison among various 1-port calibration approaches where some of them use the calibration match standard with SMD resistors soldered onto the printed circuit board (PCB). The calibration procedure relies only on the VNA Tools II software and on the CST MWS simulation results of the raw data and calibration standards data.

Custom-built Grounded Coplanar Waveguide (CPWG) calibration kit that was developed and simulated in CST Microwave Studio that is suitable for 2.92 mm Southwest Microwave Endlaunch connectors [49] was available for the following test. For the purpose of testing the common techniques this calibration kit and its CST models were used. Open, short and match standards from this kit are depicted in Fig. 19. An overall picture including the model of Southwest Microwave endlaunch is shown in Fig. 19 to give the reader a sense of scale – this actual model with the transition was not used during the presented synthetic test.

A classical 1-port OSM calibration utilizing 50 Ω match, open and short standards was performed in the first step with an internal linear error model associated with the

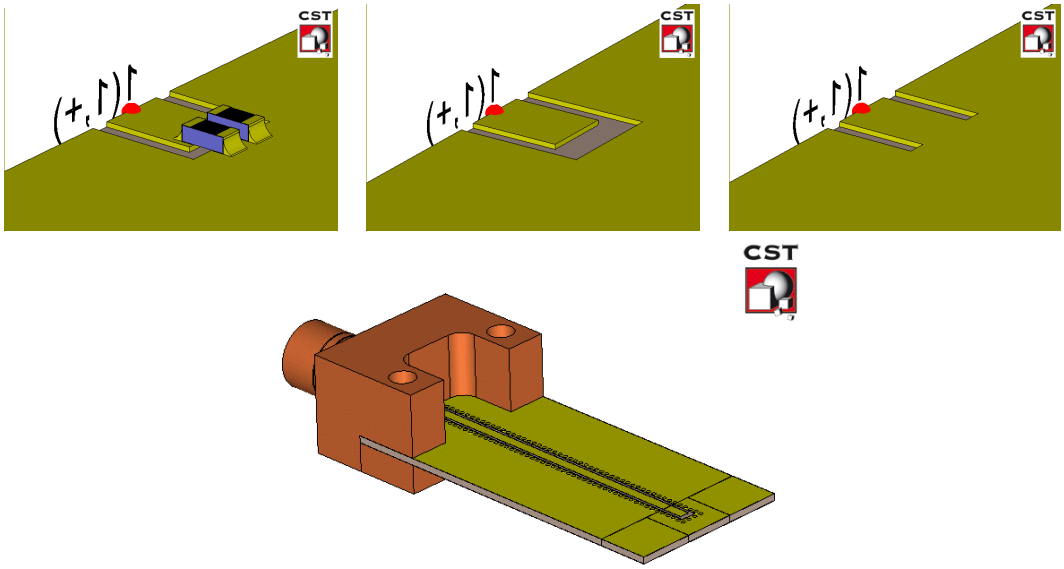

**Fig. 19** Grounded Coplanar Waveguide (CPWG) calibration kit models drawn in CST Microwave Studio.

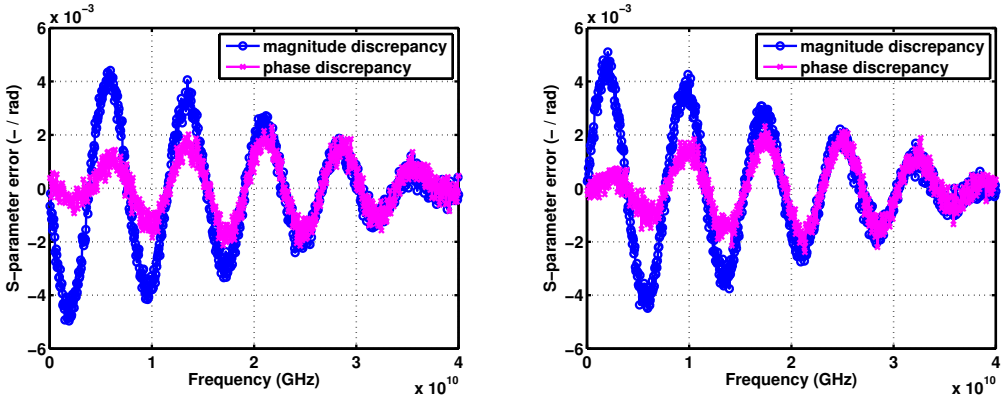


**Fig. 20** Verification of OSM calibration ($Z_{\mathrm{match}} = 50\,\Omega$) using 12.5 mm open (a) and short (b) CPWG line. Simulated line impedance $Z_0 = 47.9\,\Omega$

Test VNA itself and some random noise errors added to the synthetic data. The random noise was included in the Test VNA to simulate a real-world measurement as closely as possible. The verification with a CPWG open and short with offset 12.5 mm from the reference plane was performed. These results are plotted in Fig. 20. The discrepancy between expected (CST MWS model simulation of the verification DUT) and virtually *measured* (corrected data from VNA Tools) are shown in both magnitude/phase for 12.5 mm CPWG open, short elements.

The discrepancy that was obtained was eventually traced down to be caused by the incorrect impedance of the match standard used for the calibration. Due to the fact that the simulated impedance of the CPWG transmission line in CST MWS (an average value of 47.9 Ω) differed from the desired 50 Ω impedance, the correction does not produce valid and satisfying results.

This effect can be analogically translated into a manufacturing error during fab-

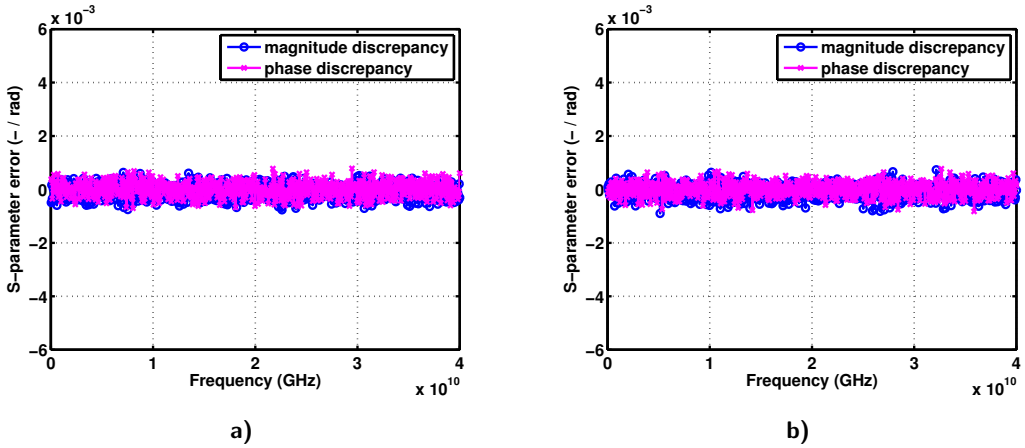


**Fig. 21** Verification of OSM calibration ($Z_{\mathrm{match}} = 47.9\,\Omega$) using 12.5 mm open (a) and short (b) CPWG line. Simulated line impedance $Z_0 = 47.9\,\Omega$

rication and etching of the CPWG board that would introduce some degree of the impedance discrepancy. In this specific case, the actual impedance of the CPWG line was smaller than the match standard. Different results would be obtained in the opposite case.

In the following step, the match standard was re-designed and re-simulated to have as closest value as the real impedance as the CPWG line (approx. $47.9\,\Omega$) and the calibration was performed again. Note that due to dispersive characteristics of the impedance of the line, some residual error in very broad frequency band will remain, this error can be neglected for this scenario. Results (see Fig. 21) show significantly reduced discrepancy between expected and *measured* traces down to the level of the arbitrary chosen added noise of the Test VNA. The scale of the y-axis was preserved to correspond with the previous results.

These plots validate the algorithm and show the ideal achievable results that do not include any additional repeatability or other random errors that would be present in real-world scenario. This test revealed some potential issues that would occur during the real-world calibration with the original match standard and with a help of sophisticated simulation tool allows to do some additional changes in the design before the fabrication itself.

The conclusion from this test can be drawn such as the match calibration standard would have to be redesigned in practice to allow for some post-fabrication correction to account for the real impedance of the fabricated transmission line. It is however not practical to use very accurate values of the SMD resistors and synthesize arbitrary match standard that would precisely match the line impedance. Another possible way is to avoid the match calibration standard and use offset open/short standards. This solution will provide the impedance of the transmission line to the algorithm which then serves as the offset standard and therefore the calibration algorithm is not sensitive to the variations of the fabricated impedance of the line versus the match standard.

### 3.3.3 Offset standards for planar calibrations

Another calibration algorithm results using an over-determined (open, short, offset open, offset short) calibration with 1 mm offset length are shown in Fig. 22. Due to the absence of the match standard, the impedance at the calibrated reference plane is

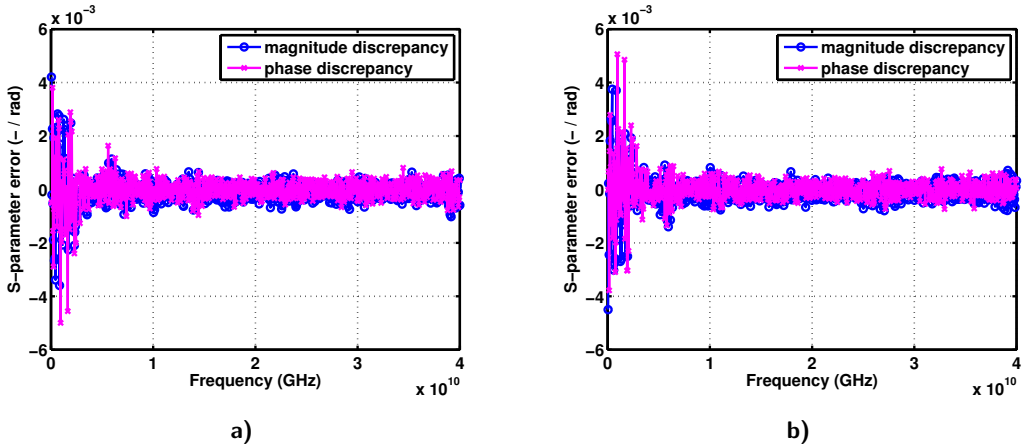


**Fig. 22** Over-determined (open, short, offset open, offset short) calibration verification using 12.5 mm open (a) and short (b) CPWG line.

based on the line impedance of the offset standards. The arbitrary chosen offset length introduces bandwidth limitations[2].

Due to the fact that the length difference of 1 mm is frequency dependent, it translates into different phase offsets on each frequency. It is known that both standards have to be independent otherwise the system of equations would not produce reasonable results. 1 mm becomes exactly half-wavelength on a 86 GHz (considering $\varepsilon_{eff} = 3$), thus making this offset length unusable on such frequency. On the other hand, 1 mm is just a fraction of wavelength on low frequencies (approx. $0 \sim 3$ GHz), thus it is becoming an issue of discriminating between two standards with this offset length on very low frequencies.

The effect of the limited bandwidth on the calibration method can be seen in Fig. 22 in the lower frequencies as increased discrepancy of the verification measurement.

It is worth to mention here, that it would be sufficient to use only three calibration elements (e.g. open, short, offset open – OSO) for a 1-port measurement to satisfy the mathematical requirements if the bandwidth limitation is not an issue. However, the advantage of the over-determined calibration over an OSO approach can be demonstrated in Fig. 23 in terms of calculated uncertainty in the corrected data using the VNA Tools II software.

Mean values of expanded uncertainty for magnitude of $S_{11}$ of both verification elements are:

- $6.2^{-3}$ for OSO calibration
- $1.5^{-3}$ for over-determined technique with 4 standards

The over-determined technique qualitatively and also quantitatively reduces (by more than factor of 3) the uncertainty within the measurement. It seems to be beneficial in terms of accuracy and ease of calculation. Thanks to low demands on calibration standards it is highly suitable and sufficiently accurate for experiments with radiation phenomenon. And finally, it does not require to have a match standard which was demonstrated to introduce some calibration issues and problems with matching its impedance with the impedance of the transmission line.

[2]These limitations can be significantly reduced by choosing appropriate offsets or by using multiple offset standards.

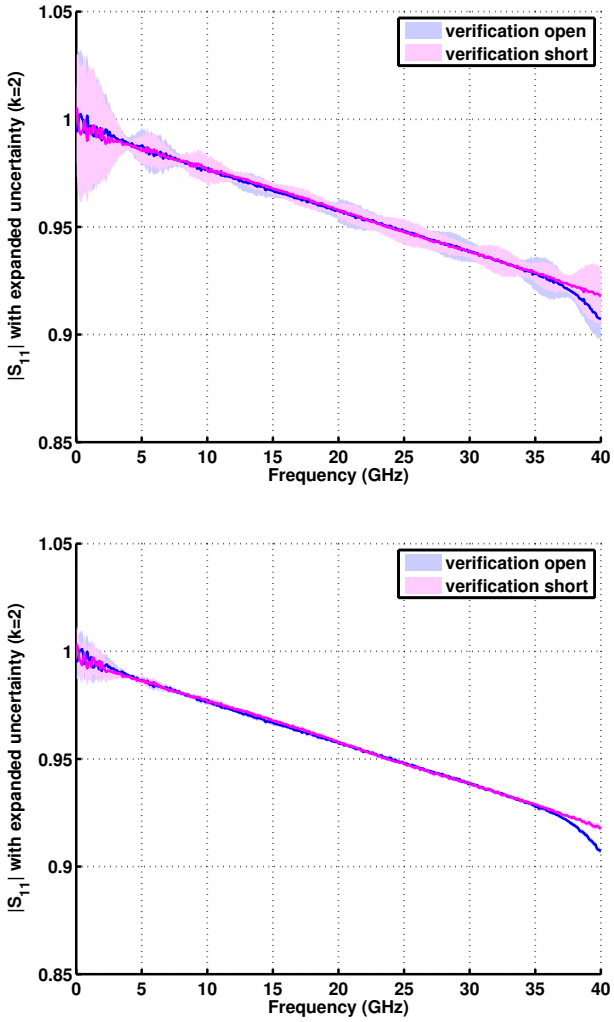


**Fig. 23** Comparison between OSO (open, short, offset open) calibration (a) and over-determined (open, short, offset open, offset short) calibration (b) in terms of expanded uncertainty (95% coverage factor) of measured verification elements (12.5 mm open and short CPWG line).

### 3.3.4 Over-determined offset open technique

This section presents measurement examples with relatively modern and reasonably elaborate over-determined 1-port calibration technique similar to the work presented by J. Hoffmann *et al.* [41] that was implemented in MATLAB environment for this purpose. Both raw measurement data for the DUT $S_{M_k}$ and calibration standards data $\Gamma_\mathrm{L}$ were obtained using CST Microwave Studio simulations with the intention of including all the radiation effects to see the impact on the calibration. This technique will be referred as *synthetic* data test.

The lossy copper microstrip line used in the CST is calculated to have 50 Ω impedance at center frequency 10 GHz on Rogers Corp. 4350b [47] substrate 0.508 mm thick. Perspective view on the CST model is shown in Fig. 24.

The method [41] uses several offset shorts with known lengths and value of reflection coefficient. The over-determined set of equations is solved by means of `lsqnonlin()` to obtain not only the error model matrix **E**, but the phase constant $\beta$ of the transmission

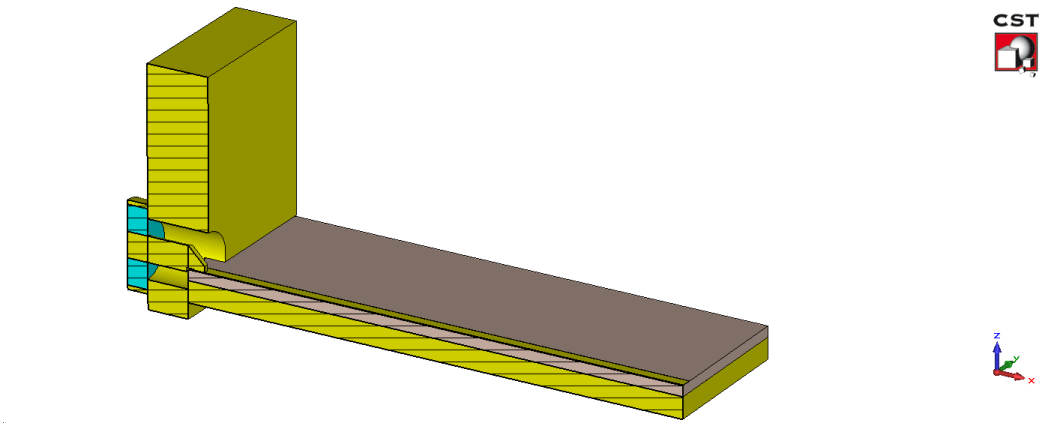

**Fig. 24** CST Microwave Studio model with open-ended microstrip line that was used to verify the radiation hypothesis.

line as well. This can be done due to the fact that the over-determined nature of this technique provides some remaining knowledge introduced with the redundant set of measurements that can be used to evaluate one additional real-valued unknown parameter (i.e. $\beta$ in this case) on each frequency.

Presented method was slightly modified compared to the original paper; five microstrip offset open standards (15-19 mm) with known parameters are used in the first step, just to perform classical over-determined 1-port OSM [4]. The basic matrix equation for the 1-port OSM can be written as:

$$\mathbf{A} \cdot \mathbf{E} = \mathbf{b} \tag{45}$$

which one has to solve for $\mathbf{E}$ on each frequency. The over-determined calibration can have $n$ standards (generally more than three) which will yield $n$ measured reflection coefficients $\Gamma_{\mathrm{m}n}$ along with their known values $\Gamma_{\mathrm{a}n}$. The matrix equation 45 can be rewritten according to [4] that yields:

$$\begin{bmatrix} 1 & \Gamma_{\mathrm{m}1}\Gamma_{\mathrm{a}1} & -\Gamma_{\mathrm{a}1} \\ 1 & \Gamma_{\mathrm{m}2}\Gamma_{\mathrm{a}2} & -\Gamma_{\mathrm{a}2} \\ 1 & \Gamma_{\mathrm{m}3}\Gamma_{\mathrm{a}3} & -\Gamma_{\mathrm{a}3} \\ \vdots & \vdots & \vdots \\ 1 & \Gamma_{\mathrm{m}n}\Gamma_{\mathrm{a}n} & -\Gamma_{\mathrm{a}n} \end{bmatrix} \cdot \begin{bmatrix} e_{00} \\ e_{11} \\ e_{00}e_{11} - e_{10}e_{01} \end{bmatrix} = \begin{bmatrix} \Gamma_{\mathrm{m}1} \\ \Gamma_{\mathrm{m}2} \\ \Gamma_{\mathrm{m}3} \\ \vdots \\ \Gamma_{\mathrm{m}n} \end{bmatrix} \tag{46}$$

With this complete matrix equation, one can then solve for $\mathbf{E}$ using for example a `mldivide()` in Matlab.

After this straightforward step, one obtains terms $e_{00}$, $e_{11}$ and $e_{10}e_{01}$ that can be used for the following calculation as initial starting values of the error model. Main disadvantage is in the fact, that one does not obtain any additional data except the error model S-parameters $S_E$. It is of course possible to use the obtained values to perform a standard 1-port correction at this point.

In the next step, the calibration technique will exploit the fact, that each microstrip open is connected to a microstrip line with different (previously known) length, but having the same propagation constant (i.e. parameters $\beta$ and $\alpha$). Thus one can provide the offset lengths between each standard to a microstrip line model [50] and cascade

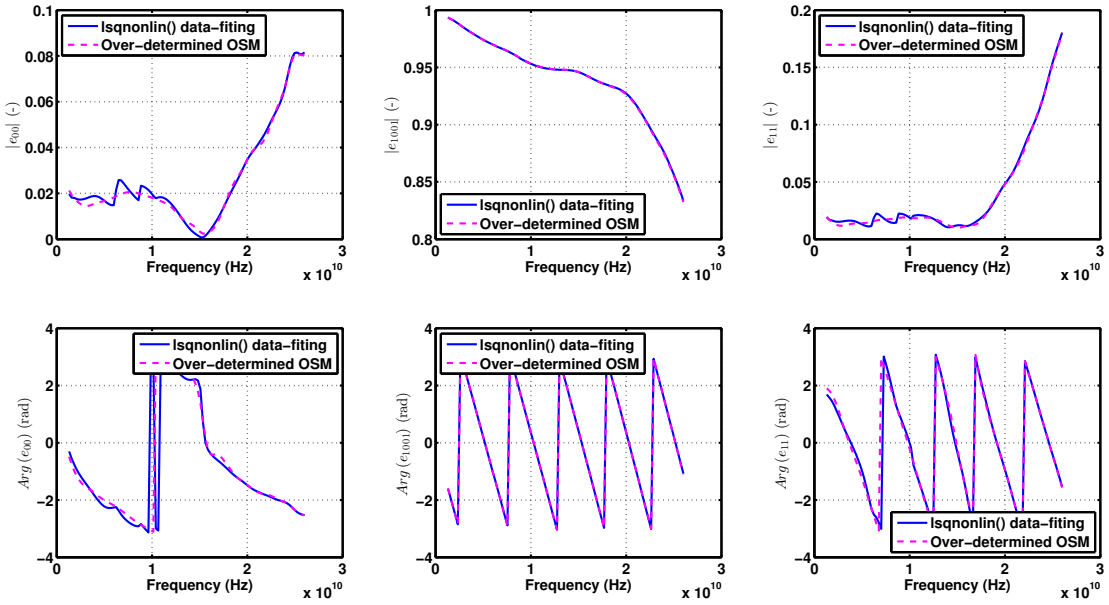


**Fig. 25** Comparison between complex error model parameters (magnitude and phase) calculated with classic over-determined OSM and `lsqnonlin()` data-fitting approach. Even though good quality OSM results were used as initial values for the data-fitting algorithm, noticeable discrepancy appears at lower frequencies.

such microstrip line (defined by propagation constant $\gamma$) with the S-parameters of the microstrip open (that is the same for each standard – $\Gamma_\mathrm{L}$).

Thanks to the over-determined nature of the system, one can use the additional information from the measurements to solve for more variables (e.g. phase constant of the microstrip line $\beta$) than just for error model parameters. There are successful calibration scenarios [41], where this technique yields satisfying results. There are some limitations associated with this approach and are discussed in the referenced paper.

The calibration algorithm tries to meet the following equation:

$$T_{M_k} = T_E T_{S_k} \tag{47}$$

where $T_{S_k}$ and $T_E$ is a T-matrix of $S_k$ and $S_E$ respectively. It is possible to acquire $T_{M_k}$ (i.e. $S_{M_k}$) by measuring $k$ offset (short) open with variable length $l_k$ and S-matrix $S_k$:

$$S_k = \begin{pmatrix} \Gamma_\mathrm{L} e^{-2\gamma l_k} & 1 \\ 1 & 0 \end{pmatrix} \tag{48}$$

Propagation variables $\beta$ and $\alpha$ calculated using [50] can serve as good estimates for the algorithm. Reflection of all open standards $\Gamma_\mathrm{L}$ is calculated by CST Microwave Studio. Finally, initial estimates for error model parameters T-matrix $T_E$ can be used from previous standard 1-port OSM calculation (Equation 46). The calibration algorithm then tries to find all the values for unknowns ($\beta$, $\mathbf{E}$) that would meet the equation 47.

Comparison between error model parameters calculated with classic over-determined OSM and `lsqnonlin()` data-fitting is shown in Fig. 25. Some comments should be made to clarify the results. Firstly, there is a noticeable discrepancy on lower frequencies due to mutual distance of the offset standards in the complex plane inside the Smith chart. This effect increases the uncertainty of the algorithm but fortunately the discrepancy in the error terms $e_{00}$ and $e_{11}$ does not affect the correction as it will be

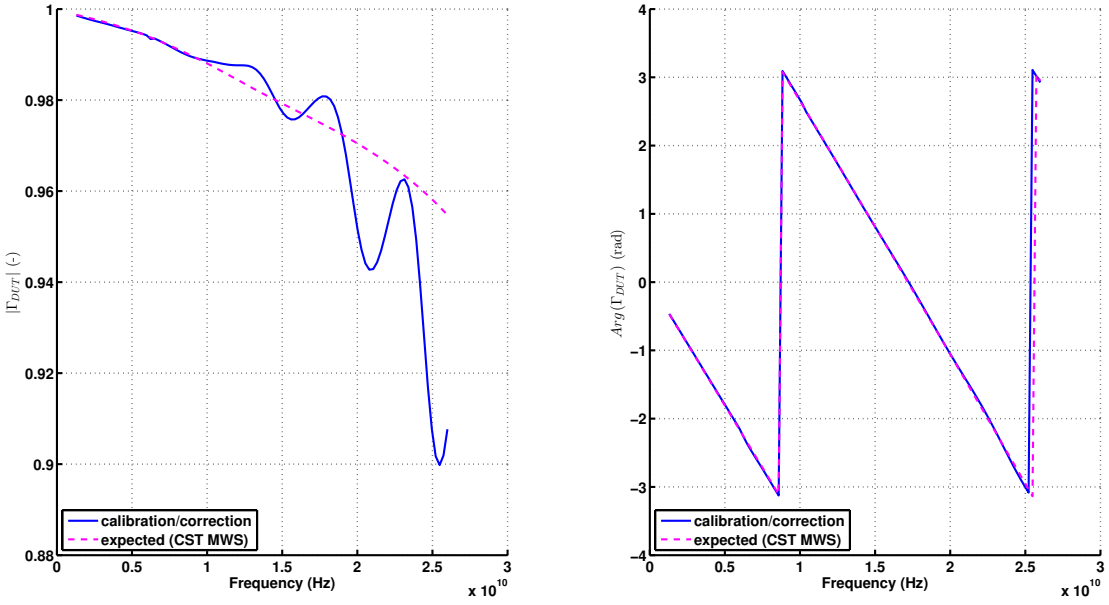


**Fig. 26** Verification of the calibration using microstrip open with 5 mm offset from the reference plane.

shown in verification data. It should be mentioned that the robustness of this method is dependent on the initial values of each variable (i.e. optimization starting point). Thus it can show various degree of robustness, especially in the lower frequency band, where the offset lengths are too short in relation to wavelength.

To perform a one-port correction with established values of error model $S_E$, one can substitute to the following equation:

$$\Gamma_{\mathrm{DUT}} = \frac{S_{\mathrm{M_{DUT}}} - e_{00}}{(S_{\mathrm{M_{DUT}}} e_{11}) - \Delta_E} \tag{49}$$

Qualitative verification of the calibration is performed (see Fig. 26). For this purpose, one (previously unused) offset open calibration standard is used. Trace is compared to the expected trace which is calculated using CST MWS.

Increasing discrepancy in magnitude of $\Gamma_{\mathrm{DUT}}$ (Fig. 26) is caused by the radiation. Due to the measurement being synthetic, there are repeatability and noise levels that cannot be matched during real world experiment. In this particular scenario and combination of transition and microstrip line (Fig. 24), the radiation losses cause an error in magnitude of reflection coefficient in order of three hundredths. Notice that the verification trace perfectly agrees with the expected trace up to approx. 10 GHz – this increases the confidence that this characteristic discrepancy between both traces is caused by the radiation.

The another advantage of the calibration algorithm [41] used for this synthetic test is the possible evaluation of transmission line's phase constant while performing a calibration. The trace in Fig. 27 shows $\beta$ obtained by Hammerstad-Jensen model compared to the value fitted with `lsqnonlin()` algorithm. The initial estimate for the algorithm was intentionally adjusted to have 10% deviation from Hammerstad-Jensen value in order to see if the algorithm is capable of fitting the correct value. The algorithm fails to fit the $\beta$ on lower frequencies while on higher frequencies the fit correctly agrees with the model. This may be useful for measurement on poorly characterized substrates with uncertain knowledge in their relative permittivity.

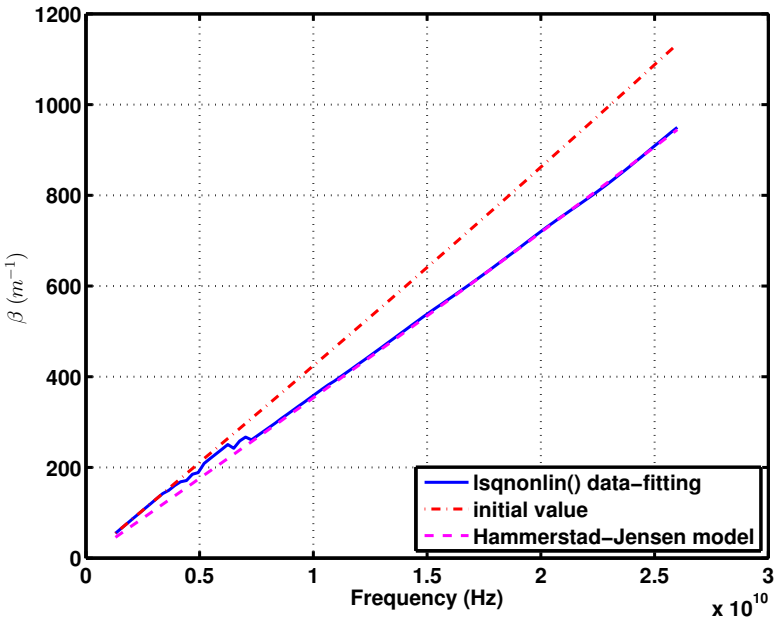


**Fig. 27** $\beta$ on microstrip calculated using `lsqnonlin()` data-fitting compared to initial values provided as estimation for the algorithm and to the results from Hammerstad-Jensen microstrip model.

The following chapter will discuss experimental quantification of the radiation using custom-designed two-port test boards with back-to-back transitions. Possible modeling approach will be shown as well.

# 4 Experimental quantification of the radiated wave

It has been recently discovered [30, 44, 36] and claimed in this thesis that it is important to evaluate the launcher's radiation under condition of a large voltage standing wave ratio (VSWR). The previous attempts [30, 44] to evaluate the radiation influence during the on-planar measurement relied on a calibration/correction technique of some sort. Authors used a verification element (usually some highly-reflective calibration standard with an offset length from the calibration reference plane). In the previous section, the radiation was qualitatively identified using a synthetic tests relying only on the simulated data. The real-world experiments are needed as well to confirm the findings.

It turns out that the calibration/correction validation is usually not accurate enough because one would obtain a calibrated VNA with some residual source match $e_{11_{\text{eff}}}$ [2, 19, 20] and radiation errors combined that cannot be separated anymore. The ripple in the verification results from [30] is constituted by multiple contributing factors and does not show just the radiation error influence. Notice the diagram in Fig. 28 that explains the effective error model effect on the calibrated/corrected data. If the term $S_{11}e_{11_{\text{eff}}}$ cannot be neglected it will produce noticeable ripple in the verification results even without the radiation effects.

## 4.1 The setup

Therefore some different experimental approach is needed and was recently proposed and presented in [38, 39]. This method relies on a precise calibration at the coaxial connector reference plane (that is reasonably easy to attain) and then requires to perform a raw measurement of a transmission coefficient $S_{21}$ (see Fig. 29) with the calibrated VNA. The term $S_{21}$ that is equal to $b_2/a_1$ contains the crosstalk component transmitted between both transitions. This approach offers several advantages:

- One does not have to rely on a precise calibrated reflection measurement which would not be as accurate as the transmission measurement, as can be proved in

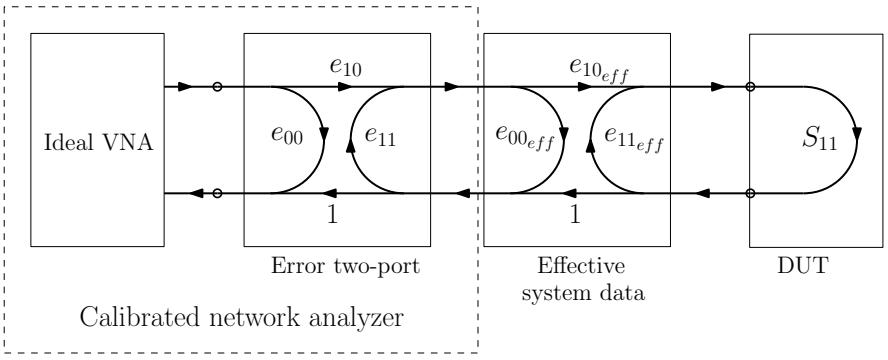


**Fig. 28** 1-port VNA calibration error-model with values of the calculated raw systematic errors $e_{00}$, $e_{10}$ and $e_{11}$ together with the residual effective error elements $e_{00_{\text{eff}}}$, $e_{10_{\text{eff}}}$ and $e_{11_{\text{eff}}}$.

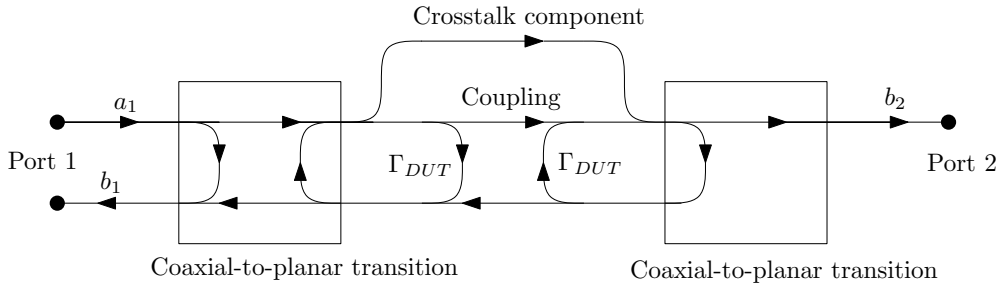


**Fig. 29** Signal flow graph of the experimental evaluation method of quantifying the residual crosstalks between the transitions under the condition of a large VSWR caused by highly reflective calibration standard ($|\Gamma_{DUT}| \approx 1$).

various VNA uncertainty specifications [51].

- The results are not influenced by residual errors in on-planar open-short-match (OSM) calibration which is considerably more elaborate and more demanding on the precision of the fabrication and exact knowledge of the calibration standards.
- Both coaxial-to-microstrip transitions can be subjected to a large VSWR with this configuration, thus the characteristic frequency-dependent radiation pattern will occur in the data.

There are several disadvantages that have to be mentioned as well:

- Results of the crosstalk component would contain only part of the radiated energy that propagates from the launcher in the forward direction and can be received by the second launcher inside the DUT.
- The crosstalk component would be superimposed to the coupling between the back-to-back discontinuities separated by a gap in the transmission line. This can be minimized by sufficient separation of the discontinuities.
- Demands on the simulation accuracy that would be performed using the 3D full-wave simulators and on their settings would be high as the magnitudes of the crosstalk would be in order of $10^{-3}$ in the linear scale. This is also true for demands on the measurement precision and setting of the VNA.

The measured wave ratio $b_2/a_1$ consists of the crosstalk between launchers combined with the intrinsic coupling between the reflective standards. These values are influenced by imperfections (reflections) at the coaxial connectors which can be omitted for the first approximation. The crosstalk and the coupling will produce a superimposed wave quantity that should be dependent on the electric length of the DUT.

## 4.2 Physical background

The VNA calibrated at the coaxial connector reference planes and commercially available coaxial-to-coplanar transitions from Southwest Microwave [49] are assumed. During any planar calibration it is common to use fully or partially known reflection standards which are usually assumed to be the same at both ports. Let's make an assumption that the large magnitude of VSWR at the transition causes the launcher to excite a spherical wave. The radiated wave which is excited at the transition is propagating along the transmission line with different properties and wavelength compared to the QTEM wave. This produces interferences between the common QTEM mode and radiated wave above the transmission line (in-depth analysis of this phenomenon is presented in [44, 48]).

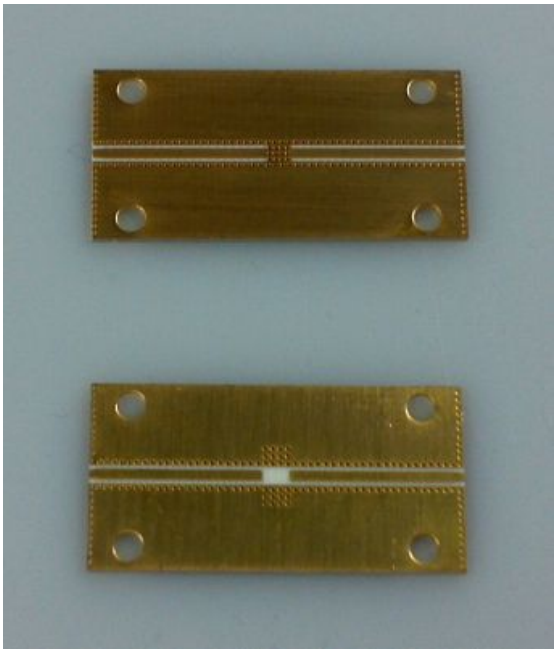

**Fig. 30** Reflective *short* and *open* CPWG boards usable for a planar TRL or OSM calibration designed on a 0.508 mm thick Rogers 4350b substrate with $\varepsilon_r = 3.66$. Overall dimensions are 25 × 12.7 mm.

Therefore if one wants to measure a reflection standard (usually *open* or *short*), different properties of the measured standard are obtained, simply by changing its position along the transmission line and this corrupts the calibration. Additionally, the varying distance from the launcher changes the standing wave distribution, therefore the radiation and interference properties along the fixture and the magnitude of measured crosstalks varies as well.

## 4.3 Experimental quantification

Two reflective calibration standards are usually designed on a single PCB (see Fig. 30) which makes it suitable to perform a calibration of both ports of the two-port VNA simultaneously and reduce the number of re-connections. Raw measured S-parameter $S_{21}$ of this set-up contains a coupling between two discontinuities and the crosstalk between the launchers as explained earlier (see Fig. 29). Using this information, the radiation and crosstalk between the transitions under different conditions (phase of reflected wave, distance from the discontinuity, etc.) can be evaluated. This method allows to estimate and quantify the radiated power in order to choose the best combination of the transitions and substrate and to avoid and minimize the radiation effects.

### 4.3.1 Raw measurement

To verify the proposed method a measurement set-up was carefully prepared to eliminate all potential systematic errors. Two sets of measurements were performed on the R&S ZVA-67 VNA in the frequency range 45 MHz - 40 GHz with a 100 Hz IF bandwidth. The coaxial calibration was performed using 2.92 mm coaxial calibration kit. The assembly repeatability of the calibrated measurement (i.e. repeatable mounting of the transition to the CPWG evaluation board) was better than 0.002 in the whole

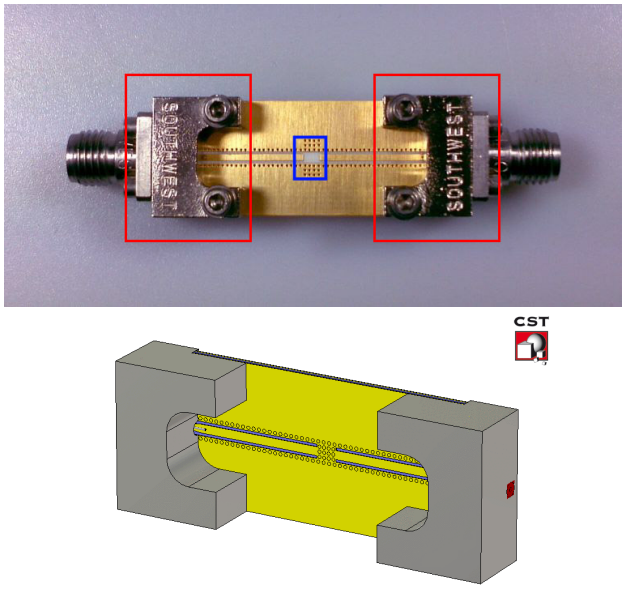


**Fig. 31** Evaluation test board and its CST model with reflective calibration standards (blue) usable for planar TRL or OSM calibrations. Southwest endlaunches (red) [49] are utilized as transitions from coaxial line to CPWG.

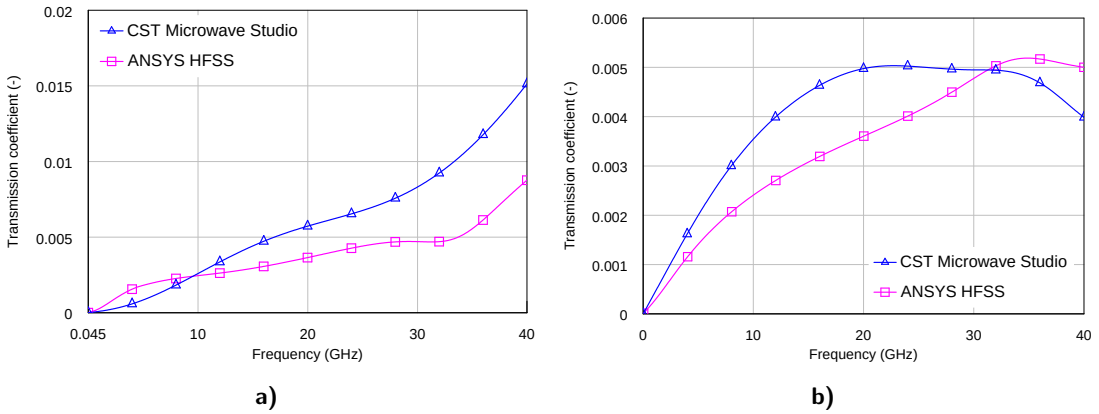


**Fig. 32** Comparison between the simulated results of the coupling for two *open* (a), *short* (b) discontinuities on CPWG PCB separated by a defined gap 1.8 mm long. Simulation done with ANSYS HFSS and CST MWS.

frequency range of this experiment. The repeatability of the coaxial connector assembly can be neglected altogether.

The intrinsic coupling between the reflective calibration standards cannot be easily acquired experimentally without influencing the measurement results with residual errors stemming from problematic calibration and correction on planar transmission line. Therefore one has to rely on 3D EM field simulations to obtain the coupling data – in this case performed using ANSYS HFSS electromagnetic field full-wave FEM solver as well as CST Microwave Studio's FEM frequency solver. The comparison of the simulated coupling for different discontinuities is shown in Fig. 32. At this scale of numerical precision, there are noticeable discrepancies between both simulators that can originate from differences in the implementations. Achieving better correlation from the same model with both simulators would be challenging and time-consuming.

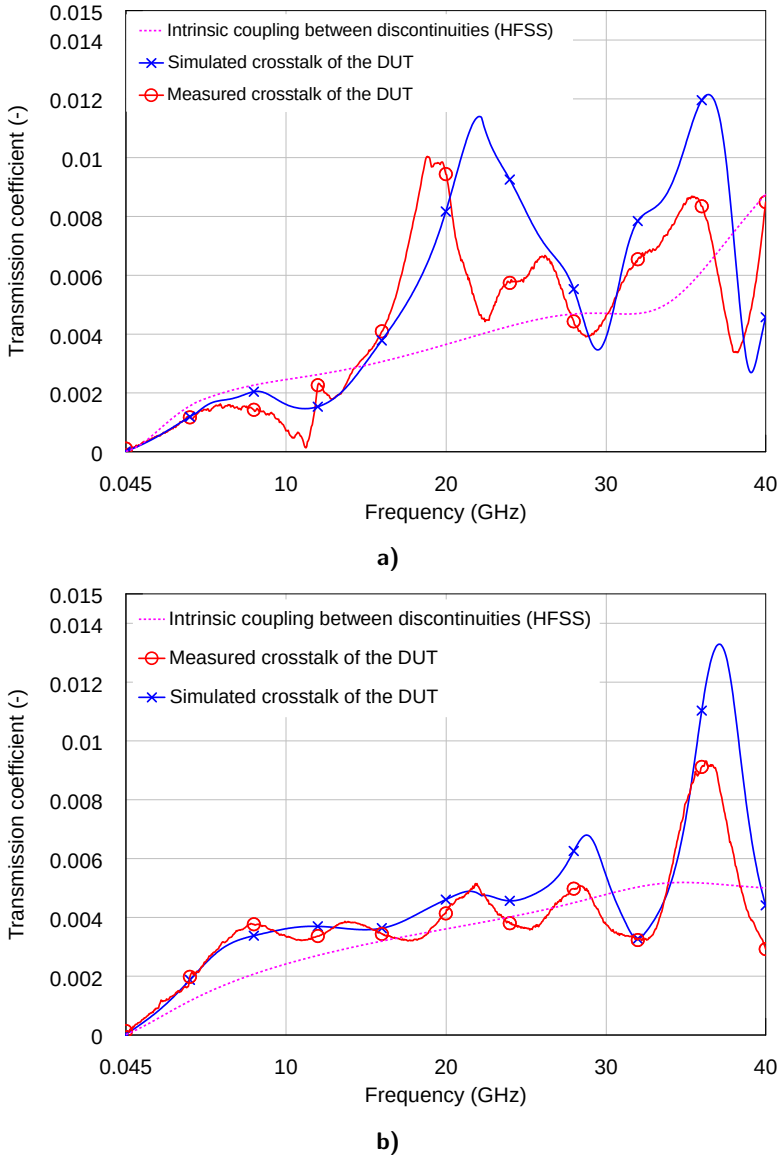


**Fig. 33** Comparison between the simulated and measured results of the DUT with a planar *open* (a) and *short* (b) calibration standards separated with a defined gap. Dotted line represents coupling between two *open* (*short*) discontinuities. All simulations are done with HFSS.

Two raw measurements (at the coaxial reference plane, thus including both end-launches) were done to see results for both common types of reflection standards (*short* and *open*) designed on a grounded coplanar waveguide (CPWG). See Fig. 31 for a picture of the DUT with an *open* reflection standard test board and Southwest end-launches. Both raw transmission measurement at the coax. reference plane in Fig. 33 are compared with simulated data from equivalent 3D EM models in HFSS.

The simulated traces agree with the measured data in both cases and positions of the peaks and troughs are in good correlation as well. Both discontinuities produce different results and it is not possible to account for this effect with some reasonable explanation. It is possible to reason that *open*-ended CPWG would have more significant effect on the overall crosstalk with its fringing field that should be larger than with the *short* discontinuity.

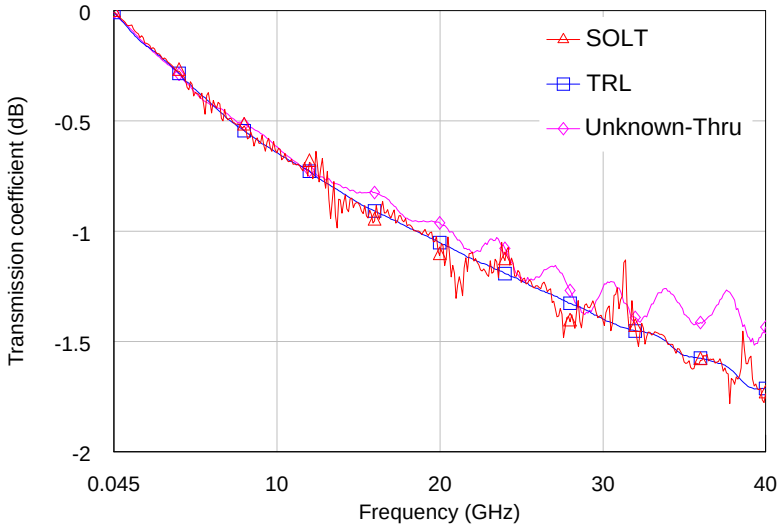


**Fig. 34** Comparison between the TRL and Unknown-Thru. Verification is done using CPWG transmission line with length 50 mm, i.e. 25 mm longer than the thru calibration element.

### 4.3.2 Unknown-Thru and TRL correction

It is now possible to correct for the systematic error introduced by the launchers and losses in the transmission lines. Hence another calibration/correction procedure is introduced in the following step that would have different reference planes from the first coaxial calibration. VNA Tools II from Metas [13] was used for this purpose as a data-acquisition and post-processing software.

Grounded coplanar waveguide transmission line with appropriate custom-built 2-port calibration kit (partially introduced in previous chapter in Fig. 19) is available and introduces the ability to perform multiple calibration schemes. Comparison of the data between Unknown-Thru [5], SOLT [3] and TRL [6] algorithms that are available within VNA Tools II is shown in Fig. 34. This qualitative verification is done using CPWG transmission line from the calibration kit that is 50 mm long. Discrepancies in this case show that TRL calibration for this scenario yields very smooth trace unlike the Unknown-Thru or the classical SOLT.

Corrected data for the crosstalk measurement are shown in Fig. 35. The correction for the same DUT is done with both TRL and Unknown-Thru. The influence of the method on the measurement results and discrepancies seems to be insignificant in this case and their influence will be neglected for the next results.

Comparison between three test boards with different lengths (25, 26 and 27 mm) while the gap between the *short* discontinuities is the same in each DUT is shown in Fig. 36. Notice that measured crosstalk varies with the distance of discontinuity from the launcher and peaks change their magnitude as well. Similar behavior was already observed in previous chapter in Fig. 26. The magnitude of crosstalk between both ports that is caused by radiation is increasing with frequency and position of the peaks varies with length of the DUT. In the frequency range up to 20 GHz, there is no significant ripple or any evidence for the radiation at all hence all traces overlap (that is to be expected if the gap is kept constant). The overlap shows that the assembly repeatability and noise levels are the residual random errors in this data.

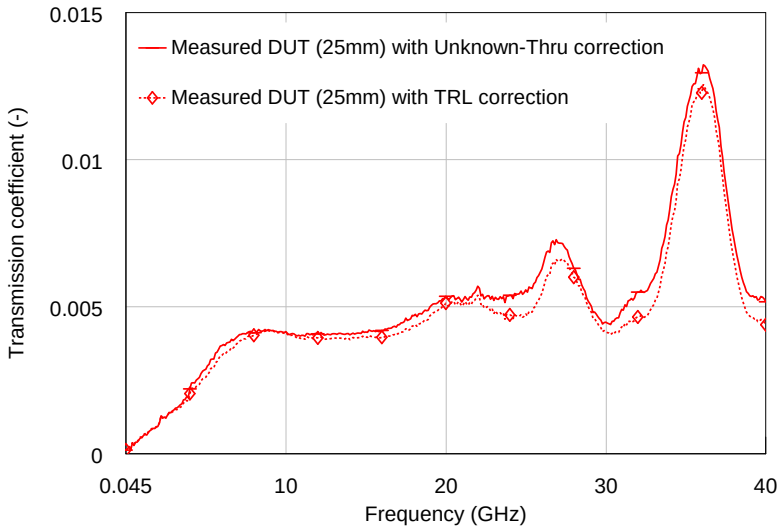


**Fig. 35** Comparison between the Unknown-Thru and TRL calibration/correction algorithms. DUT is 25 mm long test board with *short* discontinuities with a gap.

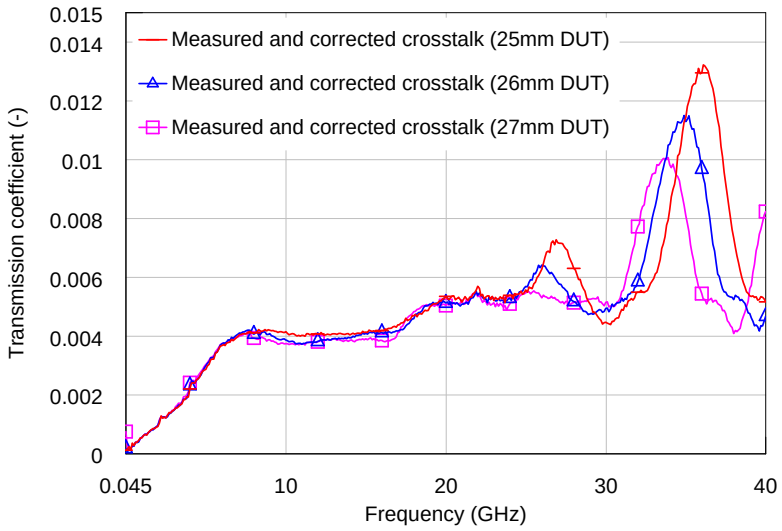


**Fig. 36** Comparison between the test boards with *short* discontinuities and various length 25, 26 and 27 mm. Unknown-Thru calibration/correction algorithm was used for correction.

## 4.4 Discussion

The experimental results in this chapter were first compared to the simulated data in Fig. 33. Achieved discrepancy is satisfactory with respect to the measured and simulated quantities in the order of thousandths in linear scale. There are measurement errors that have to be addressed and explained.

First contribution is caused by the reflection of the 2.92 mm coaxial connector mounted on the launcher which was not included in these simulations – only the launcher itself (see Fig. 31). Deeper analysis is necessary especially for the frequency range 18 - 25 GHz in the measurement with the *open* test board (see Fig. 33). This discrepancy has yet to be confirmed by another experiment.

The measured and simulated values for DUTs with *short* and *open* differ significantly. This should prove the concept that radiation properties of any given transition depend

on the load impedance and its reflection coefficient. The transmission coefficient is proportional to the phase of reflected wave from the discontinuity, that was observed in measurement with DUTs of different lengths (Fig. 36) while on lower frequencies, the traces practically overlap (the radiation effects are nonexistent).

In contrast, the simulated coupling between individual discontinuities is comparable for both *open* and *short* test boards (Fig. 32), but this cannot be supported by a direct measurement that would eliminate all systematic errors to enable acquiring the data with required accuracy. The measured $S_{21}$ can be further normalized to the magnitude of simulated coupling which would give the magnitude of the actual crosstalk component. The measurements were subjected to calibration and correction with different algorithms to eliminate the present systematic errors, but the corrected and uncorrected results do match quite well.

The experimental approach proved several speculations and showed that radiation issues can be detected even with commercially available precision launchers are used. The data show that the Southwest launchers used for the experiment perform well in terms of radiation properties up to approx. 30 GHz with this specific substrate and transmission line. The detailed experiments enabled to gather some data to introduce some theoretical models for the coaxial-to-planar transition including the radiation.

## 4.5 Modeling the transition with radiation effects

With some experimental data already collected, one of the main interest would be the development of a mathematical description that would account for the additional radiation losses in the transition/launcher. The effort can be concentrated into developing a suitable analytical model that would describe the radiation behavior of the transition well enough from the point of dependency on the character of the load impedance. Such model has to be usable in a calibration and correction scenario. The main difficulty lies in the nature of the radiation properties that are not completely intuitive. From previous chapters it has been established that

- there is a correlation between simple open-ended coaxial line and coaxial-to-microstrip transition in terms of radiation efficiency and magnitude of radiated power
- radiated power is quasi-exponentially increasing in the frequency band of the interest
- value of reflection coefficient (i.e. value of the load impedance) influences the resulting radiated power and its frequency dependence
- apart from added losses caused by radiation, there is also the apparent effect of interference between the radiated wave and the QTEM microstrip mode or the microstrip discontinuity

The acquired knowledge about the transition behavior should help to derive its mathematical model. It has been presented that radiation is dependent (apart from intrinsic geometrical properties of the transition) on several variables. One can write that the radiated power is generally a function of

$$P_{\mathrm{rad}} = f\left(\Gamma_{\mathrm{L}}, f, \beta_{\mathrm{lin}}, \alpha_{\mathrm{lin}}\right) \tag{50}$$

where phase constant $\beta_{\mathrm{lin}}$ and attenuation constant $\alpha_{\mathrm{lin}}$ add up to the propagation constant on the transmission line that is used, $\Gamma_{\mathrm{L}}$ is a reflection coefficient of the load impedance and $f$ the frequency.

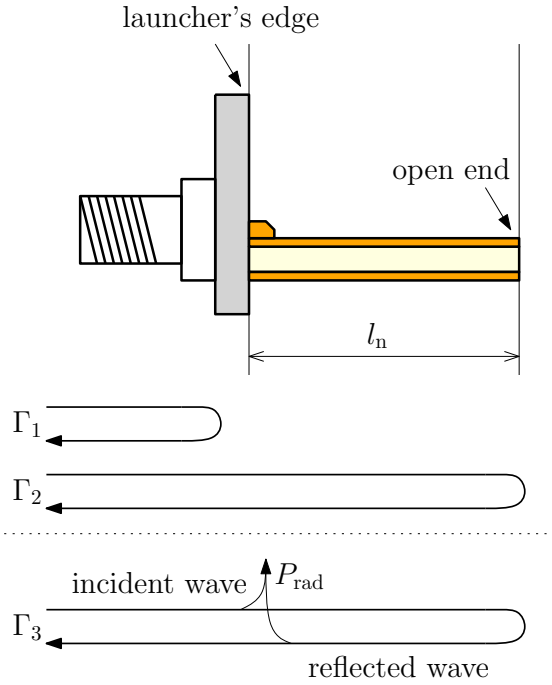


**Fig. 37** Schematic of the incident and reflected waves when calculating the radiated power.

The presence of $\Gamma_L$ in the function means that the transition's radiation changes with the load impedance. For example, during the calibration on microstrip, the $\Gamma_L$ might be known in advance. But if one wants to measure an unknown DUT, the added losses caused by $P_{rad}$ cannot be determined beforehand.

### 4.5.1 The superposition model

One can look at the radiation problem as being a superposition of two waves. If there are considered only waves traveling in the forward direction of the transition ($\Gamma_2 = 0$ in Fig. 37) the radiation from the transition introduces some added losses to the transition. This effect could be easily corrected with a calibration algorithm.

The case of almost perfectly matched microstrip line can be investigated using 3D EM field simulation tools. Similar model was already introduced in Fig. 17 along with simulation results. Radiated power was calculated and plotted for a simple model of coaxial-to-microstrip transition. This enables to compare the transition model to an open-ended coaxial line with a ground plane. It was discovered that there are certain similarities in terms of radiation properties (power, far-field diagram).

Both cases considered only one wave (it can be called incident) propagating through the transition and its launcher. This is unfortunately not the case with the real world scenario of transition with microstrip line with arbitrary impedance at its end that causes an appropriate reflection coefficient.

For the sake of simplicity, let's assume open-ended microstrip line with length $l_n$ mounted to a transition (Fig. 37). The incident wave enters the radiating part of the model (i.e. the launcher's edge) and part of the power would be radiated – hence additional losses are introduced. Part of the wave continues to the open-end and reflects with some magnitude and phase (small fraction will be radiated through the fringing field of the discontinuity). This wave (which can be called reflected) travels in the reverse direction and at the launcher's edge, part of the power would be radiated similarly

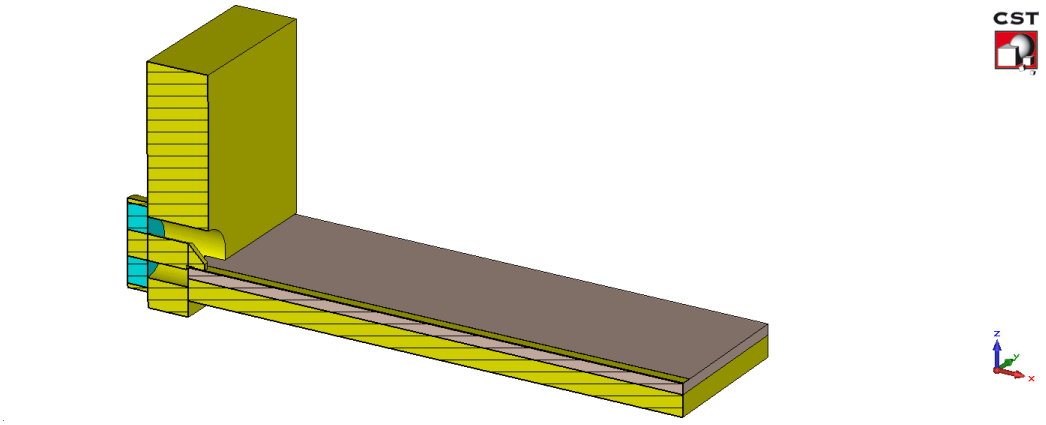


**Fig. 38** CST Microwave Studio model with open-ended microstrip line that was used to verify the radiation hypothesis.

as what happened to the incident wave.

This superposition of two waves with different phases and almost the same magnitude would produce interference pattern with maxima and minima (in case of addition in-phase or out-of-phase). This can be observed as distinctly frequency-dependent radiated power from such model. This superposition idea has to be confirmed by simulations as well.

### 4.5.2 Simulations

Simulations in CST Microwave Studio were performed that could verify the validity of concept described in previous section. The perspective view of the model is shown in Fig. 38 and physical dimensions are in close relation to the original Omni-Spectra SMA end-launch [52] which is being used for experimental purposes and other measurements.

The lossy copper microstrip line used in the model is calculated to have 50 Ω impedance at center frequency 10 GHz on Rogers Corp. 4350b [47] substrate 0.508 mm thick.

First simulation scenario was done which consisted of six-step parametric sweep of the microstrip line length varying from 15 to 25 mm. S-parameter $S_{11}$ results are plotted in Fig. 39 for each length step $n$. Each trace varies with frequency in predictable way and distinct ripple can be seen that results from vector addition of reflection coefficients $\Gamma_1 + \Gamma_2$ (introduced in Fig. 37).

Additionally, as the frequency passes above roughly 18 GHz, another phenomenon is becoming noticeable. The difference between peaks and valleys is increasing (i.e. frequency dependence of $\Gamma_1$ with frequency is increasing) and additional losses appear in the trace as well (can be noticed as the quasi-exponential trend of the plotted $S_{11}$ versus frequency does not agree with expectations for the losses on such open-ended microstrip line without the launcher). The latter effect cannot be explained by simple complex addition/subtraction of $\Gamma_1$ and $\Gamma_2$ on traditional transition with microstrip line. In depth analysis was performed which included also an electric and magnetic field calculation with additional far-field analysis.

To illustrate the difference between peak and valley in terms of magnitude of electric field, cross section of the CST model with the electric field contours is shown in Fig. 40. The difference in wavelengths and electric lengths of the microstrip line contributes to the fact that the traveling waves can constructively or destructively interfere at the launcher's position. This is having significant influence on the radiation properties of

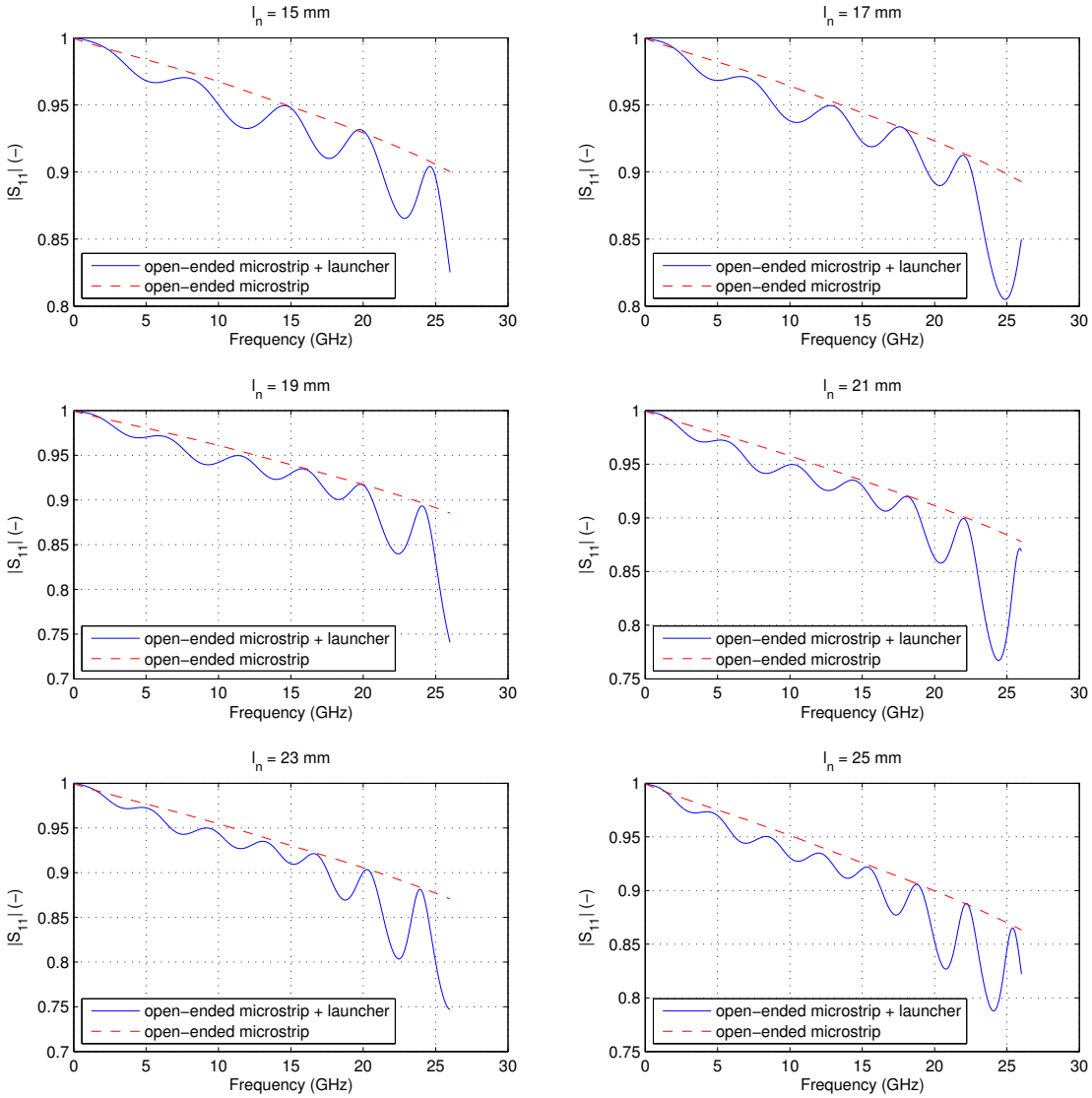


**Fig. 39** Results from CST Microwave Studio of the microstrip line with swept length between transition and the microstrip open (solid line). Idealized situation with open-ended microstrip line without the launcher (dashed line).

the structure. At the peak of the reflection coefficient, both waves destructively interfere producing a negligible radiated power at this wavelength. On the contrary, both waves constructively interfere when there is a valley in the reflection coefficient which means increase in radiated power that can be measured as an added loss on this wavelength.

If one plots calculated Total Radiated Power (TRP) which is absorbed by the boundary the results can help to explain this effect.

The traces labeled as **CST simulation** in Fig. 41 plot TRP as a function of frequency for each step in the varying microstrip line length $l_n$. Positions of $k$-th radiation peak can be empirically evaluated from the simulations. This way, one can calculate a local maximum of radiated power for a given configuration. It can be expressed as [39]:

$$f_{\text{peak}} = k\frac{c}{2l_n\sqrt{\varepsilon_{\text{eff}}}} \tag{51}$$

where $c$ is a speed of light, $\varepsilon_{\text{eff}}$ is an effective permittivity and $l_n$ is a length of the

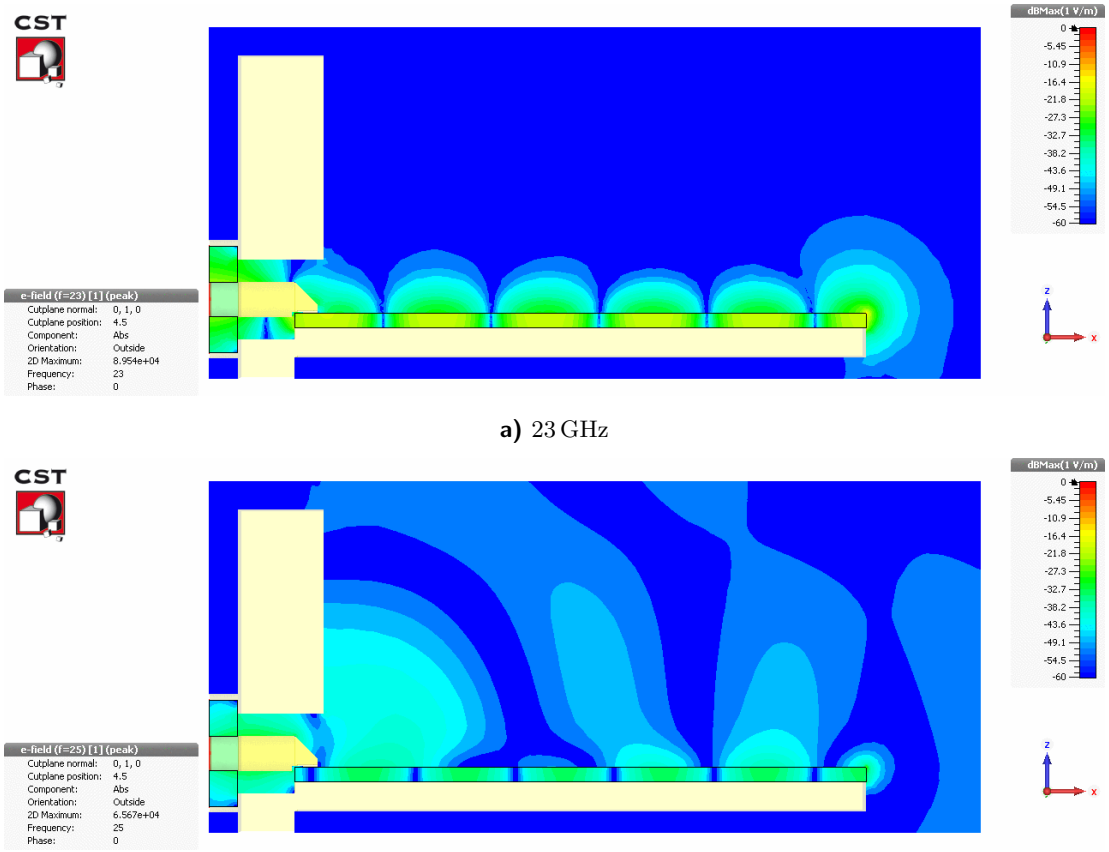


**Fig. 40** Calculated electric field in logarithmic scale normalized to maximum value. CST simulations were performed for $l_n = 20\,\text{mm}$ using FEM frequency solver. Note that this illustrates the case of minimum (a) and maximum (b) of radiated power on a deliberately chosen frequency point.

microstrip line. This equation serves as the first approximation and does not help to explain the observed influence. To verify the hypothesis, the mathematical model that enables to calculate the value of TRP for any given microstrip length will be presented (see traces labeled as **Model** in Fig. 41).

$$C_1 = 1 \tag{52}$$
$$C_2 = e^{-2\alpha l'_n} e^{-2i\beta l'_n} \Gamma_\text{L} \tag{53}$$
$$C_3 = A\,(C_1 + C_2) \tag{54}$$

Equations 52-54 show a simple addition of two electromagnetic waves $C_1$, $C_2$ that propagate and interfere at the edge of transition multiplied by a constant $A$ that represents intrinsic frequency-dependent radiation properties of a transition which is not under superposition of two waves.

The propagation constant variables $\alpha$, $\beta$ can be determined using a CST Microwave Studio as well as reflection coefficient $\Gamma_\text{L}$ that is simulated as an open-ended microstrip in this case. The effective length of the microstrip line $l'_n$ and the radiation constant $A$ are unknowns that can be calculated. The length of the microstrip line $l_n$ has to be corrected with term $l_\text{diff}$ to take into account not very well defined type of transmission line (from the electro-magnetic field distribution point of view) at the transition edge

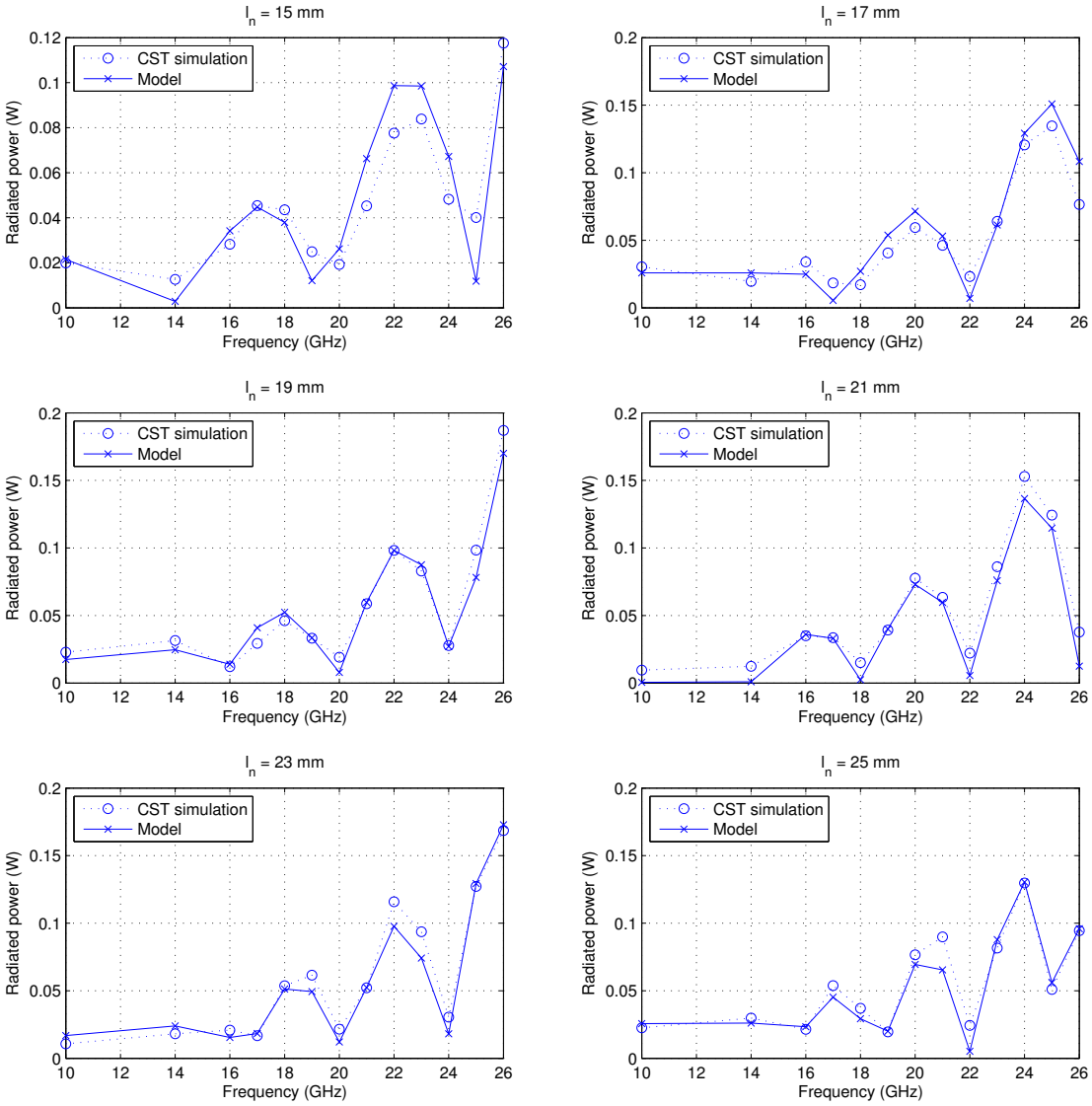


**Fig. 41** Comparison between CST Microwave Studio and MATLAB model of the calculated TRP from the 3D model of the microstrip line with the transition. The comparison is done for a varying length of the microstrip line between transition and the reflective load impedance (microstrip open).

between the coaxial line and the microstrip. This constant is applied to each length as $l'_n = l_n + l_{\text{diff}}$.

One can have multiple radiated power *measurements* (obtained from CST Microwave Studio) for different lengths of the microstrip line $l_n$ to have enough linearly independent equations to calculate the unknowns. In this case, simulation sweep was performed for lengths varying from 15 to 25 mm (similarly as in Fig. 39).

With these data, one can perform least-squares data-fitting to solve for frequency dependent vector $A$ and for the scalar $l_{\text{diff}}$ using the function `lsqnonlin()` in Matlab. The calculated value of the frequency dependent vector $A$ that determines the radiation of a single propagating wave is plotted against simulated results in Fig. 42. The fitted unknown scalar value $l_{\text{diff}}$ is equal to $+0.675$ mm.

There is some periodic discrepancy between both traces which is caused by non-zero reflection coefficient remaining in the CST model (i.e. $\Gamma_2 \neq 0$) caused by the simulator

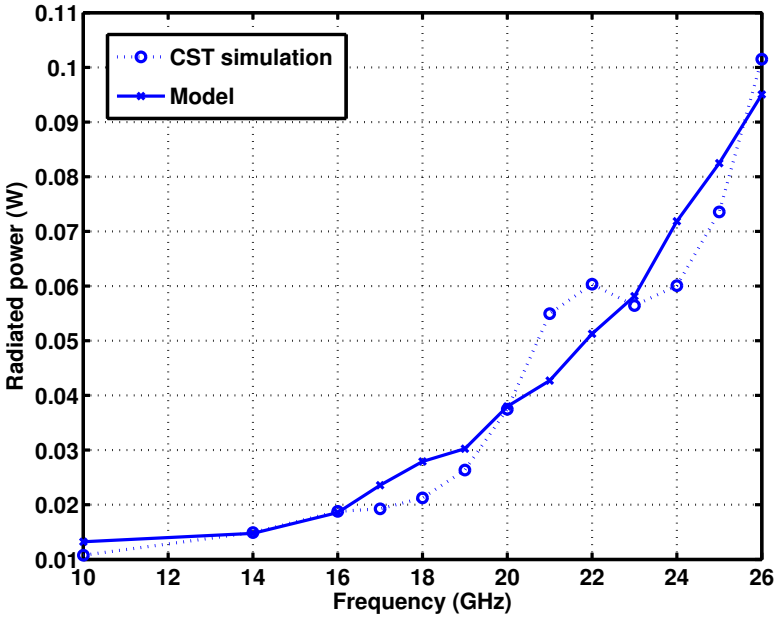


**Fig. 42** Radiated power from the transition that is not being subjected to superposition of two waves. Fitted value of $A$ is compared to a CST simulation of almost ideal reflection-less case of a wave propagating through coaxial-to-microstrip transition.

setting that unfortunately introduces similar effect as observed in Fig. 41. It needs to be emphasized that the evaluated values $A$ and $l_{\text{diff}}$ represent the radiation of a transition for the scenario of a single propagating wave without any superposition from the discontinuities. The results show that interference of two electromagnetic waves can describe physical behavior of the launcher quite well for the presented superposition case.

Traces labeled as **Model** in Fig. 41 show TRP for each $l_n$ obtained using extracted variables $A$, $l_{\text{diff}}$ and computed $\alpha$, $\beta$ and $\Gamma_{\text{L}}$. This validates the simplified explanation proposed in this section. However, more in-depth analysis would be needed to introduce the radiation effect into the practical examples with planar calibration and correction.

The error model parameters that are evaluated during any calibration with this transition model cannot have a direct interference with the unknown value $\Gamma_{\text{L}}$ which is actually being calculated during the following correction. The error term $e_{10}$ would then vary with different magnitude or phase of $\Gamma_{\text{L}}$ as the radiated waves are propagating along the transmission line and interfere with the field from the QTEM mode and other discontinuities thus changing their properties with the magnitude of the radiated power.

# 5 Coaxial-to-planar transitions with suppressed radiation

The purpose of this chapter is to cover achievements published in one paper [48] that contains the essential part of this thesis. The referenced paper presents not just a physical explanation of the radiation from the transition, it shows one possible design of a coaxial-to-microstrip transition that sufficiently suppresses the unwanted radiated wave without introducing any disadvantages in usability. Experimental and simulation results that validate the effectiveness of the proposed structure are presented, and it is shown that the published hardware solution improves the measurement accuracy when using the common calibration method (1-port and 2-port Short-Open-Load-Thru (SOLT) [3]).

Unlike the approach in [43, 44], versatile configuration of the test-fixture without any practical limitations is described in the following sections. It is worth to note that the presented radiation problem should not be confused with the leaky-wave modes on microstrip, which are not present due to dimensions of the microstrip (i.e. substrate thickness) used throughout this chapter.

## 5.1 Test-fixture

The custom-made test-fixture used throughout this chapter is based on a standard coaxial launcher mounted onto the metallic base and is designed to enable quick assembly of planar DUTs to speed-up the measurements with good reproducibility. The test-fixture used for the purpose of this chapter was fabricated using two Omni-Spectra SMA launchers [52] (see photos in Fig. 43) and has a fixed length of 50 mm.

Laminate substrate Rogers 4350b [47] $h = 0.508\,\text{mm}$ (20 mils) thick was used during subsequent simulations and measurements. For simulation purposes, the substrate was defined as a lossy dielectric with $\varepsilon_\text{r} = 3.66$ and $\tan\delta = 0.004$.

The proposed approach is based on mechanical modifications in the transition's edge (see Fig. 43) to suppress the radiated field near the launcher using two short sidewalls on each side of the microstrip line. The concept is illustrated on the diagram in Fig. 44 and it is inspired by commercially available endlaunch solution by Southwest Microwave [49] that is suitable mainly for CPWG transmission line. All essential dimensions are introduced in Fig. 44 and will be used throughout this section. The standard and the proposed test-fixture use the same SMA launchers and they differ in the mechanical design of the transition edge.

Different hardware approach was adopted in other papers [43], [44] however they introduced some practical limitations with the modification as well, especially in [44]. The concept from [44] can be thought of as a parallel-plate transmission line that is created by the conducting sidewalls. All excitable modes that are below the cutoff frequency of the parallel-plate will result in an evanescent mode, which means that they cannot propagate or radiate due to the very high attenuation inside an ideal parallel-plate which would be infinitely large. Naturally, for clearly practical reasons, one has to introduce parallel-plate with reasonable dimensions, which will allow some

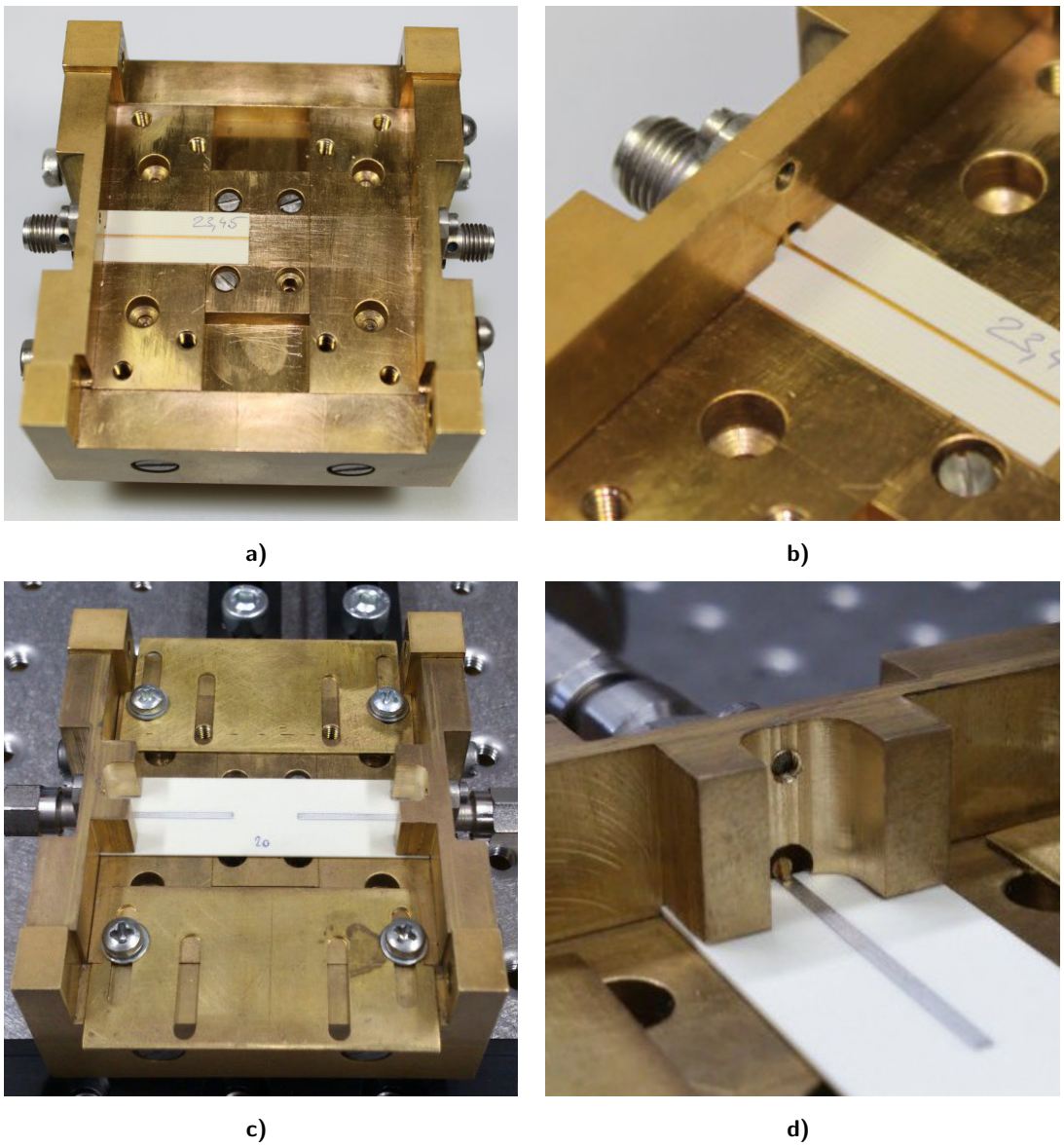


**Fig. 43** Top view (a) and perspective (b) of the standard test-fixture; top view (c) and perspective (d) of the proposed test-fixture with microstrip calibration standard as a DUT. Both test-fixtures use the same SMA launchers and they differ in the mechanical configuration of the transition's edge.

residual radiation as a drawback. The presented solution is a trade-off between sufficient suppression and reasonable dimensions.

## 5.2 CST MWS approach

The suppression of the radiated field can be illustrated using CST simulations in Fig. 46. Both models are drawn accurately to their physical representations of fabricated test-fixtures (see photographs in Fig. 43b for the unmodified test-fixture and in Fig. 43d for the proposed test-fixtures) with coaxial launchers. The models of the transitions consist of the coaxial launcher and open-ended microstrip line. This allows to observe, explain and qualitatively evaluate the interactions between standing wave caused by the open

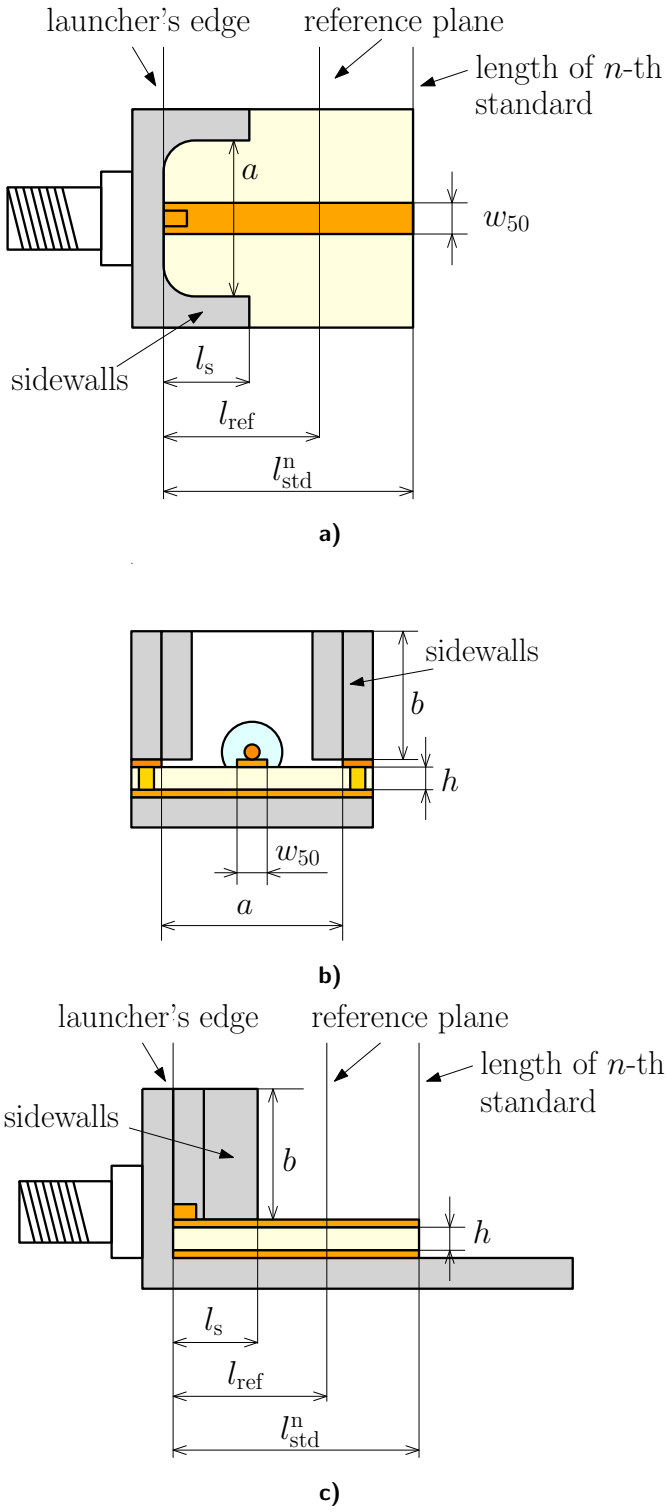


**Fig. 44** Plan view (a), cross section (b) and longitudinal view (c) of the proposed test-fixture with microstrip calibration standard as a DUT.

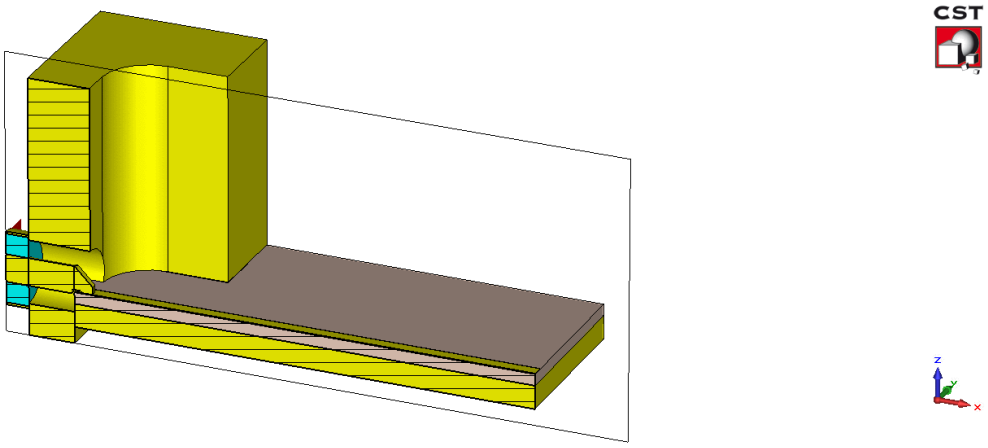


**Fig. 45** CST Microwave Studio model with open-ended microstrip line with proposed modification of the endlaunch construction.

end and the radiated wave from the transition. No objective qualitative conclusion should be made from these informative results.

The unmodified transition excites an electromagnetic wave that will propagate into the free space above the microstrip. Despite the fact that the main radiation lobe is rather focused under elevation of $\theta \approx 30°$, this wave propagates along the microstrip and interferes with the desired QTEM mode as a result. This behavior is consistent with results in [30] and radiation pattern of this model is very similar to the simulation in Fig. 17. The proposed solution (see Fig. 46b and Fig. 45) effectively suppresses this excitation and the interactions with QTEM on microstrip are minimized as well as the added losses introduced by the radiation.

This solution is effective only below the cutoff frequency of the sidewalls configuration that act as a parallel-plate transmission line. With increasing frequency of traveling wave, the suppression is becoming less effective after the cutoff. From the approximate cutoff frequency for a parallel-plate (given by [46]) one can estimate the maximum effective frequency for the suppression.

$$f_{\text{cutoff}} = \frac{c}{2a\sqrt{\varepsilon_{\text{r}}}} \tag{55}$$

Where $c$ is speed of light in vacuum, $a$ is distance between the „plates“ (see Fig. 44a) and $\varepsilon_{\text{r}}$ is relative permittivity of the dielectric which fills the parallel-plate. For example if $a = 6.5\,\text{mm}$ is chosen, this gives approximate cutoff frequency $f_{\text{cutoff}} \approx 23.07\,\text{GHz}$ of the dominant parallel-plate mode, assuming vacuum as a dielectric material.

It is now clear that dimensions of the structure (not just the distance $a$) would have to be chosen to achieve satisfying performance.

### 5.2.1 Parametric analysis

Parametric sweep for the most important dimensions of the parallel-plate is shown in Fig. 47. The reflection coefficient of the proposed transition with open-ended microstrip line is noticeably varying with distance between sidewalls $a$ while the length of the sidewalls $l_{\text{s}}$ has smaller influence in the presented swept range. As the distance $a$ is decreasing, the cutoff frequency of the parallel-plate is increasing which results in effective radiation suppression on frequencies below the cutoff. This effect has to be

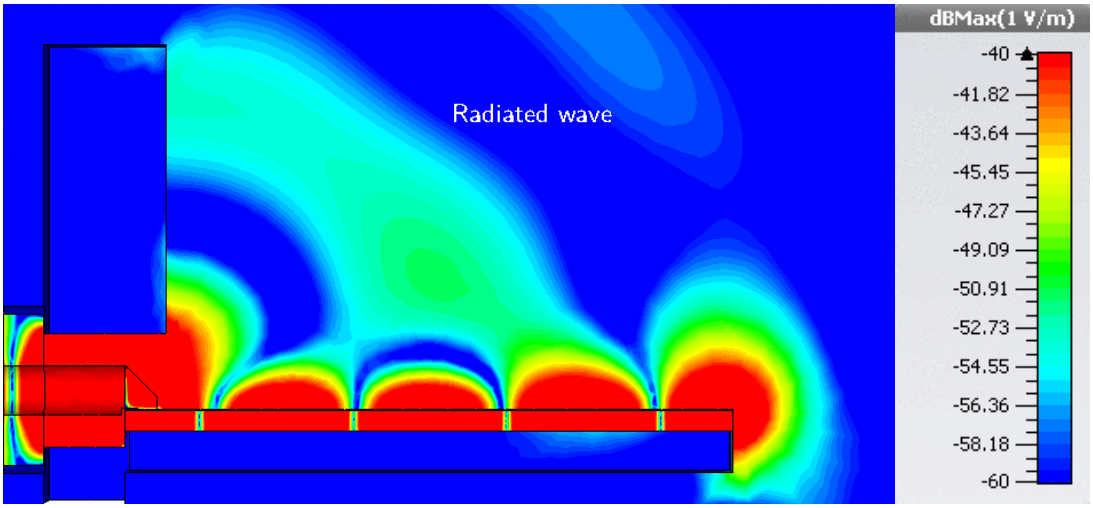


a)

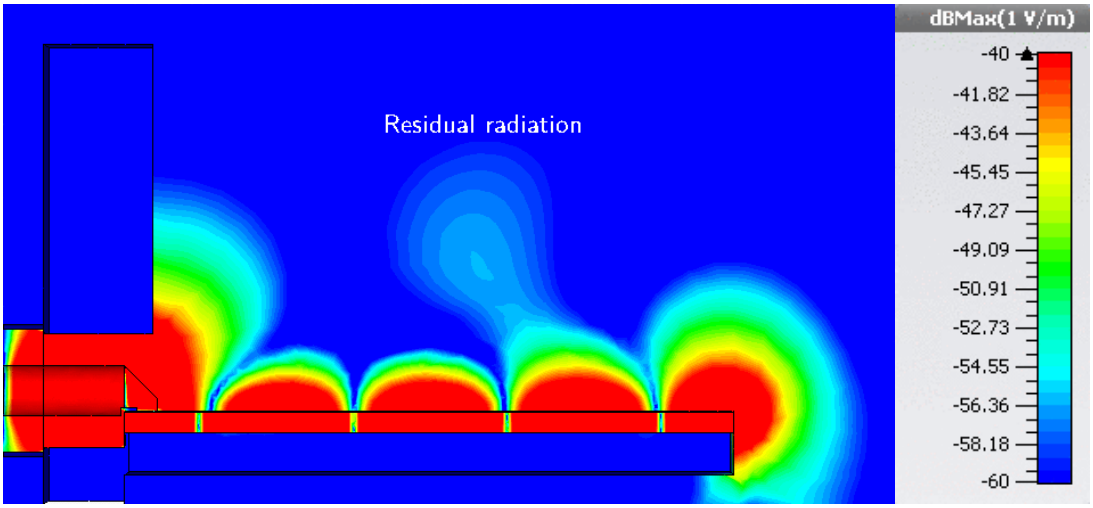


b)

**Fig. 46** Effectiveness of the proposed solution. The electric field distribution in the unmodified test-fixture (a) shows a traveling wave which is interfering with the standing wave on the microstrip line. The modified test-fixture (b) clearly suppresses the free-space propagation. Both figures are in scale (note that the logarithmic scale is adjusted for better perception of the radiated field). Frequency was chosen to show the suppression in case of the largest radiated power.

supported by appropriate height of the sidewalls $b$. While the height increases, the parallel-plate is becoming more efficient in the whole frequency range below cutoff. Surprisingly enough, the configuration becomes effective even when $b$ is larger than 1.5 mm as it is shown in Fig. 47c.

Traces of $S_{11}$ might not be reliable enough to verify the actual magnitude of the radiated electromagnetic field from the launcher. Fig. 48 shows radiated field in terms of calculated radiated power (TRP) from the transition model for the swept geometrical dimensions $a$ and $b$. For this set of simulations, the influence of the open-end was excluded from the simulation in order to compare the configurations without any reflections or standing waves. This was achieved by using two-port model with matched second waveguide port.

Notice the different effect of both variables on the radiated power. Instead of al-

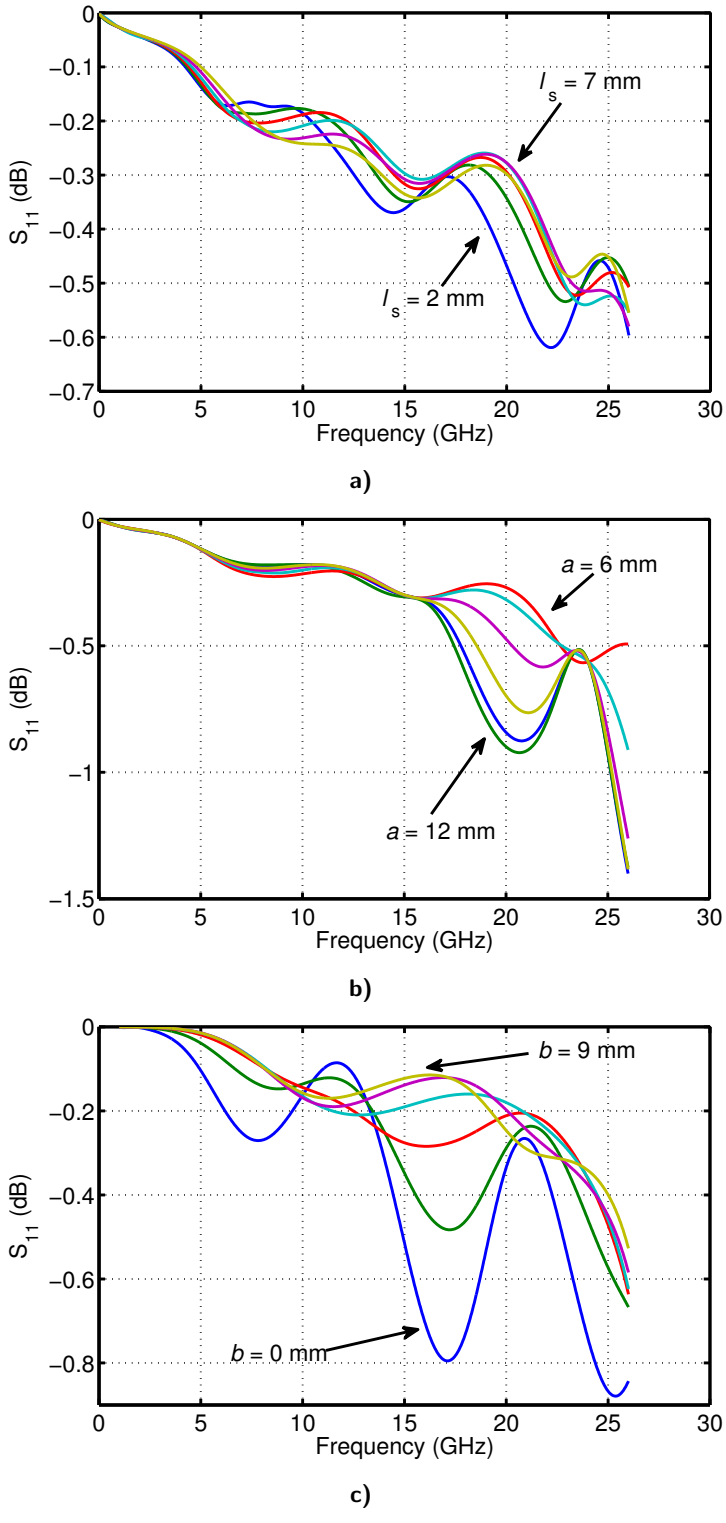


**Fig. 47** Reflection coefficient of the proposed transition with open-ended microstrip line. (a) Variation of the sidewalls length $l_s$ is between 2 and 7 mm ($a = 6.5$, $b = 9$). (b) Variation of the distance $a$ is between 6 and 12 mm ($l_s = 4.6$, $b = 9$). (c) Variation of the height $b$ is between 0 and 9 mm ($l_s = 4.6$, $a = 6.5$).

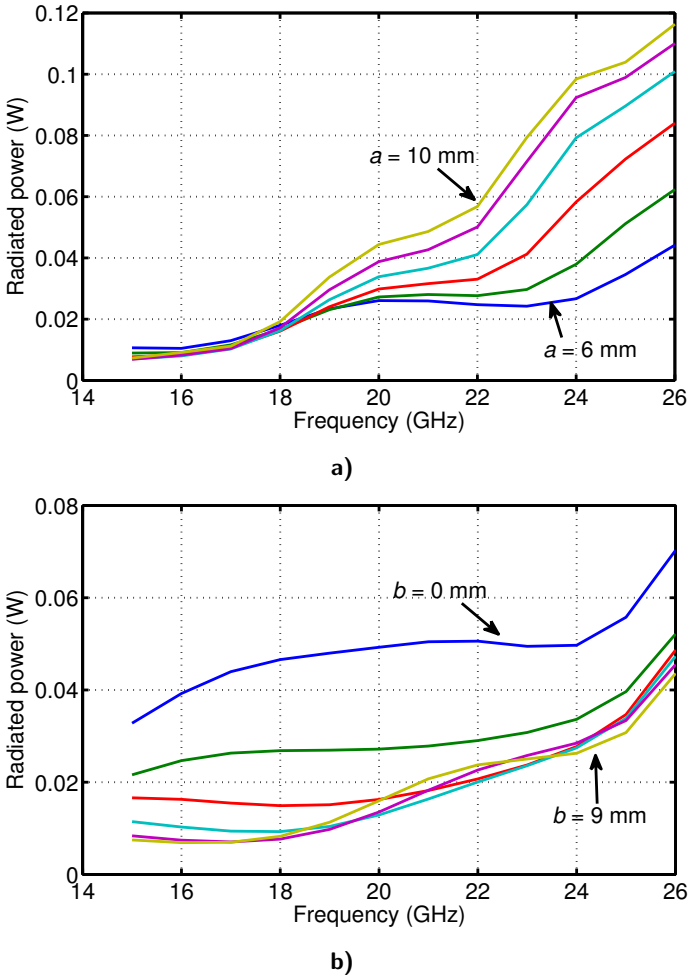


**Fig. 48** Radiated power from the transition model for incident power equal to 1 W. (a) Variation of the distance $a$ is between 6 and 10 mm with step 0.8 mm. (b) Variation of the height $b$ is between 0 and 9 mm with step 1.5 mm. Note that influence of the microstrip open-end is excluded in both figures by using two-port model with matched waveguide port.

most linear dependence of radiated power on distance $a$ (see Fig. 48a), the radiation is rather exponentially dependent on the height $b$ (see Fig. 48b) indicating that there is a very sharp cut-off for the suppression to become effective, as proved earlier with the simulation of $S_{11}$.

Simulation results show achievable suppression of the radiated power and its dependence on the width and the height of the parallel-plate. Presented parametric sweeps can provide ideal dimensions for the best achievable suppression for one specific substrate properties. The final design of the test-fixture was fabricated with the following dimensions: $a = 6.5$ mm, $l_s = 5.3$ mm and $b = 9$ mm.

## 5.3 Calibration and correction

The proposed test-fixture should serve as a reliable platform for accurate and repeatable measurements of surface mount devices (SMD). To validate the effect of the proposed modifications, calibration and correction is performed to move the calibration reference plane onto the planar transmission line and to include the launcher into the error model, which compensates for the added losses of the interconnecting lines and unwanted re-

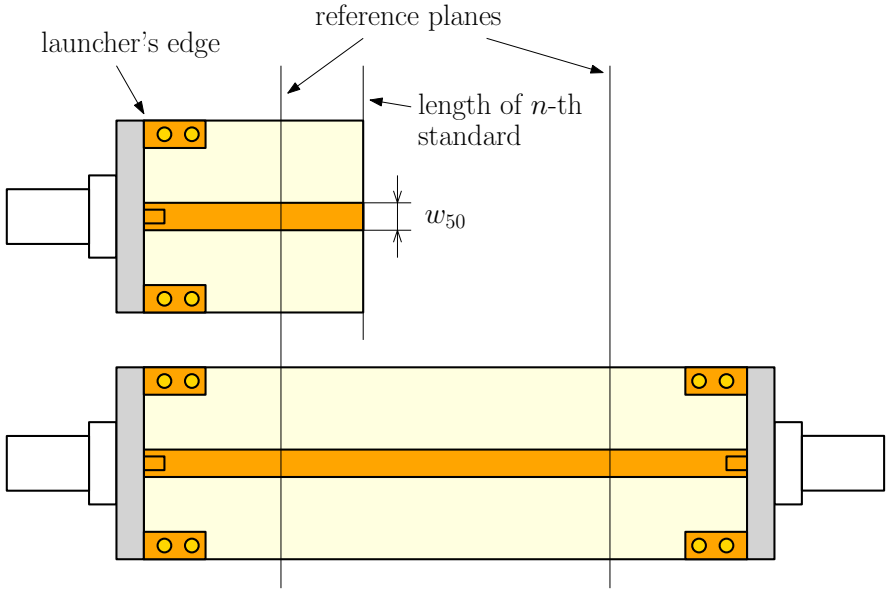


**Fig. 49** Detail of the *open* and *thru* calibration standards to illustrate the modification for the proposed test-fixture. Number of the vias and their placement is just for illustration purposes.

flections from the transition. There are many suitable calibration methods, most of them [6] – [5] use some type of reflective calibration standard - short or open. Due to the fact that the test-fixture is not adjustable in length, the TRL method or other derivatives that require 2-port offset length standards are not suitable in this case.

Reflective standards in presented measurements are microstrip open-ends with offset length – this decision is made in favor of minimizing the fabrication repeatability error which may vary with different type of calibration standard. The custom-built calibration kit for this experiment contains six offset opens ($l_{\mathrm{std}}$ = 20, 21, 22, 23, 24 and 25 mm) and one microstrip thru standard ($l_{\mathrm{std}}$ = 50 mm long) on 50 Ω microstrip line. Simulation data from CST Microwave Studio were used to characterize both magnitude and phase of each calibration standard in the whole frequency range. Additionally, 3D models of the standards were adjusted after precise optical measurement with accuracy of $\pm 2\mu m$.

Calibration standards were designed to provide a better compatibility with the proposed test-fixture and to enable higher effectiveness. To avoid any unwanted resonant effects, the sidewalls are placed onto the substrate and through the vias connected with the microstrip ground. See Fig. 49 for the detail of the calibration standards.

### 5.3.1 One-port error model

An over-determined technique using 6 microstrip open calibration standards with different lengths was implemented (according to Least-Squares OSM approach [4]) in Matlab. This method is an improvement over the well known OSM (open-short-match) technique that derives the frequency dependent error model by solving the system of three equations with three unknowns (directivity $e_{00}$, reflection tracking $e_{10}e_{01}$ and source match $e_{11}$). For description of the error model see Fig. 50.

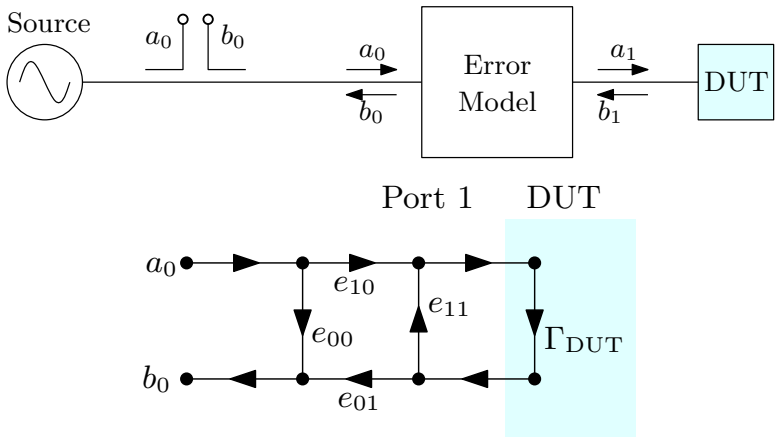


**Fig. 50** One-port error model from the point of view of perfect reflectometer and microwave source including the signal flow graph with error terms.

The matrix equations for the forward error terms can be written as follows:

$$\begin{bmatrix} 1 & \Gamma_{\mathrm{m}1}\Gamma_{\mathrm{a}1} & -\Gamma_{\mathrm{a}1} \\ 1 & \Gamma_{\mathrm{m}2}\Gamma_{\mathrm{a}2} & -\Gamma_{\mathrm{a}2} \\ 1 & \Gamma_{\mathrm{m}3}\Gamma_{\mathrm{a}3} & -\Gamma_{\mathrm{a}3} \end{bmatrix} \cdot \begin{bmatrix} e_{00} \\ e_{11} \\ \Delta_e \end{bmatrix} = \begin{bmatrix} \Gamma_{\mathrm{m}1} \\ \Gamma_{\mathrm{m}2} \\ \Gamma_{\mathrm{m}3} \end{bmatrix} \tag{56}$$

This matrix equation is often symbolically rewritten to:

$$\mathbf{A} \cdot \mathbf{x} = \mathbf{b} \tag{57}$$

which one has to solve for vector of unknowns $\mathbf{x}$ on each frequency. On the other hand, the overdetermined calibration can have $n$ standards (generally more than three) which will yield $n$ measured reflection coefficients $\Gamma_{\mathrm{m}n}$ along with their known values $\Gamma_{\mathrm{a}n}$. The matrix equation 56 has to be rewritten to:

$$\begin{bmatrix} 1 & \Gamma_{\mathrm{m}1}\Gamma_{\mathrm{a}1} & -\Gamma_{\mathrm{a}1} \\ 1 & \Gamma_{\mathrm{m}2}\Gamma_{\mathrm{a}2} & -\Gamma_{\mathrm{a}2} \\ 1 & \Gamma_{\mathrm{m}3}\Gamma_{\mathrm{a}3} & -\Gamma_{\mathrm{a}3} \\ \vdots & \vdots & \vdots \\ 1 & \Gamma_{\mathrm{m}n}\Gamma_{\mathrm{a}n} & -\Gamma_{\mathrm{a}n} \end{bmatrix} \cdot \begin{bmatrix} e_{00} \\ e_{11} \\ \Delta_e \end{bmatrix} = \begin{bmatrix} \Gamma_{\mathrm{m}1} \\ \Gamma_{\mathrm{m}2} \\ \Gamma_{\mathrm{m}3} \\ \vdots \\ \Gamma_{\mathrm{m}n} \end{bmatrix} \tag{58}$$

where $\Delta_e$ is equal to:

$$\Delta_e = e_{00}e_{11} - e_{10}e_{01} \tag{59}$$

This overdetermined system of equations has to be solved for $\mathbf{x}$. In this case, the procedure within Matlab was utilized for this purpose that can solve the overdetermined system of linear equations (with function `mldivide`). The over-determined technique also reduces the uncertainty in the lower part of the frequency band of interest while keeping the overall usable frequency band width fairly high. The standard OSM approach with only three offset opens would introduce significant bandwidth constraints.

The $n$-th DUT with raw measured reflection coefficient $\Gamma^n_{\mathrm{m_{DUT}}}$ can now be corrected to obtain the desired reflection coefficient $\Gamma^n_{\mathrm{DUT}}$ using previously calculated terms $e_{00}$,

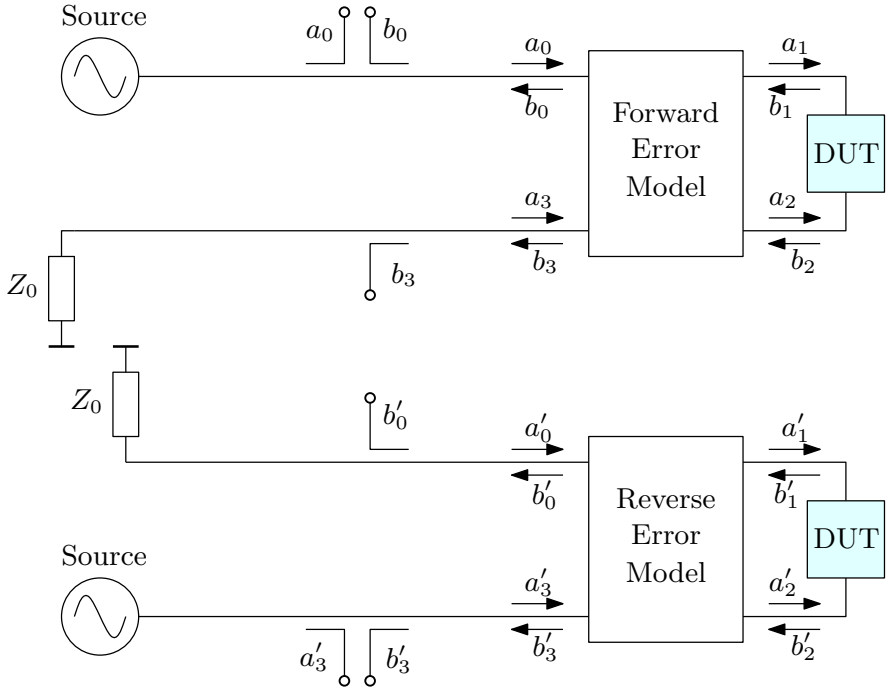


**Fig. 51** Forward and reverse error models for 12-term SOLT calibration method from the point of view of perfect reflectometer and microwave source.

$e_{11}$ and $e_{10}e_{01}$:

$$\Gamma^n_{\mathrm{DUT}} = \frac{\Gamma^n_{\mathrm{mDUT}} - e_{00}}{\left(\Gamma^n_{\mathrm{mDUT}} e_{11}\right) - (e_{00}e_{11} - e_{10}e_{01})} \tag{60}$$

By exploiting the overdetermined calibration, it is possible to perform plausibility check of the calibration [2] and use some of the standards directly as DUTs to check the calibration validity. Therefore the term DUT is used for all measured devices or calibration standards regardless of their actual purpose. Test scenario consists of the synthetic (or virtual) measurement followed by experimental verification on one-port and two-port DUTs.

### 5.3.2 Two-port error model

One of the most common calibration algorithms originally published by Rehnmark [53] was developed for a 12-term error model that divides the solution into forward and reverse models that are derived and applied independently. This measurement setup with both error models is shown in Fig. 51. This means, that unlike the Unknown-Thru [5] or TRL [6] that rely on 8-term error model, the number of unknowns is higher which means that one has to utilize more calibration standards.

Two-port 12-term SOLT [53] that uses the forward and reverse error models yielding 12 unknowns (depicted in Fig. 52) is described in this section. The two-port calibration process and error terms calculation can be divided into following steps:

1. Perform 1-port calibration using the one-port procedure from the previous section. Solve for $e_{00}$, $e_{11}$ and $e_{10}e_{01}$.
2. Terminate both ports with impedance $Z_0$ and measure the leakage $S_{21\mathrm{M}}$ that yields the isolation term $e_{30}$.

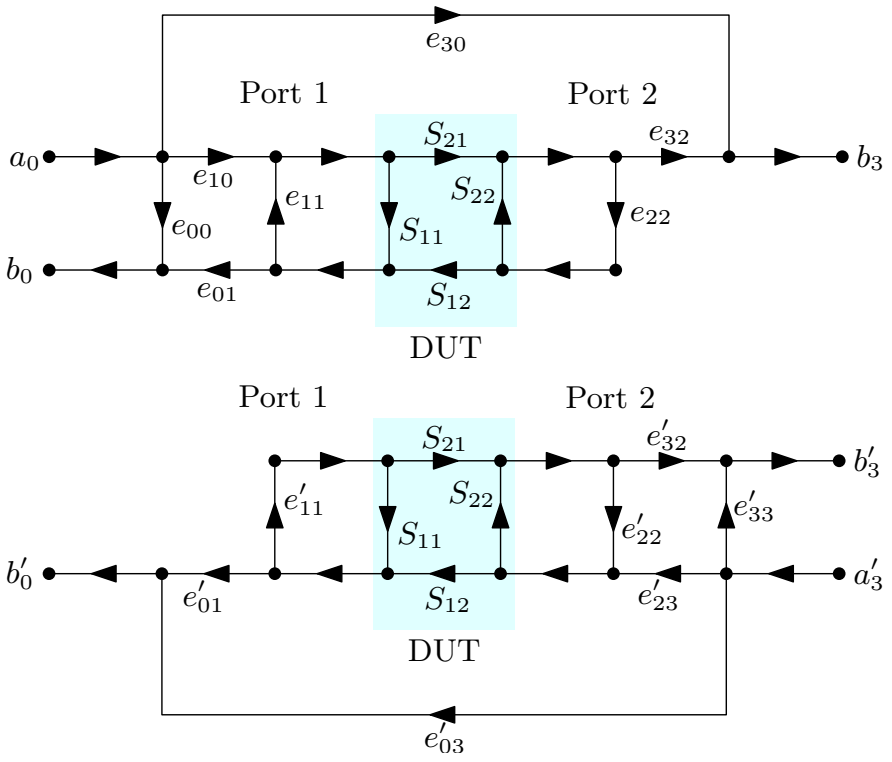


**Fig. 52** Signal flow graph of the forward and reverse error models for the 12-term SOLT calibration method.

3. Connect both ports with the *thru* calibration standard and measure the second port match $e_{22}$ using the calibrated one-port reflectometer at first port. Also measure the term $S_{21\mathrm{M}}$ that yields the transmission tracking $e_{10}e_{32}$.
4. Analogically use the same procedure for the reverse error model.

From the previous section that covered the one-port calibration, three error terms $e_{00}$, $e_{11}$ and $e_{10}e_{01}$ have been already established. The second step enables to measure the leakage between both ports if both of them have $Z_0$ terminations. This step is optional, and it is usually skipped with $e_{30}$ being set to 0. But all it takes is to perform a measurement of $S_{21\mathrm{M}}$, that is:

$$S_{21\mathrm{M}} = \frac{b_3}{a_0} = e_{30} \tag{61}$$

The third step requires to use a fully known *thru* calibration standard and to connect both ports together. This usually means that the *thru* has zero length and both connectors are placed together (provided that they mate). Then, measurements of $S_{21\mathrm{M}}$ and $S_{11\mathrm{M}}$ are done, that is:

$$S_{21\mathrm{M}} = \frac{b_3}{a_0} = e_{30} + (e_{10}e_{32})\frac{S_{21}}{1 - e_{11}S_{11} - e_{22}S_{22} + e_{11}e_{22}\Delta_{\mathrm{S}}} \tag{62}$$

$$S_{11\mathrm{M}} = \frac{b_0}{a_0} = e_{00} + (e_{10}e_{01})\frac{S_{11} - e_{22}\Delta_{\mathrm{S}}}{1 - e_{11}S_{11} - e_{22}S_{22} + e_{11}e_{22}\Delta_{\mathrm{S}}} \tag{63}$$

where $\Delta_{\mathrm{S}}$ is equal to:

$$\Delta_{\mathrm{S}} = S_{11}S_{22} - S_{21}S_{12} \tag{64}$$

Using these measurements, one can evaluate for the remaining terms:

$$e_{22} = \frac{S_{11\mathrm{M}} - e_{00}}{S_{11\mathrm{M}} e_{11} - \Delta_e} \tag{65}$$

$$e_{10} e_{32} = (S_{21\mathrm{M}} - e_{30})\,(1 - e_{11} e_{22}) \tag{66}$$

The term $e_{22}$ is measured directly due to the fact that the port 1 is already calibrated for one-port measurements and full knowledge (all four S-parameters) of the *thru* standard is provided. If the similar workflow is performed for the reverse error term, one can perform the correction to obtain the S-matrix $\mathbf{S}$ of the unknown DUT [54].

$$D = \left(1 + \left(\frac{S_{11\mathrm{M}} - e_{00}}{e_{10} e_{01}}\right) e_{11}\right)\left(1 + \left(\frac{S_{22\mathrm{M}} - e'_{33}}{e'_{23} e'_{32}}\right) e'_{22}\right) - \\ - \left(\frac{S_{21\mathrm{M}} - e_{30}}{e_{10} e_{32}}\right)\left(\frac{S_{12\mathrm{M}} - e'_{03}}{e'_{23} e'_{01}}\right) e_{22} e\prime_{11} \tag{67}$$

$$S_{11} = \frac{\left(\frac{S_{11\mathrm{M}} - e_{00}}{e_{10} e_{01}}\right)\left(1 + \left(\frac{S_{22\mathrm{M}} - e'_{33}}{e'_{23} e'_{32}}\right) e'_{22}\right) - \left(\frac{S_{21\mathrm{M}} - e_{30}}{e_{10} e_{32}}\right)\left(\frac{S_{12\mathrm{M}} - e'_{03}}{e'_{23} e'_{01}}\right) e_{22}}{D} \tag{68}$$

$$S_{21} = \frac{\left(\frac{S_{21\mathrm{M}} - e_{30}}{e_{10} e_{32}}\right)\left(1 + \left(\frac{S_{22\mathrm{M}} - e'_{33}}{e'_{23} e'_{32}}\right)(e'_{22} - e_{22})\right)}{D} \tag{69}$$

$$S_{12} = \frac{\left(\frac{S_{12\mathrm{M}} - e'_{03}}{e'_{23} e'_{01}}\right)\left(1 + \left(\frac{S_{11\mathrm{M}} - e_{00}}{e_{10} e_{01}}\right)(e_{11} - e'_{11})\right)}{D} \tag{70}$$

$$S_{22} = \frac{\left(\frac{S_{22\mathrm{M}} - e'_{33}}{e'_{23} e'_{32}}\right)\left(1 + \left(\frac{S_{11\mathrm{M}} - e_{00}}{e_{10} e_{01}}\right) e_{11}\right) - \left(\frac{S_{21\mathrm{M}} - e_{30}}{e_{10} e_{32}}\right)\left(\frac{S_{12\mathrm{M}} - e'_{03}}{e'_{23} e'_{01}}\right) e'_{11}}{D} \tag{71}$$

## 5.4 Synthetic one-port measurement

It was shown in one of the previous chapters and in other papers [30, 44, 48] as well that virtual or synthetic measurement is a robust test which reveals errors resulting from poor definitions of calibration standards or from badly designed or simulated calibration kit. Thanks to its convenience it is a fast way of qualitative check before the elaborate and time-consuming experimental measurement.

The *synthetic* measurement relies only on simulated data of the test-fixture that are processed using calibration and correction method – ideal VNA is substituted by an EM field simulator, that lacks most of the repeatability problems that one would have to deal with in the real-world setup. The virtual error model contains the coaxial to microstrip launcher with a microstrip line, up to the chosen reference plane $l_{\mathrm{ref}} = 20\,\mathrm{mm}$ from the edge of the launcher (for illustration see Fig. 53).

Virtual calibration and correction based on one-port Least-Squares OSM calibration [4] was performed to assess the properties of designed test-fixture in comparison with the unmodified test-fixture.

In this case, the absence of connection repeatability is substituted by simulation errors of the EM solver. This random error is dependent on the solver accuracy and can be controlled (up to some level) with proper meshing and solver settings by the user. Provided the EM software is properly set up, the error associated with the solver

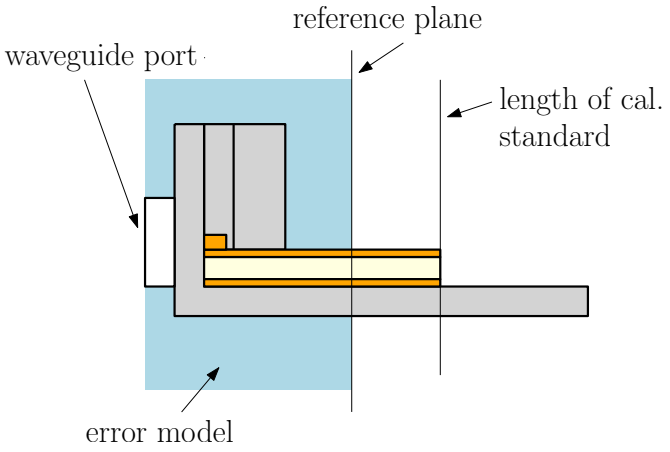


**Fig. 53** Schematic of the reference plane location for the synthetic data sets and for the experimental verification. Error model is highlighted with blue color.

would be significantly smaller than errors caused by the radiation. The frequency domain solver of CST Microwave Studio was used to calculate the S-parameters of six microstrip opens with different lengths. Both – unmodified and proposed test-fixtures were considered, which means that we obtain 12 *measured* S-parameters of 6 DUTs in two test-fixtures. To exploit the over-determined OSM calibration scheme, one can use as many calibration standards as possible instead of the more common approach with three standards. This results in increased usable unambiguous frequency band of this method.

The one-port calibration and correction was performed using known S-parameters of microstrip calibration kit that was described in the beginning of section 5.3. Detailed results of the virtual measurement are shown in Fig. 65. Instead of detailed plots, magnitudes of corrected reflection coefficients $S_{11}$ from standard and proposed test-fixtures are subtracted from the expected results of each DUT $S_{11_{\text{exp}}}$. The expected results are just simulated calibration standards used to perform the calibration. This overview is displayed in Fig. 54, where the magnitude discrepancies for each DUT illustrate the radiation influence for both test-fixtures. The error in magnitude and phase for $n$-th DUT can be calculated as:

$$E^n_{\text{mag}} = \left| S^n_{11} - S^n_{11_{\text{exp}}} \right| \tag{72}$$

$$E^n_{\text{phase}} = \arg\left( S^n_{11} - S^n_{11_{\text{exp}}} \right) \tag{73}$$

Both, the proposed test-fixture and the unmodified test-fixture do overlap in the magnitude with the expected trace up to approximately 15 GHz where the discrepancies caused by interactions between radiated field and QTEM on microstrip are starting to become an issue. Due to the fact that both approaches agree in phase for this test, there is no plot that would compare the arguments of the S-parameters because the results would essentially overlap.

In all cases the proposed solution outperforms the standard approach in terms of the magnitude of discrepancies on higher frequencies. The standard method suffers from radiation error in the order of hundredths while the proposed test-fixture performs much better up to 26 GHz where the suppression is clearly becoming not effective enough due to the parallel plate dimensions. These idealized results would be difficult to achieve with a real-world measurement on an actual VNA as one would have to deal with

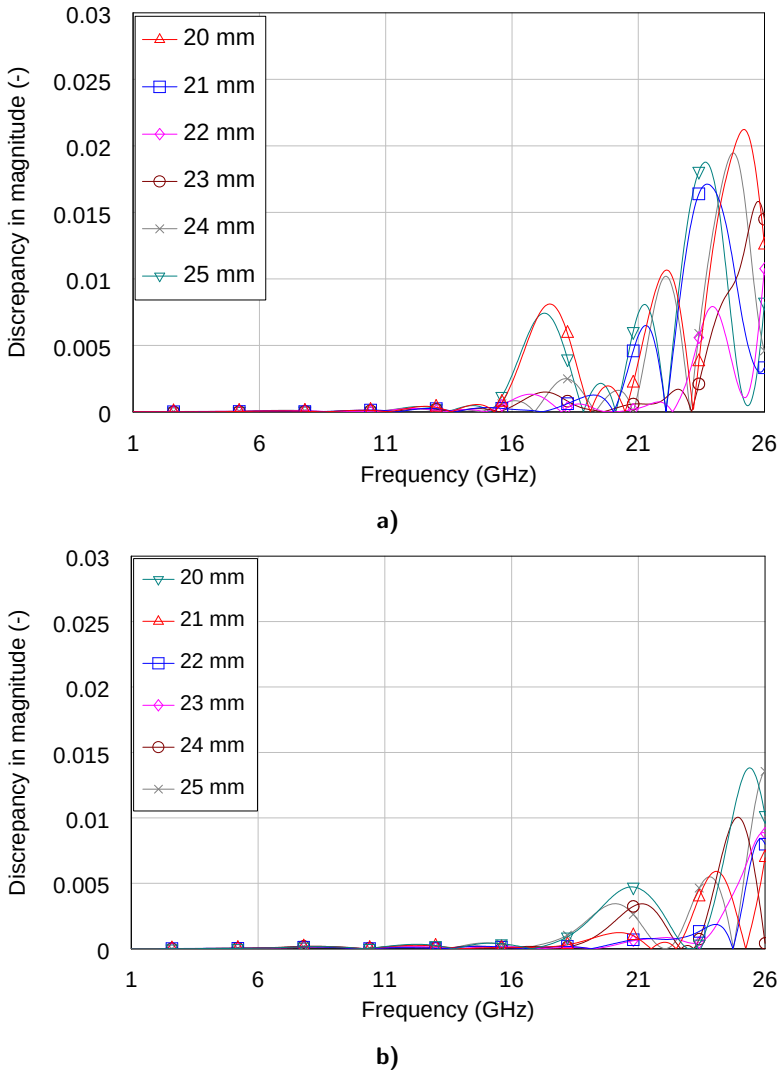


**Fig. 54** Discrepancies between calibrated and corrected virtual measurement of six microstrip open-ended DUTs and their simulated expected response. Results from proposed solution (b) compared to the standard test-fixture (a) show improved performance. The physical length of each DUT is described in the label.

measurement and fabrication repeatability along with measurement noise of the VNA. One can try to get as close as possible to the synthetic test data.

## 5.5 One-port measurements

Measurement was set up to validate the synthetic results that were carried out using CST Microwave Studio and calibration/correction algorithm in Matlab. The measurement was performed in a controlled and stable environment with temperature $23.5 \pm 0.5\,°\mathrm{C}$ and relative humidity $39 \pm 1\,\%$.

For the raw measurement acquisition, the Rohde&Schwarz ZVA67 VNA was used in the frequency range 1 GHz - 26 GHz. The measurement bandwidth (IF) was set to 50 Hz to minimize the random error and the noise floor of the VNA. The first-tier [55] calibration was performed using SOLT calibration with Agilent 3.5 mm precision calibration kit 85052C. Then, the internal 12-term error model was used to perform the

correction on the measured data within the VNA's firmware. The reference planes for the first-tier calibration are at both coaxial connectors of the test-fixture.

Then, second-tier calibration/correction was performed using custom-made microstrip calibration kit (see section 5.3). This calibration procedure is identical (including the distance to the reference plane) as the one performed with synthetic data, only the input raw S-parameters were measured with the real VNA and corrected with the first-tier calibration. Repeatability of the assembly and fitting of each microstrip standard or DUT into both test-fixtures remains the most significant uncalibrated random error present in the system. The worst case of two-port DUT's assembly repeatability in terms of average least-squares error (ALSE) was less than $-80\,\mathrm{dB}$ calculated by the following equation:

$$ALSE = 20\log\frac{\sum_{i=1}^{N}\sum_{j=1}^{N}\left(\left|S_{ij}^{A}-S_{ij}^{B}\right|\right)^{2}}{N^{2}} \tag{74}$$

where $\mathbf{S^A}$ and $\mathbf{S^B}$ are two S-parameter matrices with same dimension (number of ports) $N$ which are being compared. If there is perfect match between the data, the ALSE would be $-\infty$ (zero in linear scale).

Detailed results from the second-tier calibration and correction are shown in Fig. 66. Instead of detailed plots, magnitudes and phases of corrected reflection coefficients $|S_{11}|$ from standard and proposed test-fixtures are subtracted from the expected results of each DUT. This overview is displayed in Fig. 55, 56. The experimental verification validates the proposed approach although being less evident than in the case of synthetic data test. Apart from several repeatability issues at various frequencies, the agreement between expected and corrected measured trace is acceptable. The connection and manufacturing repeatability is the main source of discrepancy for the measurement on lower frequencies, while the radiation error starts to be significant above 18 GHz.

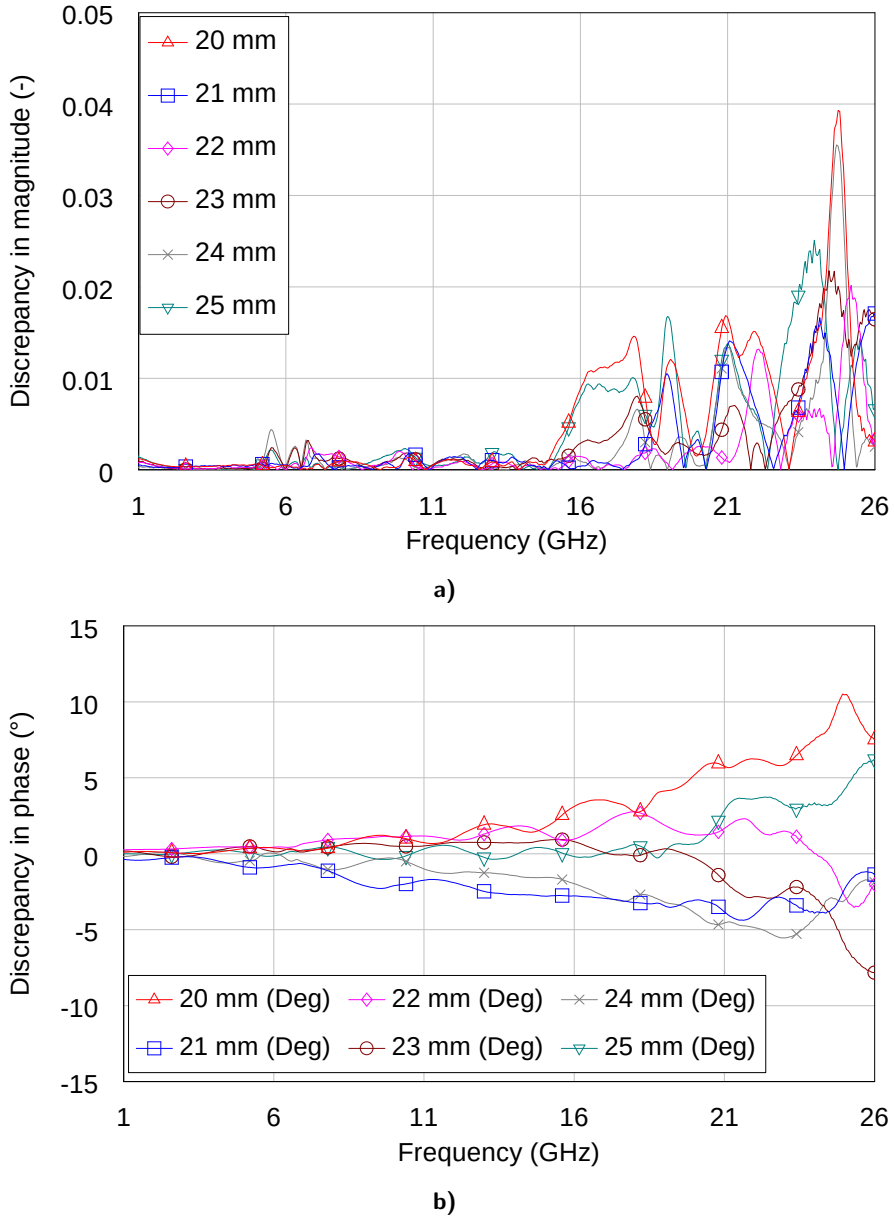


**Fig. 55** Discrepancies between calibrated and corrected reflection coefficients of six microstrip open-ended DUTs and their simulated expected trace. Both magnitude (a) and phase (b) results from measurement with standard test-fixture. The physical length of each DUT is described in the label.

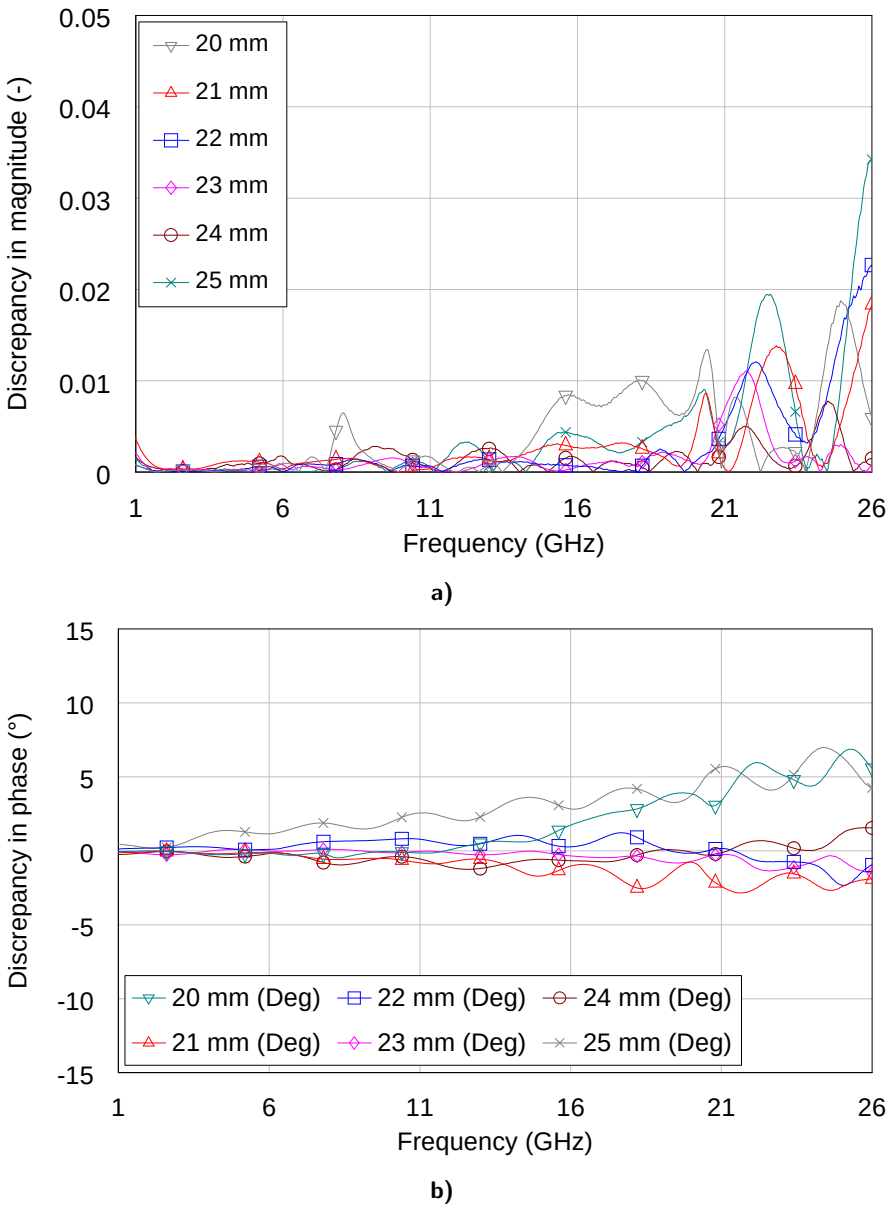


**Fig. 56** Discrepancies between calibrated and corrected reflection coefficients of six microstrip open-ended DUTs and their simulated expected trace. Both magnitude (a) and phase (b) results from measurement with the proposed test-fixture. The physical length of each DUT is described in the label.

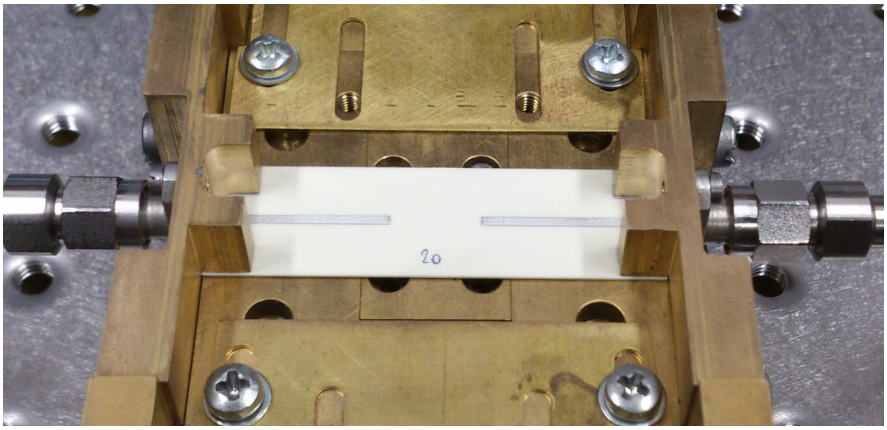

**Fig. 57** Photograph of a two-port DUT that is designed as an open-ended microstrip line at both sides with defined gap (10 mm in this case).

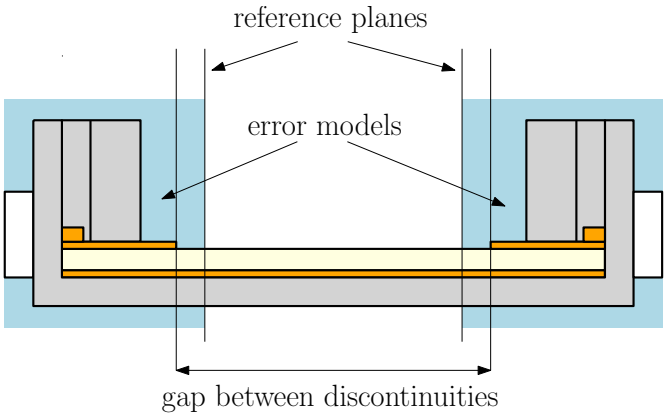


**Fig. 58** Schematic of the reference plane location for the transmission measurement. Error models are highlighted in light blue color.

## 5.6 Two-port measurements

For the purpose of the two-port measurement in the proposed test-fixture, reflective two-port DUTs were used. The measurement setup and conditions were maintained and are described in the previous section for the one-port measurement. The measured DUTs are designed as back-to-back open-ended microstrip lines with defined gap (see Fig. 57). The lengths of the gap for each DUT are 10, 20 and 30 mm.

The overdetermined one-port calibration that was described earlier was conducted at both ports of the test-fixture for the purpose of two-port measurement – two-port SOLT [3] calibration was used. Reference planes are set to $l_{\mathrm{ref}} = 20\,\mathrm{mm}$ from the edge of both launchers. Hence the known *thru* standard that is used for a correction has a non-zero length ($l_{\mathrm{thru}} = 10\,\mathrm{mm}$, $l_{\mathrm{std}} = 50\,\mathrm{mm}$) and all four S-parameters that have to be known were obtained using CST MWS. The reference planes for the two-port measurements are illustrated in Fig. 58.

The calibration was performed and the corrected $S_{21}$ data are plotted in Fig. 59 for all DUTs with various lengths. Similarly, as in the chapter 4, the crosstalk component can be quantified and compared with simulations to provide some information about the presence of the radiation.

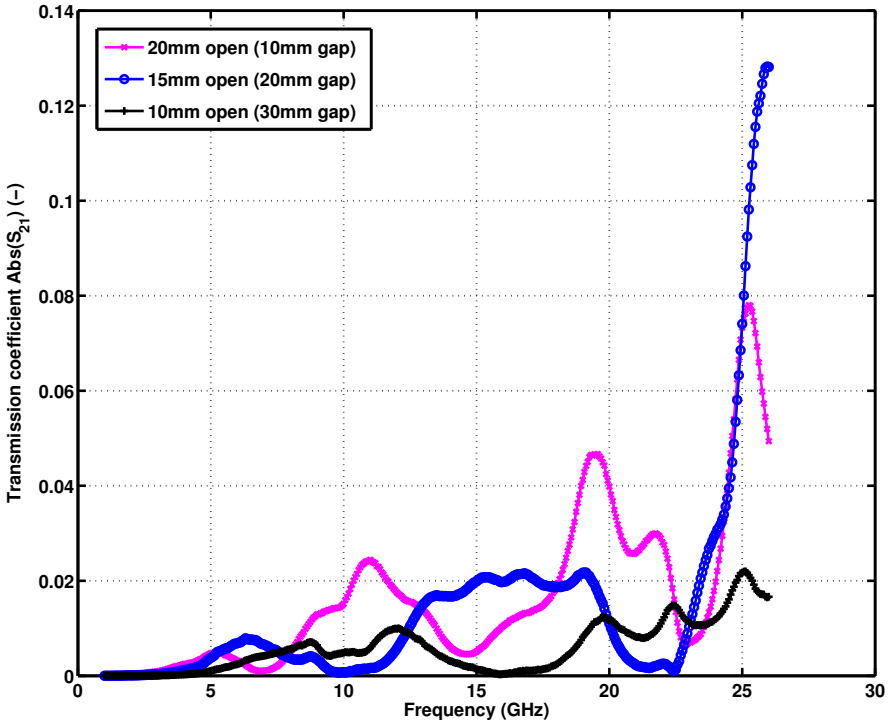


**Fig. 59** Corrected $|S_{21}|$ data for two-port reflective DUTs with an open-ended microstrip line at both sides separated by a defined gap (10, 20 and 30 mm).

### 5.6.1 Crosstalk component

A method useful to perform quantitative comparison of both test-fixtures from the radiation point of view was introduced in [38, 39] and was also presented in the chapter 4 of this thesis. This method is based on simulation or measurement of back-to-back arrangement of two highly reflective DUTs (for illustration see Fig. 58). Its main advantage is to exploit the superior accuracy and dynamic range of transmission measurements compared to the general reflection measurements. In this case, the back-to-back microstrip opens were simulated on the same substrate separated by a gap. The crosstalk between both ports is evaluated, which can be used to assess the radiated field. For a simplified signal flow graph of this method, see diagram in Fig. 29 from one of the previous chapters.

The corrected transmission coefficients for one selected DUT measured in both test-fixtures are shown in Fig. 60. The gap between both microstrip open ends is 30 mm. The intrinsic coupling between both discontinuities was simulated and is compared to the results for standard and proposed test-fixture. Improvement over the standard approach can be seen especially in frequencies above 15 GHz. Ideally, the corrected results should match very well to the simulated coupling but this is not the case especially for the simulation in the standard test-fixture, mainly because the coupled wave interferes with the radiated wave. These waves have different phase constants which produce troughs and peaks in the resulting transmission and this results in very large discrepancies. Additionally, considering the very low magnitudes of transmission $S_{21}$, this is demanding on the VNA's dynamic range and the EM solver accuracy as well, thus special care must be given to the solver set-up.

This simulation or measurement-based testing platform proved to be useful when evaluating the radiation properties of any existing or newly designed test-fixture. The

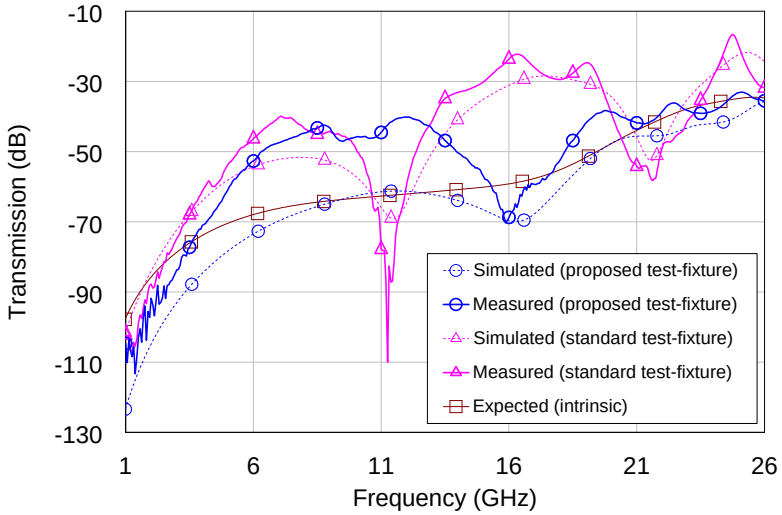


**Fig. 60** Simulated and measured traces of transmission coefficient $S_{21}$ of back-to-back microstrip open-ended DUT with a 30 mm gap in the standard and proposed test-fixture. All simulated and measured results are compared to the expected intrinsic coupling simulated in CST Microwave Studio.

measured and simulated crosstalks are compared to the expected trace. Expected trace was simulated using two open-ended microstrip lines in the same geometrical configuration but fed by a QTEM mode from a waveguide port. The proposed test-fixture shows improved suppression of the radiated power, therefore the magnitude of superimposed crosstalk on the intrinsic coupling is reduced in both simulated and measured data.

Compared to the results from chapter. 4, this method suffers from larger discrepancies between simulations and measurement (e.g. comparison between simulated and measured crosstalk in the proposed test-fixture – Fig. 60). One of the reasons for this can be that different transmission lines were used (microstrip line versus CPWG). Difficulties with simulation accuracy or possibly some random errors during the measurement might contribute to these errors as well.

Despite this issue, the proposed test-fixture still outperforms the standard one in this test as well as the one-port experimental verification.

## 5.7 Test-fixture design recommendations

This section summarizes the findings associated with radiation from coaxial-to-microstrip transitions and it presents general recommendations when designing new test-fixtures or even a new launcher to avoid the radiation phenomenon.

The results presented in this thesis validate the proposed test-fixture with the test case scenario with intentionally chosen substrate thickness of 0.508 mm in order to evaluate the radiation with some reasonable magnitude. With the substrate thickness $h$ decreasing, the radiation problems would be less evident (see Fig. 61), because the electric field in the cross-section of the launcher aperture is confined to the gap between coaxial center conductor and ground plane of the microstrip. This would mean that increased capacitance between the two electrodes forces the electric field lines into the substrate and to the microstrip ground plane. Similar effect would occur by using a substrate with higher permittivity.

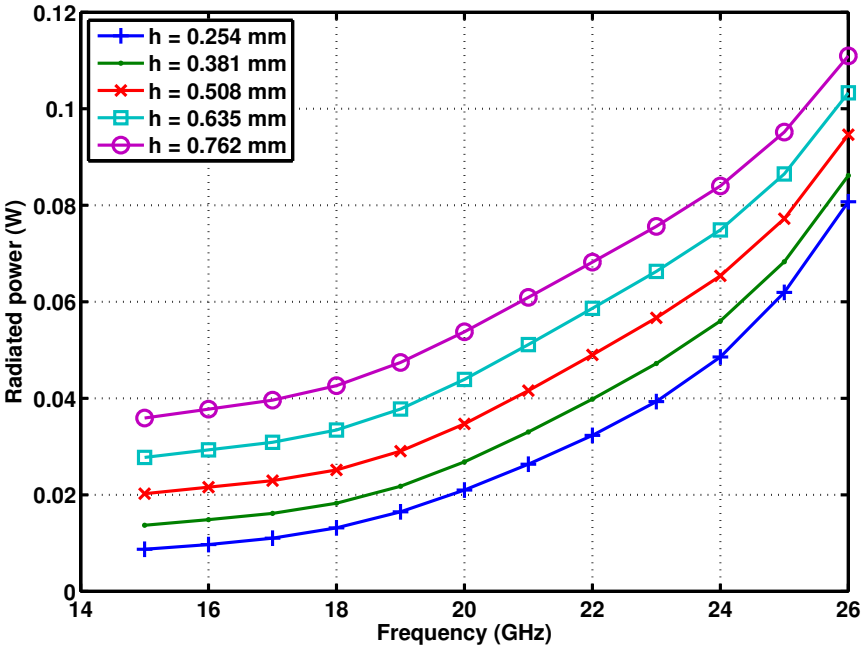


**Fig. 61** Simulation results of the swept substrate height with perfectly matched 50 Ω microstrip line mounted with a simplified launcher. The model of the launcher is consistent with the one shown in Fig. 17, but uses different substrate with relative permittivity $\varepsilon_r = 1.9$. Note that the radiated power is almost linearly dependent on the substrate height.

Hence it would be reasonable to say that with relatively high permittivity and decreasing thickness, the issues discussed in this thesis would not occur with such magnitude.

The distance between sidewalls $a$, which influences the cutoff frequency of the parallel-plate, can be chosen accordingly to the equation 55. This analytical approximation can be useful for the initial best guess for a new design. The length of the sidewalls $l_s$ should be close to the distance $a$ while longer sidewalls would suppress the radiation more effectively. Height of both sidewalls $b$ has strong effect on the final performance – as the height increases above $1.5\,a$, the parallel-plate is formed and further increase of the height is less effective, therefore good initial guess would be $b = 1.5\,a$. Both sidewalls should be connected to a common ground of the microstrip line to avoid any unwanted resonances. This can be achieved using plated-through vias in the substrate of each PCB. The transition between the coaxial line and the QTEM mode is made as a two-step process – firstly to the coplanar and then to microstrip.

For any given substrate, the dimensions of the launcher and its aperture should be optimized in the end to achieve the best possible results for any given test scenario.

## 5.8 Conclusion and measurement results

Together with an extensive study of radiation problem on coaxial-to-microstrip launchers, promising hardware approach was proposed to minimize this unwanted effect. The presented solution is based on enclosing an existing coaxial-to-microstrip transition into a short parallel-plate transmission line which has cutoff frequency above the working frequency of the test-fixture. Any radiated field is quickly attenuated because it is propagating inside a subcritical waveguide. The proposed method is extensively an-

alyzed in a CST Microwave Studio and fabricated test-fixture is verified by synthetic test set and experimental verification as well to show its impact on general calibration/correction techniques. Results in general show improved accuracy and reduce an uncertainty during measurements on microstrip in some specific use cases.

Detailed results of the virtual and experimental validation of the presented approach are presented in section B of the appendix. It has to be noted that the suppression is not as effective as with the use of buried microstrip configuration proposed by Hoffmann [44]. Despite this, the proposed test-fixture is more versatile and enables measurement of various devices without any constraints on their dimensions.

# 6 Conclusion

This thesis has presented four technical chapters in which my dissertation called *Precise measurement and modeling on planar transmission lines* should have been properly introduced. The uncertainty analysis in microwave measurement is becoming essential for every microwave engineer and researcher these days. Every measurement that does not provide or discuss the uncertainty analysis looses part of the credibility. The uncertainty propagation through measurement and calibration was introduced in the second chapter and one real world example was chosen to illustrate its application during VNA calibration and verification process.

The third and fourth chapters deal with a radiation from coaxial-to-planar transitions that was originally published at the Dept. of Electromagnetic Field during years 2007-2008. This phenomenon was not well understood at the time of the original publication [30], but some major advances have been made since then and are being introduced in this thesis. The research was focused on several parts: summarize the current state-of-the-art of this problem; try to find a suitable and practical way of quantifying the radiation during experimental measurements; understand the physical background of the radiation phenomenon and develop theoretical understanding of the radiation suppression.

Important analogies between open-ended coaxial line and very simple transition were found and with the 3D EM simulation tools and the obtained radiation properties helped to make a physical perspective over the transition's behavior. Moreover, it has been verified using the synthetic tests that the commonly used (and fairly elaborate) planar calibration method would indeed be disturbed by the radiation effects and its accuracy would be decreased.

It has been shown that the magnitude of the radiation is dependent on several factors and its reliable quantification is still an issue that needs resolving. Nevertheless, significant advances have been made in terms of the experimental quantification where a comparative measurement technique with a help of suitable simulation software can be useful to quantify the magnitude of radiated power so one can judge the quality of any given transition to microstrip.

Final chapter deals with a development, fabrication and experimental testing of a modified test-fixture with suppressed radiation properties. This chapter has shown some purely mechanical modifications that are based on the observations, measurements and simulations with a custom-built test-fixture. Complete design work-flow was described along with various parametric analysis to justify author's design choices. The validation results indeed show a reduced discrepancy compared to the standard approach effectively due to the suppressed radiation. Additionally, this modification does not require changes to the test boards that are mounted inside the test-fixture and it does not put any constraints on the size of the DUT.

## 6.1 Authored results dealing with the topic of the dissertation

- Partial effective error model extraction ($e_{00_{eff}}$) on planar transmission line with uncertainty analysis and post-calibration correction.

a) **Moravek, O.** - Prihoda, M. - Hoffmann, K., *Verification technique of on-planar VNA calibration*, In: Proceedings of 22nd International Conference Radioelektronika 2012, Brno, p. 103-106. ISBN 978-80-214-4468-3.

- Experimental measurement of the crosstalk component between two transitions and correlation with the radiated wave phenomenon.

  a) **Moravek, O.** - Hoffmann, K., *Radiation properties of Coaxial-to-coplanar transitions in K band*, In: Electronics Letters. 2012, vol. 48, no. 16, p. 1003-1004. ISSN 0013-5194.

  b) **Moravek, O.** - Hoffmann, K., *Measurement and Simulation of Coaxial to Microstrip Tansitions' Radiation Properties and Sbstrate Influence*, In: Radioengineering. 2012, vol. 21, no. 2, p. 568-572. ISSN 1210-2512.
- Radiation from coaxial-to-microstrip transition, its theoretical explanation and analogies with open-ended coaxial line. Suppression of the radiated waves from the transition with specific mechanical design of the transition's edge that does not introduce any frequency band limitations or manufacturing disadvantages.

  a) **Moravek, O.** - Hoffmann, K. - Polivka, M. - Jelinek, L., *Precise Measurement Using Coaxial-to-Microstrip Transition Through Radiation Suppression*, In: IEEE Transactions on Microwave Theory and Techniques. 2013, vol. 61, no. 8, p. 1-10. ISSN 0018-9480.

## 6.2 Other co-authored and published results

- Development of a load-pull technique for a design of a power amplifier.

  a) **Moravek, O.** - Hoffmann, K., *Improvement to Load-pull Technique for Design of Large-signal Amplifier in K Band*, In: Radioengineering. 2011, vol. 20, no. 4, p. 828-831. ISSN 1210-2512.
- Assembly influence on packaged transistors modeling using CST MWS.

  a) **Moravek, O.** - Hoffmann, K., *3D Modeling of Assembly Influence on Packaged Transistors*, In: 78th ARFTG Microwave Measurement Conference Proceedings [CD-ROM]. Piscataway: IEEE Microwave Theory and Techniques Society, US, 2011, p. 24-29. ISBN 978-1-4673-0281-4.
- Performance improvement of absorber suitable for microstrip or CPWG and its application as a sliding mismatch for VNA calibration.

  a) Prihoda, M. - **Moravek, O.** - Hoffmann, K., *Study of Absorber Materials Usable on Microstrip and Their Attribute Improvements*, In: Proceedings of 21st International Conference Radioelektronika 2011, Brno, p. 345-347. ISBN 978-1-61284-322-3.
- Wide-band measurement of losses due to the propagation through the window blinds.

  a) Valtr, P. - Pechac, P. - Korinek, T. - **Moravek, O.** - Prihoda, M., *Measurement of Window Blind Attenuation at 5-50 GHz*, In: Proceedings of the 7th European Conference on Antennas and Propagation (EUCAP 2013). Piscataway: IEEE, 2013, p. 3653-3656. ISBN 978-88-907018-1-8.

## 6.3 Additional remarks and the future work

Future work that can build on the published findings becomes possible by the discoveries presented in this thesis. One of the main motivations that came from working on my masters thesis that eventually got published [36] was to develop better understanding

of the radiation phenomenon that was rather new at the time. As it turned out, the radiation from the custom-made coaxial-to-microstrip transition prevented from achieving more accurate measurement results [21] thus the focus was aimed to the radiation from the transition during the following research.

The original paper [30] showed for the first time that the radiation is an issue and the subsequent work followed with more analysis that made possible to do an accurate description of the radiation phenomenon from the antenna theory point of view. The attention was paid to the EM simulation in CST MWS (later also in ANSYS HFSS) along with evaluating the experimental work with the same custom-made test-fixture that was used by Raboch and Hoffman [30]. Later, the Southwest Microwave launchers [28] were also analyzed and experimentally measured for the radiation effects. These efforts were later published [38, 39] and simple mathematical model that enables to predict the radiated power was introduced.

As the understanding of the theory behind the problem got improved, the effort moved to the development of a modified test-fixture that eventually led to the fabrication of the improved launcher which is covered in the article [48] along with the final chapter of this thesis. With the suppression now being proved as effective, this opens new possibilities of accurate measurement and characterization of active and passive devices in the higher frequencies. Major initiative for the future efforts would include the investigation of an updated planar VNA calibration technique that could use some modified error model of each transition in such way that it could eliminate the radiation problem completely using a correction technique without the need for an expensive mechanical modifications to the existing test-fixtures.

# Appendix A

# Reproduced measurement of the test-fixture with buried microstrip

In this section, complete results from synthetic data test (Fig. 62), i.e. from virtual measurement, along with experimental measurement (Fig. 63) of the test-fixture in so-called *canyon* configuration [44] are shown. The length of each microstrip open is described in each caption as a distance from the calibration reference plane that was set to 15 mm. If this was an ideal case of perfectly extracted error model and perfectly consistent simulations without any random errors, the corrected values $S_{11}$ would match the expected traces.

The measurement data also contain the $S_{21}$ measurements (see Fig. 64) that show that the crosstalk component in the buried microstrip line is completely suppressed up to the cutoff frequency of the first high-order waveguide mode of the structure.

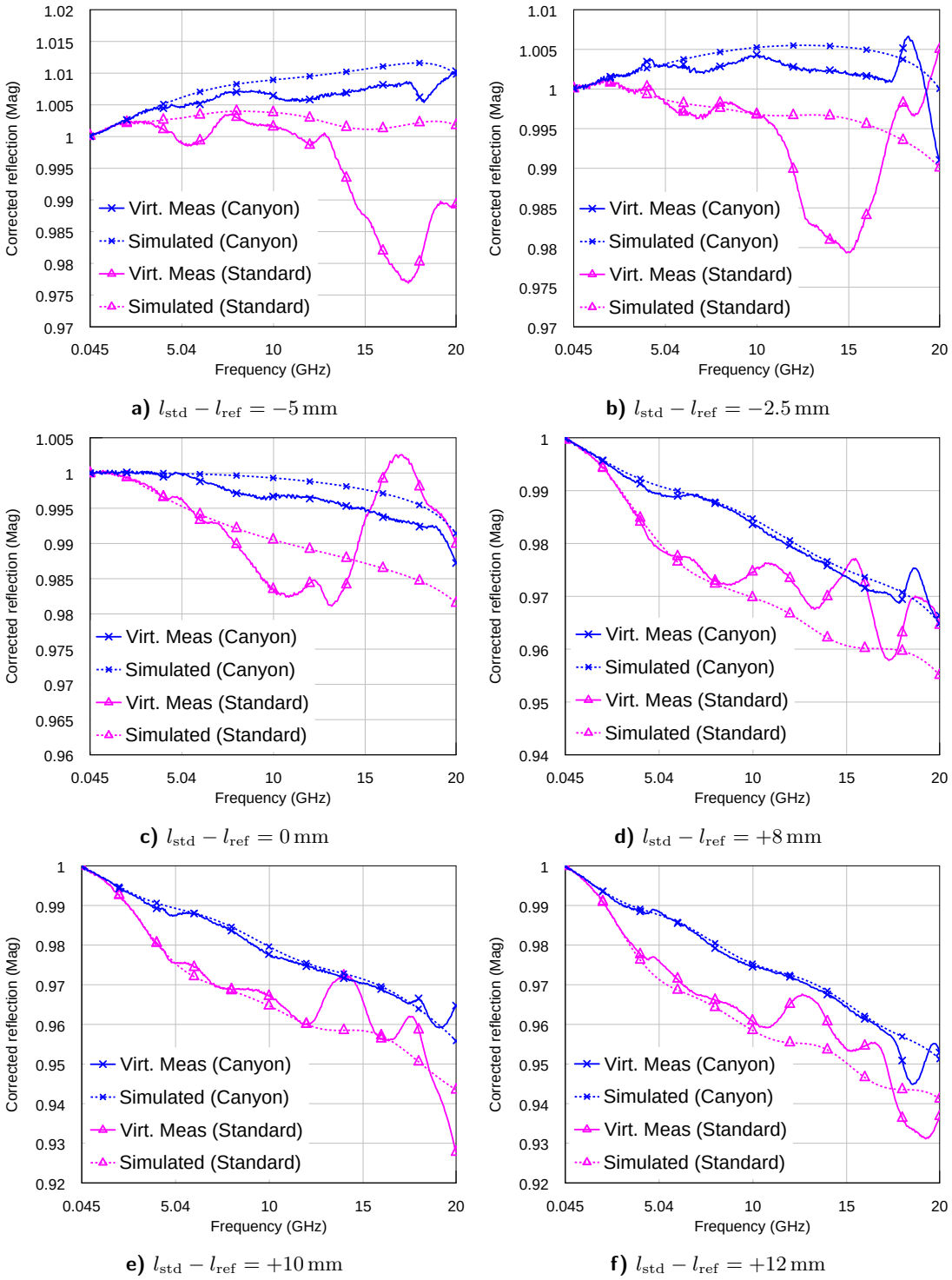


**a)** $l_{\mathrm{std}} - l_{\mathrm{ref}} = -5\,\mathrm{mm}$ **b)** $l_{\mathrm{std}} - l_{\mathrm{ref}} = -2.5\,\mathrm{mm}$

**c)** $l_{\mathrm{std}} - l_{\mathrm{ref}} = 0\,\mathrm{mm}$ **d)** $l_{\mathrm{std}} - l_{\mathrm{ref}} = +8\,\mathrm{mm}$

**e)** $l_{\mathrm{std}} - l_{\mathrm{ref}} = +10\,\mathrm{mm}$ **f)** $l_{\mathrm{std}} - l_{\mathrm{ref}} = +12\,\mathrm{mm}$

**Fig. 62** Comparison of reflection coefficient $|S_{11}|$ among corrected data from the virtual measurement of DUTs with various lengths simulated on a 0.508 mm thick Rogers RO4350 substrate. Two calibrations were performed using a standard test-fixture and a *canyon* structure as well. Both traces are compared to the expected trace calculated using CST MWS.

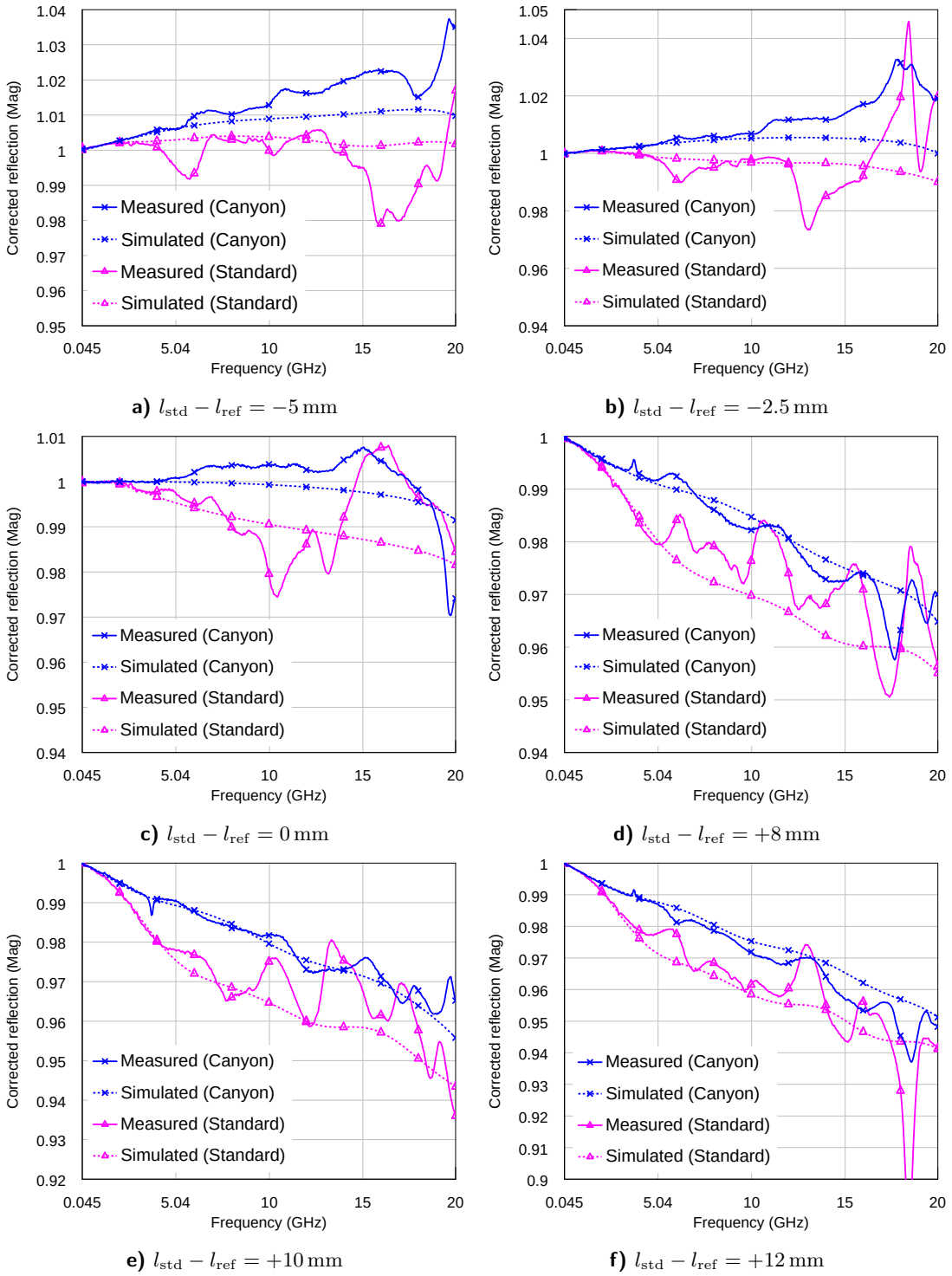


**a)** $l_{\mathrm{std}} - l_{\mathrm{ref}} = -5\,\mathrm{mm}$ **b)** $l_{\mathrm{std}} - l_{\mathrm{ref}} = -2.5\,\mathrm{mm}$

**c)** $l_{\mathrm{std}} - l_{\mathrm{ref}} = 0\,\mathrm{mm}$ **d)** $l_{\mathrm{std}} - l_{\mathrm{ref}} = +8\,\mathrm{mm}$

**e)** $l_{\mathrm{std}} - l_{\mathrm{ref}} = +10\,\mathrm{mm}$ **f)** $l_{\mathrm{std}} - l_{\mathrm{ref}} = +12\,\mathrm{mm}$

**Fig. 63** Comparison of reflection coefficient $|S_{11}|$ among corrected measured data of DUTs with various lengths fabricated on a 0.508 mm thick Rogers RO4350 substrate. Two calibrations were performed using a standard test-fixture and a *canyon* structure as well. Both traces are compared to the expected trace calculated using CST MWS.

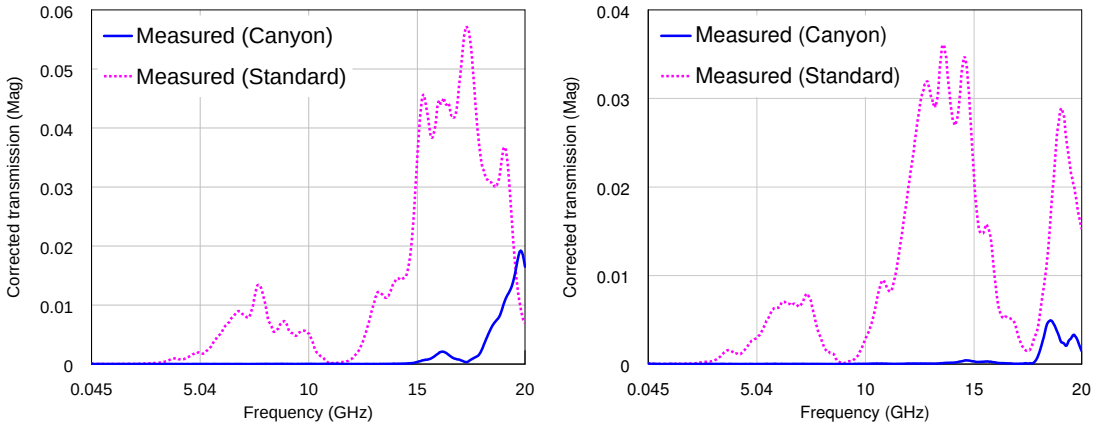


**a)** $-5; -5\,\mathrm{mm}$ **b)** $-2.5; -2.5\,\mathrm{mm}$

**c)** $0; 0\,\mathrm{mm}$ **d)** $+8; +8\,\mathrm{mm}$

**Fig. 64** Comparison of transmission coefficient $|S_{21}|$ among corrected measured data of DUTs with various lengths fabricated on a 0.508 mm thick Rogers RO4350 substrate. Two calibrations were performed using a standard test-fixture and a *canyon* structure as well.

# Appendix B

# Validation measurement of the proposed test-fixture

In this section, complete results from synthetic data test (i.e. from virtual measurement) along with experimental verification of the proposed test-fixture are shown. The length of each microstrip open is described in each caption as a distance from the calibration reference plane. If this was an ideal case of perfectly extracted error model and perfectly consistent simulations, the corrected values $S_{11}$ should match the expected results.

The caption of each figure describes difference between the standard's length and distance to the reference plane. It is easy to see the benefit of the proposed modification in the synthetic data test (see Fig. 65). Results in Fig. 66 are influenced by the real-world fabrication and measurement repeatability effects which vary with each measurement. Still, the details of the traces from experimental results match with the virtual measurements surprisingly well.

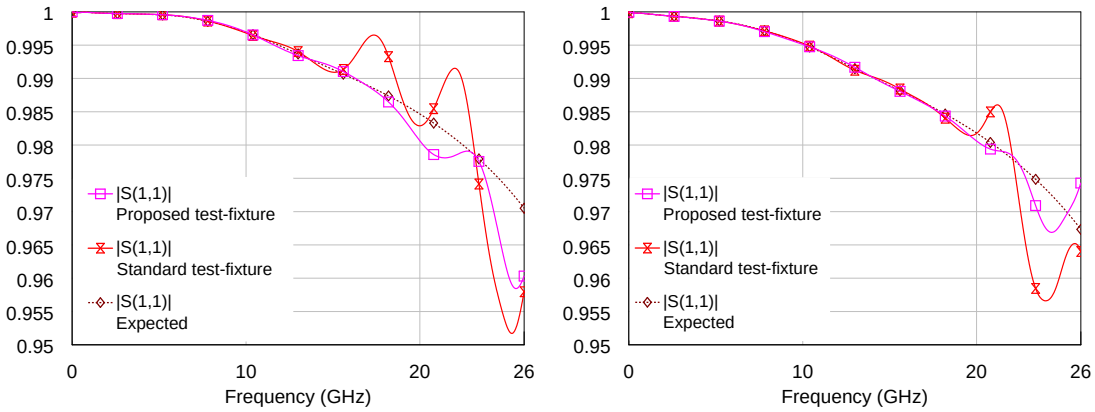


**a)** $l_{\mathrm{std}} - l_{\mathrm{ref}} = 0\,\mathrm{mm}$




**b)** $l_{\mathrm{std}} - l_{\mathrm{ref}} = +1\,\mathrm{mm}$

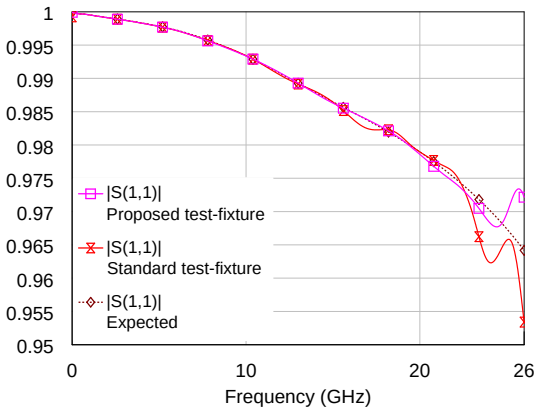


**c)** $l_{\mathrm{std}} - l_{\mathrm{ref}} = +2\,\mathrm{mm}$

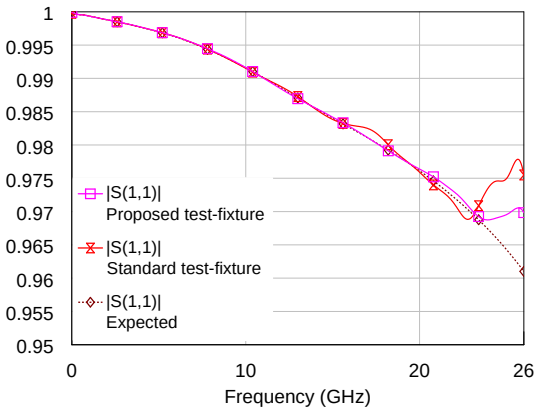


**d)** $l_{\mathrm{std}} - l_{\mathrm{ref}} = +3\,\mathrm{mm}$

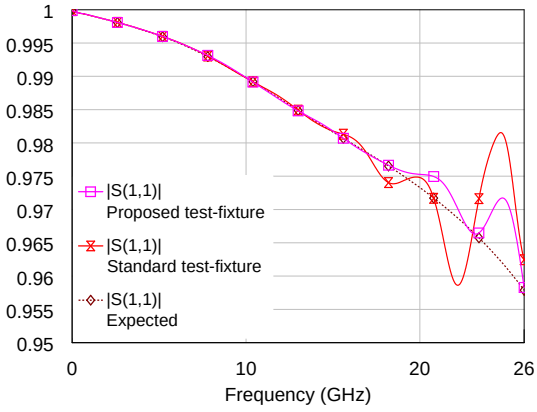


**e)** $l_{\mathrm{std}} - l_{\mathrm{ref}} = +4\,\mathrm{mm}$

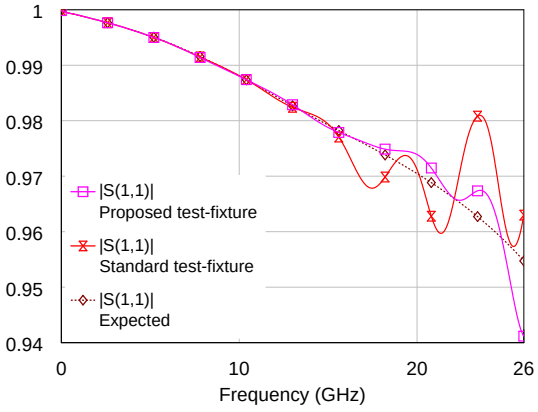


**f)** $l_{\mathrm{std}} - l_{\mathrm{ref}} = +5\,\mathrm{mm}$

**Fig. 65** Reflection coefficient $S_{11}$ obtained by the synthetic data test with the calibrated and corrected virtual measurements of six microstrip open-ended DUTs. Results from the standard test-fixture are compared to the proposed solution to highlight the improvements. The expected trace obtained by CST Microwave Studio is shown as well.

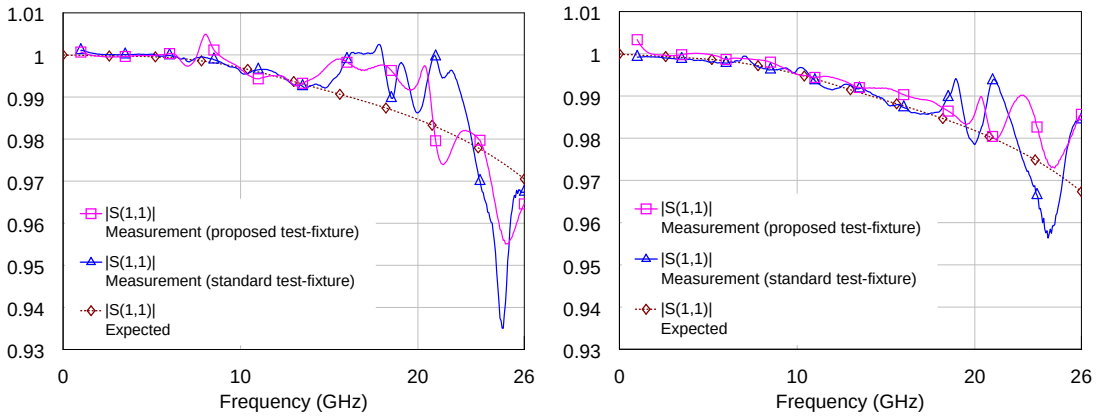


**a)** $l_{\mathrm{std}} - l_{\mathrm{ref}} = 0\,\mathrm{mm}$ **b)** $l_{\mathrm{std}} - l_{\mathrm{ref}} = +1\,\mathrm{mm}$

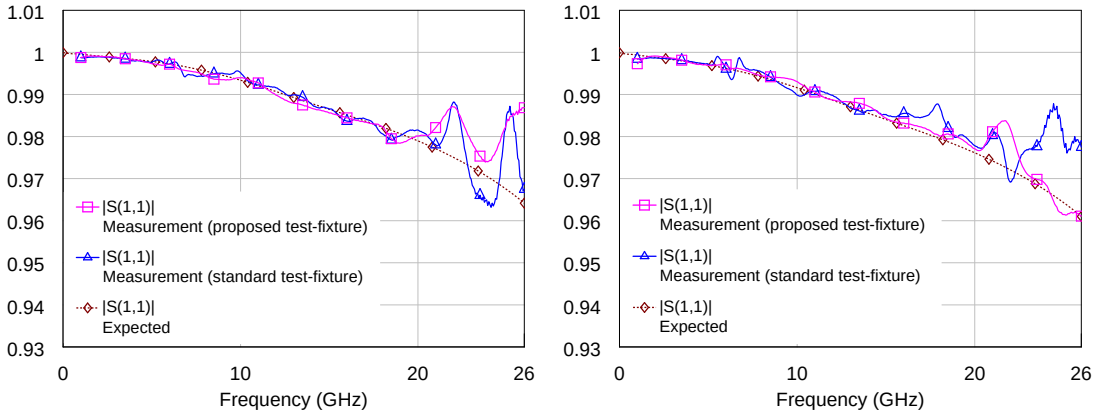


**c)** $l_{\mathrm{std}} - l_{\mathrm{ref}} = +2\,\mathrm{mm}$ **d)** $l_{\mathrm{std}} - l_{\mathrm{ref}} = +3\,\mathrm{mm}$

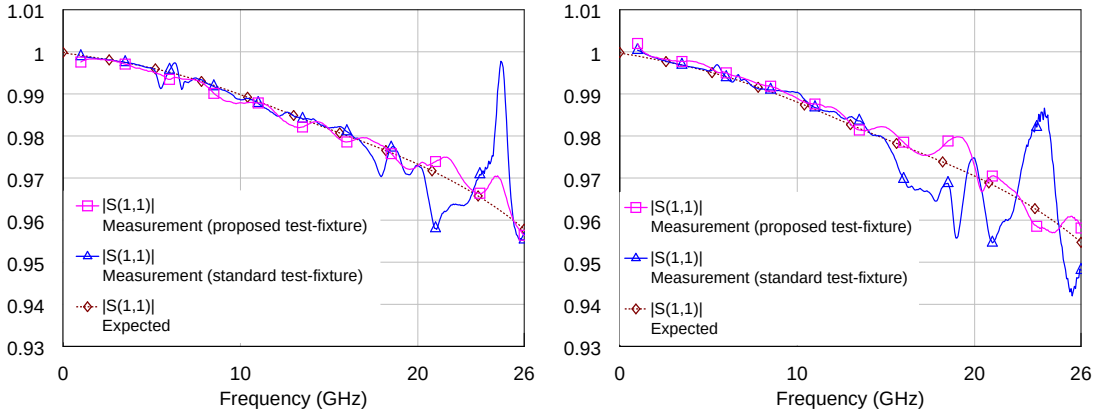


**e)** $l_{\mathrm{std}} - l_{\mathrm{ref}} = +4\,\mathrm{mm}$ **f)** $l_{\mathrm{std}} - l_{\mathrm{ref}} = +5\,\mathrm{mm}$

**Fig. 66** Reflection coefficients $S_{11}$ obtained from the calibrated and corrected measurements of six microstrip open-ended DUTs. Results from the standard test-fixture are compared to the proposed solution to highlight the improvements. The expected trace obtained by CST Microwave Studio is shown as well.

# Bibliography


[1] R. A. Hackborn. “An automatic network analyzer system”. In: *Microwave Journal* 11 (1968).

[2] M. Hiebel. *Fundamentals of Vector Network Analysis*. 1st ed. 2007.

[3] Stig Rehnmark. “On the Calibration Process of Automatic Network Analyzer Systems (Short Papers)”. In: *Microwave Theory and Techniques, IEEE Transactions on* 22.4 (Apr. 1974), pp. 457–458. ISSN: 0018-9480. DOI: 10.1109/TMTT.1974.1128250.

[4] D. Blackham. “Application of weighted least squares to OSL vector error correction”. In: *ARFTG Conference Digest, Spring 2003. 61st.* June 2003, pp. 11–21. DOI: 10.1109/ARFTGS.2003.1216862.

[5] A. Ferrero and U. Pisani. “Two-port network analyzer calibration using an unknown ’thru’”. In: *Microwave and Guided Wave Letters, IEEE* 2.12 (Dec. 1992), pp. 505–507. ISSN: 1051-8207. DOI: 10.1109/75.173410.

[6] Glenn F. Engen and Cletus A. Hoer. “Thru-Reflect-Line: An Improved Technique for Calibrating the Dual Six-Port Automatic Network Analyzer”. In: *Microwave Theory and Techniques, IEEE Transactions on* 27.12 (Dec. 1979), pp. 987–993. ISSN: 0018-9480. DOI: 10.1109/TMTT.1979.1129778.

[7] Roger B. Marks. “A multiline method of network analyzer calibration”. In: *Microwave Theory and Techniques, IEEE Transactions on* 39.7 (July 1991), pp. 1205–1215. ISSN: 0018-9480. DOI: 10.1109/22.85388.

[8] F. Lenk, R. Doerner, and A. Rumiantsev. “Sensitivity Analysis of S-Parameter Measurements Due to Calibration Standards Uncertainty”. In: *Microwave Theory and Techniques, IEEE Transactions on* 61.10 (Oct. 2013), pp. 3800–3807. ISSN: 0018-9480. DOI: 10.1109/TMTT.2013.2279774.

[9] Nick M. Ridler and Martin J. Salter. “Propagating S-parameter uncertainties to other measurement quantities”. In: *ARFTG Conference Digest-Fall, 58th.* Vol. 40. Nov. 2001, pp. 1–19. DOI: 10.1109/ARFTG.2001.327487.

[10] Nick M Ridler and Martin J Salter. “An approach to the treatment of uncertainty in complex S-parameter measurements”. In: *Metrologia* 39.3 (2002), p. 295.

[11] A. Lewandowski et al. “Covariance-Based Vector-Network-Analyzer Uncertainty Analysis for Time- and Frequency-Domain Measurements”. In: *Microwave Theory and Techniques, IEEE Transactions on* 58.7 (July 2010), pp. 1877–1886. ISSN: 0018-9480. DOI: 10.1109/TMTT.2010.2049768.

[12] M. Garelli and A. Ferrero. “A Unified Theory for S -Parameter Uncertainty Evaluation”. In: *Microwave Theory and Techniques, IEEE Transactions on* 60.12 (Dec. 2012), pp. 3844–3855. ISSN: 0018-9480. DOI: 10.1109/TMTT.2012.2221733.

[13] M. Wollensack et al. “VNA Tools II: S-parameter uncertainty calculation”. In: *Microwave Measurement Conference (ARFTG), 2012 79th ARFTG*. June 2012, pp. 1–5. DOI: 10.1109/ARFTG79.2012.6291183.

[14] J. Leinhos and U. Arz. “Monte-Carlo analysis of measurement uncertainties for on-wafer thru-reflect-line calibrations”. In: *Microwave Symposium Digest, 2008 IEEE MTT-S International*. June 2008, pp. 33–36.

[15] ISO. *Guide to the expression of uncertainty in measurement*. International Organization for Standardization, 1993.

[16] Nick M. Ridler and Martin J. Salter. “Evaluating and expressing uncertainty in complex S-parameter measurements”. In: *ARFTG Conference Digest-Fall, 56th*. Vol. 38. Nov. 2000, pp. 1–13. DOI: 10.1109/ARFTG.2000.327429.

[17] Robert W. Beatty. “Insertion loss concepts”. In: *Proceedings of the IEEE* 52.6 (June 1964), pp. 663–671. ISSN: 0018-9219. DOI: 10.1109/PROC.1964.3047.

[18] Glenn F. Engen. “Amplitude Stabilization of a Microwave Signal Source”. In: *Microwave Theory and Techniques, IRE Transactions on* 6.2 (Apr. 1958), pp. 202–206. ISSN: 0097-2002. DOI: 10.1109/TMTT.1958.1124538.

[19] G. Wubbeler et al. “Determination of complex residual error parameters of a calibrated vector network analyzer”. In: *ARFTG Conference, 2007 69th*. June 2007, pp. 1–4. DOI: 10.1109/ARFTG.2007.5456312.

[20] R.H. Judaschke. “Second-order waveguide calibration of a one-port vector network analyzer”. In: *Microwave Measurement Conference (ARFTG), 2011 77th ARFTG*. June 2011, pp. 1–3. DOI: 10.1109/ARFTG77.2011.6034566.

[21] O. Moravek and K. Hoffmann. “3D Modeling of assembly influence on packaged transistors”. In: *Microwave Measurement Symposium (ARFTG), 2011 78th ARFTG*. Dec. 2011, pp. 1–6. DOI: 10.1109/ARFTG78.2011.6183866.

[22] V. Sokol et al. “Assembly influence on S-parameters of packaged transistor”. In: *ARFTG Conference Digest, 2005. Spring 2005. 65th*. June 2005, p. 5. DOI: 10.1109/ARFTGS.2005.1500579.

[23] K. E. Jones and W. K. Harwood. “Coaxial transmission line to microstrip transmission line launcher”. U.S. Patent 4 855 697. Aug. 8, 1989.

[24] K. K. Agarwal and R. R. Harlan. “Coax-to-microstrip transition”. U.S. Patent 5 552 753. Sept. 3, 1996.

[25] C. Quan. “Coaxial-to-coplanar-waveguide transmission line connector using integrated slabline transition”. U.S. Patent 5 570 068. Oct. 29, 1996.

[26] C. J. Kellett and A. Smith. “Coaxial cable transition arrangement”. U.S. Patent 5 986 519. Nov. 16, 1999.

[27] D.K. Snodgrass et al. “Coaxial-to-microstrip transitions”. U.S. Patent 7 915 981. Mar. 29, 2011.

[28] Southwest Microwave Inc. *End Launch Connectors Models and Specifications*. URL: http://mpd.southwestmicrowave.com/products/family.php?family=71 (visited on 04/24/2014).

[29] Inter-Continental Microwave. *UniversalSubstrate TestFixture*. URL: http://www.icmicrowave.com/pdf/wksubstrate.pdf (visited on 04/29/2014).

[30] J. Raboch et al. “Hidden problems in precise calibration on microstrip”. In: *ARFTG Microwave Measurement Symposium, 2008 72nd*. Dec. 2008, pp. 37–39. DOI: 10.1109/ARFTG.2008.4804286.

[31] Helmut Ermert. "Guiding and radiation characteristics of planar waveguides". In: *Microwaves, Optics and Acoustics, IEE Journal on* 3.2 (Mar. 1979), pp. 59–62. ISSN: 0308-6976. DOI: 10.1049/ij-moa:19790013.

[32] José Luis Gómez-Tornero, Fernando Daniel Quesada-Pereira, and Alejandro Álvarez-Melcón. "A full-wave space-domain method for the analysis of leaky-wave modes in multilayered planar open parallel-plate waveguides". In: *International Journal of RF and Microwave Computer-Aided Engineering* 15.1 (2005), pp. 128–139.

[33] A.A. Oliner and K. S. Lee. "The Nature of the Leakage from Higher Modes on Microstrip Line". In: *Microwave Symposium Digest, 1986 IEEE MTT-S International*. June 1986, pp. 57–60. DOI: 10.1109/MWSYM.1986.1132108.

[34] Lei Liu, C. Caloz, and T. Itoh. "Dominant mode leaky-wave antenna with backfire-to-endfire scanning capability". In: *Electronics Letters* 38.23 (Nov. 2002), pp. 1414–1416. ISSN: 0013-5194. DOI: 10.1049/el:20020977.

[35] J. Machac, M. Polivka, and K. Zemlyakov. "A Dual Band Leaky Wave Antenna on a CRLH Substrate Integrated Waveguide". In: *Antennas and Propagation, IEEE Transactions on* 61.7 (July 2013), pp. 3876–3879. ISSN: 0018-926X. DOI: 10.1109/TAP.2013.2256097.

[36] Ondrej Moravek and Karel Hoffmann. "Improvement to Load-pull Technique for Design of Large-signal Amplifier in K band." In: *Radioengineering* 20.4 (2011).

[37] C. Setzer. "High power nonlinear measurements: Calibration issues, real time loadpull, and other RF data". In: *Microwave Measurement Symposium (ARFTG), 2012 80th ARFTG*. Nov. 2012, pp. 1–4. DOI: 10.1109/ARFTG.2012.6422435.

[38] Ondrej Moravek and Karel Hoffmann. "Radiation properties of coaxial-to-coplanar transitions in K band". In: *Electronics letters* 48.16 (2012), pp. 1003–1004.

[39] Ondrej Moravek and Karel Hoffmann. "Measurement and Simulation of Coaxial to Microstrip Transitions' Radiation Properties and Substrate Influence." In: *Radioengineering* 21.2 (2012).

[40] Martin J Salter, Nick M Ridler, and Peter M Harris. "Over-determined calibration schemes for RF network analysers employing generalised distance regression". In: *ARFTG Microwave Measurements Conference, 2003. Fall 2003. 62nd.* IEEE. 2003, pp. 127–142.

[41] J. Hoffmann, P. Leuchtmann, and R. Vahldieck. "Over-determined offset short calibration of a VNA". In: *Microwave Symposium Digest, 2008 IEEE MTT-S International*. June 2008, pp. 47–50. DOI: 10.1109/MWSYM.2008.4633318.

[42] J. Hoffmann et al. "A Stable Bayesian Vector Network Analyzer Calibration Algorithm". In: *Microwave Theory and Techniques, IEEE Transactions on* 57.4 (Apr. 2009), pp. 869–880. ISSN: 0018-9480. DOI: 10.1109/TMTT.2009.2015096.

[43] Jui-Ching Cheng et al. "Improving the High-Frequency Performance of Coaxial-to-Microstrip Transitions". In: *Microwave Theory and Techniques, IEEE Transactions on* 59.6 (June 2011), pp. 1468–1477. ISSN: 0018-9480. DOI: 10.1109/TMTT.2011.2123911.

[44] K. Hoffmann and J. Raboch. "Hidden problems in precise calibration on microstrip II explanation and solution". In: *Microwave Measurement Symposium (ARFTG), 2011 78th ARFTG*. Dec. 2011, pp. 1–5. DOI: 10.1109/ARFTG78.2011.6183879.

[45] T. Ishikawa and E. Yamashita. “Characterization of buried microstrip lines for constructing high-density microwave integrated circuits”. In: *Microwave Theory and Techniques, IEEE Transactions on* 44.6 (June 1996), pp. 840–847. ISSN: 0018-9480.

[46] Simon Ramo, John R Whinnery, and Theodore Van Duzer. *Fields and waves in communication electronics*. John Wiley & Sons, 2007.

[47] Rogers Corporation. *RO4000® Series High Frequency Circuit Materials*. URL: http://www.rogerscorp.com/documents/726/acm/RO4000-Laminates---Data-sheet.pdf (visited on 04/24/2014).

[48] O. Moravek et al. “Precise Measurement Using Coaxial-to-Microstrip Transition Through Radiation Suppression”. In: *Microwave Theory and Techniques, IEEE Transactions on* 61.8 (Aug. 2013), pp. 2956–2965. ISSN: 0018-9480. DOI: 10.1109/TMTT.2013.2272380.

[49] Southwest Microwave Inc. *2.92mm (Female) End Launch Connector, Model: 1092-01A-5*. URL: http://mpd.southwestmicrowave.com/showImage.php?image=774%5C&name=1092-01A-5.pdf (visited on 04/24/2014).

[50] E. Hammerstad and O. Jensen. “Accurate Models for Microstrip Computer-Aided Design”. In: *Microwave symposium Digest, 1980 IEEE MTT-S International*. May 1980, pp. 407–409. DOI: 10.1109/MWSYM.1980.1124303.

[51] Rohde&Schwarz GmbH&Co. KG. *R&S ZVA Vector Network Analyzer Specifications*. URL: http://cdn.rohde-schwarz.com/dl_downloads/dl_common_library/dl_brochures_and_datasheets/pdf_1/ZVA_dat-sw_en.pdf (visited on 04/24/2014).

[52] Coaxial Components Corp. *Flange Mount Jack Model 3244-4A (former Omni-Spectra P/N: 2052-5277)*. URL: http://www.coaxicom.com/pdf/catalog.pdf (visited on 04/24/2014).

[53] Stig Rehnmark. “On the Calibration Process of Automatic Network Analyzer Systems (Short Papers)”. In: *Microwave Theory and Techniques, IEEE Transactions on* 22.4 (Apr. 1974), pp. 457–458. ISSN: 0018-9480. DOI: 10.1109/TMTT.1974.1128250.

[54] Doug Rytting. *Network Analyzer Error Models and Calibration Methods*. URL: http://emlab.uiuc.edu/ece451/appnotes/Rytting_NAModels.pdf (visited on 04/30/2014).

[55] R. Vaitkus and D. Scheitlin. “A Two-Tier Deembedding Technique for Packaged Transistors”. In: *Microwave Symposium Digest, 1982 IEEE MTT-S International*. June 1982, pp. 328–330. DOI: 10.1109/MWSYM.1982.1130708.

# Appendix C

# List of candidate's works relating to the doctoral thesis

## C.1 Publications in impacted journals

A1 **Moravek, O.** - Hoffmann, K., *Radiation properties of Coaxial-to-coplanar transitions in K band*, In: Electronics Letters. 2012, vol. 48, no. 16, p. 1003-1004. ISSN 0013-5194.
author contribution 50 %

A2 **Moravek, O.** - Hoffmann, K., *Measurement and Simulation of Coaxial to Microstrip Tansitions' Radiation Properties and Sbstrate Influence*, In: Radioengineering. 2012, vol. 21, no. 2, p. 568-572. ISSN 1210-2512.
author contribution 50 %

A3 **Moravek, O.** - Hoffmann, K. - Polivka, M. - Jelinek, L., *Precise Measurement Using Coaxial-to-Microstrip Transition Through Radiation Suppression*, In: IEEE Transactions on Microwave Theory and Techniques. 2013, vol. 61, no. 8, p. 1-10. ISSN 0018-9480.
author contribution 25 %

## C.2 Publications in WOS database

None

## C.3 Peer-reviewed publications

C1 **Moravek, O.** - Prihoda, M. - Hoffmann, K., *Verification technique of on-planar VNA calibration*, In: Proceedings of 22nd International Conference Radioelektronika 2012. Brno, 2012, p. 103-106. ISBN 978-80-214-4468-3.
author contribution 34 %

## C.4 Other publications

None

## C.5 Responses and citations

- The paper [C1] was referenced in: Prihoda, M. - Hoffmann, K., *Novel Multimode Planar Absorbing Structure,* In: IEEE Microwave and Wireless Components Letters. 2013, vol. 23, no. 1, p. 7-9. ISSN 1531-1309.